CORROSION IN SUPERCRITICAL WATER (SCW)

EFFECT OF Cr CONTENT ON CORROSION RESISTANCE OF Fe-Cr-Ni ALLOYS EXPOSED IN SUPERCRITICAL WATER (SCW)

BY: SHOOKA MAHBOUBI, B.Eng.

A Thesis Submitted To The Department of Materials Science and Engineering in Partial Fulfilment of the Requirements for the Degree Master's of Applied Science in Materials Engineering

McMaster University

Title: Effect of Cr Content on Corrosion Resistance of Fe-Cr-Ni Alloys Exposed in Supercritical Water (SCW)

Author: Shooka Mahboubi, B.Eng. (University of Tehran)

Supervisors: Dr. Joey R. Kish and Dr. Gianluigi A. Botton

Pages: xii-99

Abstract

The aim of this work was to rationalize the corrosion resistance of candidate austenitic iron-chromium-nickel (Fe-Cr-Ni) alloys in supercritical water (SCW) for use as fuel claddings within the in-core structure of the Canadian supercritical water-cooled reactor (SCWR) concept. High chromium (Cr)-containing alloys (Alloy 800HT with 20.6 wt.% Cr and 30.7 wt.% Ni and Alloy 33 with 33.4 wt.% Cr and 31.9 wt.% Ni) in the mill annealed condition were chosen for this purpose. Coupons were exposed on a short-term basis (500 h) in a static autoclave containing 25 MPa SCW at 550 °C and 625 °C. Gravimetric measurements and electron microscopy techniques were then used to study the oxidation/corrosion resistance of two alloys. Alloy 33 was found to exhibit the higher corrosion resistance at both temperatures. The improved corrosion resistance of Alloy 33 was attributed to two factors: (i) the formation of a continuous Cr-rich corundum-type M_2O_3 (M= Cr and Fe) oxide layer that prevented the diffusion of Fe and the formation of a less-protective Fe/Mn-Cr spinel ($[Fe,Mn]Cr_2O_4$) outer layer, (ii) a sufficient residual bulk Cr in the Cr-depleted layer adjacent to the alloy/scale interface that prevented any localized internal oxidation from occurring. A mass balance conducted on the corroded Alloy 33 material suggested that volatilization of the corundum-type oxide layer did not occur, at least not within the short-term exposure in the essentially deaerated SCW. A key issue requiring further study was the observation of intermetallic precipitates that formed below the Cr-depleted zone adjacent to the alloy/scale interface in both alloys when exposed for 500 h at 625 °C and their possible influence on the in-service mechanical integrity.

Keywords: Corrosion resistance, Supercritical water-cooled reactor (SCWR), supercritical water (SCW), Cr content, oxide scale

Acknowledgements

I would like to begin by thanking my supervisors Dr. Joey R. Kish and Dr. Gianluigi A. Botton for their unconditional support and encouragement, their assistance through the project and their patience to bear with me all along in my master's program. I would also like to thank Dr. Wenyue Zheng for sitting in my committee and his effort to read through my thesis. Not to mention the support of my group members who were repeatedly listening to my presentations and passing me constructive feedbacks of my work.

Thanks are also expressed to Carmen Andrei, Glynis de Silveira and Chris Butcher for electron microscopy training, Julia Huang and Travis Casagrande for microscopy assistance, Yinan Jiao for his help in preparing the samples and Dr. David Guzonas and Dr. Joseph R. McDermid for sharing ideas along the project.

I would like to acknowledge the funding to Canada Gen-IV National Program was provided by Natural Resources Canada through the Office of Energy Research and Development, Atomic Energy of Canada Limited, and Natural Sciences and Engineering Research Council of Canada. Also special thanks to CanmetMATERIALS for conducting the SCW corrosion testing.

At last but not least, I would like to thank my family who although is far away from me, has always been a symbol of courage, patience and passion to me, who taught me that I should always try to be my best and never ever give up on my dreams.

Contents

List of Figures

List of Tables

List of Abbreviations

AES	**A**uger **E**lectron **S**pectroscopy
BF	**B**right **F**ield
CI	**C**onfidence **I**ntervals
DF	**D**ark **F**ield
DO	**D**issolved **O**xygen
EDS	**E**nergy **D**ispersive **S**pectroscopy
EELS	**E**lectron **E**nergy **L**oss **S**pectroscopy
F-M	**F**erritic-**M**artensitic
FIB	**F**ocused **I**on **B**eam
FEG	**F**ield **E**mission **G**un
GIF	**G**eneration-IV **I**nternational **F**orum
HT	**H**igh **T**emperature
ICP	**I**nductively **C**oupled **P**lasma
ISE	**I**on-induced **S**econdary **E**lectron
MTC	**M**ill **T**est **C**ertificate
MD	**M**agnetic **D**isc
RD	**R**olling **D**irection

TD	**T**ransverse **D**irection
TT	**T**hrough **T**hickness
SS	**S**tainless **S**teel
SAD	**S**elected **A**rea **D**iffraction
SEM	**S**canning **E**lectron **M**icroscopy
SCW	**S**upercritical **W**ater
SCWR	**S**uper**c**ritical **W**ater-Cooled **R**eactor
STEM	**S**canning **T**ransmission **E**lectron **M**icroscopy
SHS	**S**uperheated **S**team
TEM	**T**ransmission **E**lectron **M**icroscopy
WG	**W**eight **G**ain
WL	**W**eight **L**oss

1. Introduction

The supercritical water-cooled reactor (SCWR) with an increase in thermodynamic efficiency of greater than 45% is one of the six reactor design concepts developed by the Generation-IV International Forum (GIF) [1-4].

Figure 1-1 shows a simplified schematic of the SCWR design concept where the inlet light water (coolant) from the feedwater line enters into the reactor and exits as supercritical water (SCW) via the main steam line where it then enters the turbine-generator system to produce electricity and exists through the cooling water line [5]. The inlet water temperature in the various SCWR design concepts put forth by the participating Generation-IV Forum countries such as EU, Japan, US, Russia, Korea, China and Canada is predicted to range from 280 °C to 350 °C, which results in predicted outlet water temperature range from 500 °C to 625 °C [6]. Of particular interest to this study is the Canadian SCWR design concept, which currently has a predicted inlet water temperature of 350 °C and a maximum outlet SCW temperature of 625 °C, both at 25 MPa pressure [7].

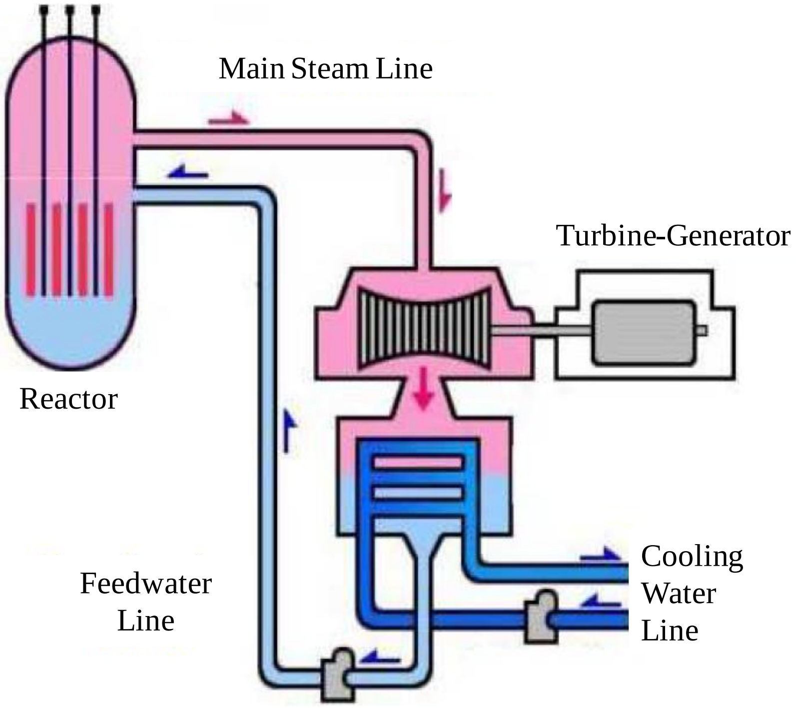

Figure 1-1 A simplified layout of a typical supercritical water-cooled reactor (SCWR) design concept put forth by the Generation IV Forum [5].

Figure 1-2(a) shows a schematic of the current Canadian pressurized tube SCWR design concept [8]. The light water (coolant) flows down a tube that is positioned in the center of each fuel channel, which is the pressurized tube assembly containing an array of fuel pins [Figure 1-2(b)]. At the bottom of the fuel channel, the water coolant flow is directed back upwards while in direct contact with the fuel pins until it exists the outlet plenum as SCW. The proposed design of the fuel channel [Figure 1-2(b)] consists of a pressure tube with 12 mm thickness made of zirconium (Zr) alloy, a 0.5 mm outer linear tube made of Zr alloy, a 5.5 mm non-porous insulator made of yttrium (Y)-stabilized zirconia (ZrO_2) and a 0.5 mm austenitic Fe-Cr-Ni alloy linear tube that holds the fuel pins together. Two fuel cycles are currently being examined for improved performance: (i) 13.4% plutonium (Pu) in thorium (Th) and (ii) 39.7% uranium (U) in Th [9]. An array of fuel pins (62 in one channel) are placed around a central flow tube made of an austenitic Fe-Cr-Ni alloy with 89 mm diameter.

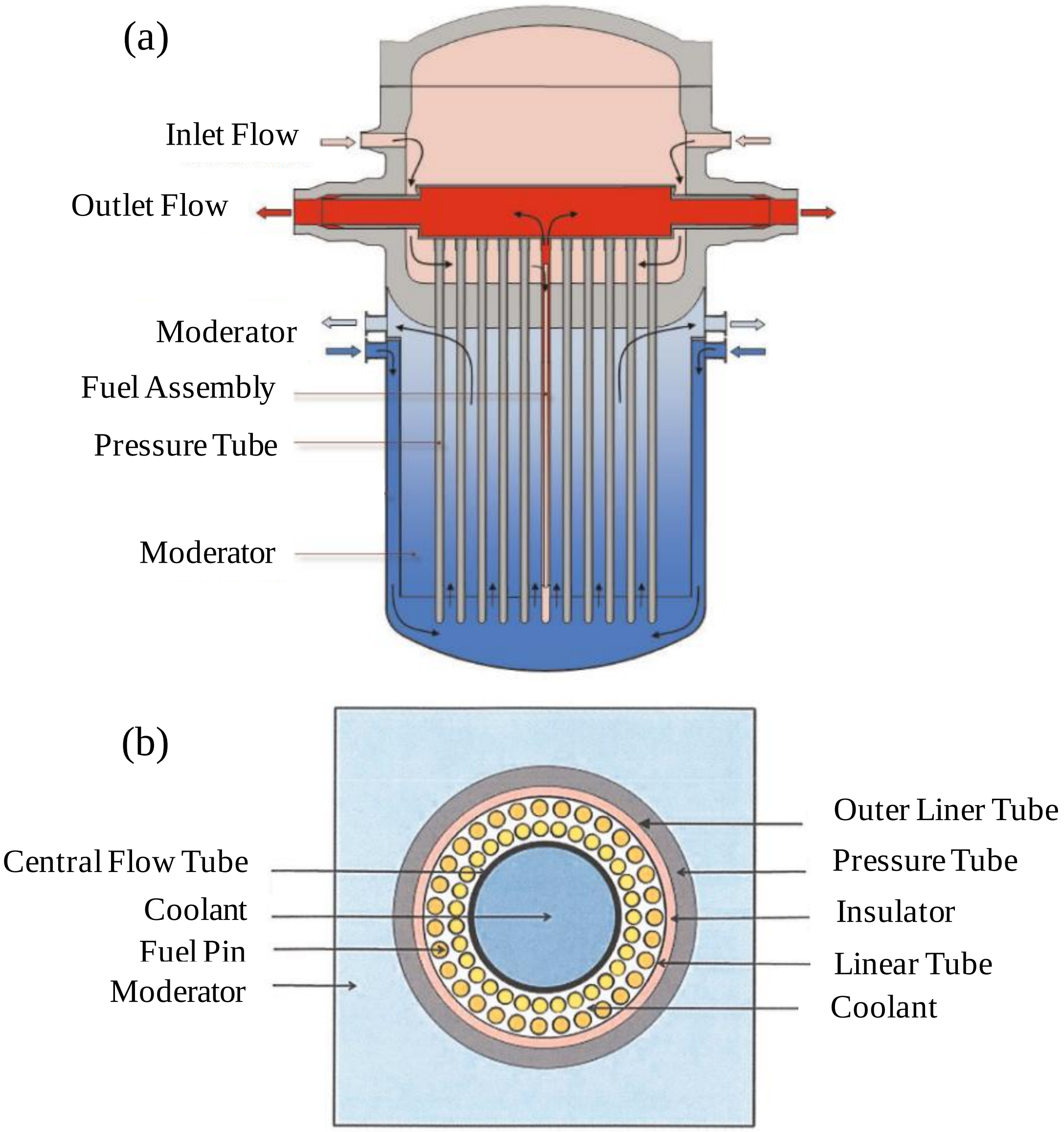

Figure 1-2 (a) Schematic of the in-core design of the Canadian pressurized tube SCWR concept and (b) cross-section schematic of the fuel channel design [8].

Figure 1-3 shows a predicted temperature variation as a function of distance across a fuel pin in the Canadian SCWR design concept [10]. The fuel cladding faces the high temperature fuel at 850 °C on the inside surface and the SCW coolant at 625 °C (maximum) on the outside surface [11-13].

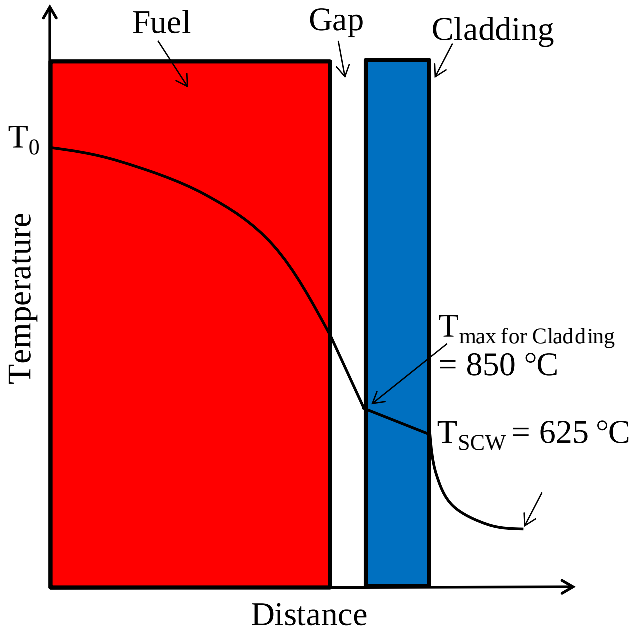

Figure 1-3 A predicted temperature variation as a function of distance in a fuel pin of the Canadian SCWR design concept [10].

As a result, selection of a fuel cladding material that performs well within such circumstances with minimum degradation is a very imperative challenge. Participating Generation-IV Forum countries have been using their preferred fuel cladding materials (mostly conventional austenitic stainless steels e.g. 316L), with the outlet SCW temperature lower than 550 °C (Table 1-1) [10]. While the trend from all the corrosion testing in SCW thus far shows that the higher Cr content, the better the corrosion resistance is, there still exists two knowledge gaps: (i) how much Cr beyond 18 wt.% in conventional 304L/316L stainless steel is needed for acceptable corrosion resistance and (ii) how will these austenitic stainless steels perform at higher SCW predicted outlet temperature (625 °C) in the Canadian SCWR design concept.

Table 1-1 Pressure, inlet and outlet temperatures of coolant for the participating Generation-IV Forum countries [10]

Country	**Pressure (MPa)**	**Inlet Temperature (°C)**	**Outlet Temperature (°C)**
EU/Japan	25	290	510
US	25	280	500
Russia	24.5	290	540
Korea	25	280	510
China	25	280	500
Canada	25	350	625

The purpose of the following work is to characterize the corrosion resistance of candidate higher Cr-containing Fe-Cr-Ni alloys in SCW at two exposure conditions by means of gravimetric measurements and electron microscopy techniques. Firstly, corrosion resistance of coupons exposed in SCW with 25 MPa pressure and 550 °C temperature was considered to be studied to compare the alloy behaviour under well studied conditions from which preferred alloys for other programs have been selected and secondly, corrosion resistance of coupons exposed in SCW with 25 MPa pressure and 625 °C temperature was considered to be examined to understand the mechanism of corrosion and oxidation formation at the maximum anticipated SCW outlet temperature that was developed by GIF.

2. Literature Review

2.1. Key SCW Properties Affecting Corrosion

The supercritical point in water phase diagram is a critical transition point after which increasing the pressure and/or temperature will not result in a distinct liquid-gas phase transformation [14,15]. In other words, in the supercritical region, the liquid and gas phases cannot be distinguished from one another and no boiling occurs [14-16]. Figure 2-1(a) shows the temperature-pressure phase diagram of water with the liquid-gas phase transition boundary shown with the solid line and the supercritical water (SCW) region shown with the orange box. The term SCW is broadly used in the top-right hand corner of water phase diagram where the temperature and pressure is above 374.15 °C and 22.1 MPa respectively (the dashed line in [Figure 2-1(a)]) [14-16]. It has been argued that the whole region after the critical temperature can be considered as the effective SCW phase field since in this area the interaction energy between water molecules is very much smaller than their average thermal energy: hence, a distinct liquid phase formation cannot occur [14,15]. As a consequence, it has also been argued that there exists a meaningful connection between the corrosion behaviour of materials exposed in SCW to that exposed in "superheated steam (SHS)" (steam at temperature above the saturation temperature) [15,17]. Figure 2-1(b) shows the density versus pressure diagram of water for a set of temperatures above the critical temperature [15]. Unlike the behaviour observed at the lower temperatures, water density at 600 °C changes in a linear manner as the pressure is increased from low values typical of SHS (5-10 MPa) to high values typical of SCW (25 MPa). This linear dependence is consistent with the notion that there is a meaningful connection between SCW and superheated steam.

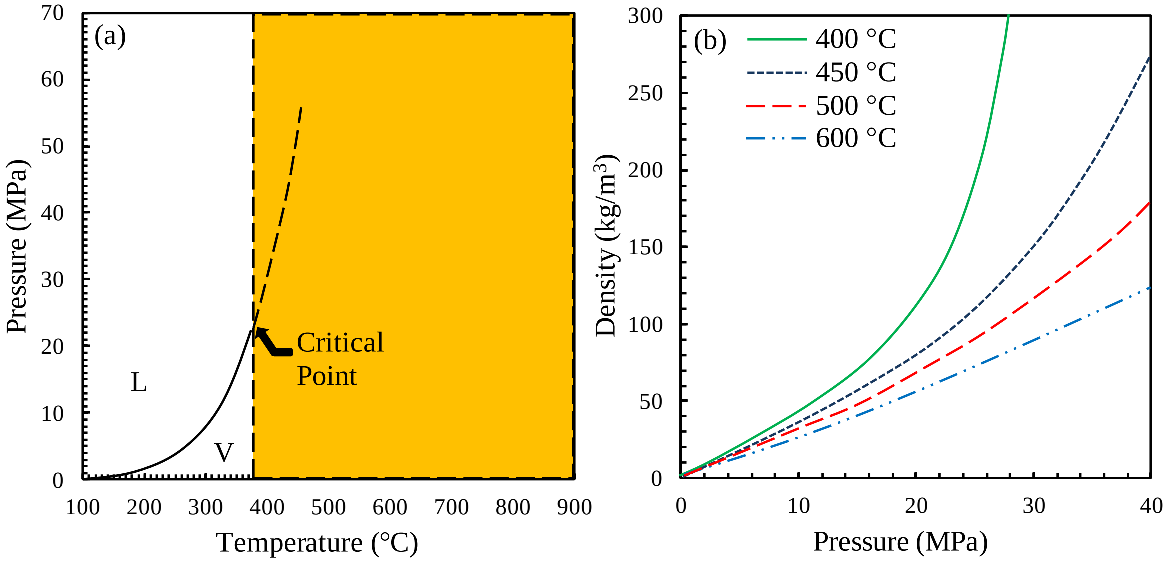

Figure 2-1 Temperature-pressure phase diagram of water showing the SCW region in the orange box and (b) density-pressure diagram of water for the temperatures of 400 °C, 450 °C, 500 °C and 600 °C [15].

Figure 2-2(a) shows the changes in the dielectric constant as a function of temperature for several supercritical pressures [15]. The dielectric constant sharply drops to a value of about 2 for each pressure considered as the temperature is increased in excess of the critical temperature. The small value of dielectric constant can be directly related to the ionic product (pK_w) and pH [Figure 2-2(b)] [15]. As Figure 2-2(b) shows, a minima exists in the temperature dependence of both pK_w and pH, which coincides with the critical temperature [15]. The relative high value of the pK_w particularly at the lower supercritical pressures (circa 25 MPa) for temperatures in excess of the critical temperature reveals that the SCW phase is essentially a non-polar solvent. This change in property for SCW, particularly at lower supercritical pressures (circa 25 MPa), has two important implications regarding the corrosion of materials: a significantly reduced ability to dissolve protective metal oxides and a significantly reduced ability to support electrochemical reactions.

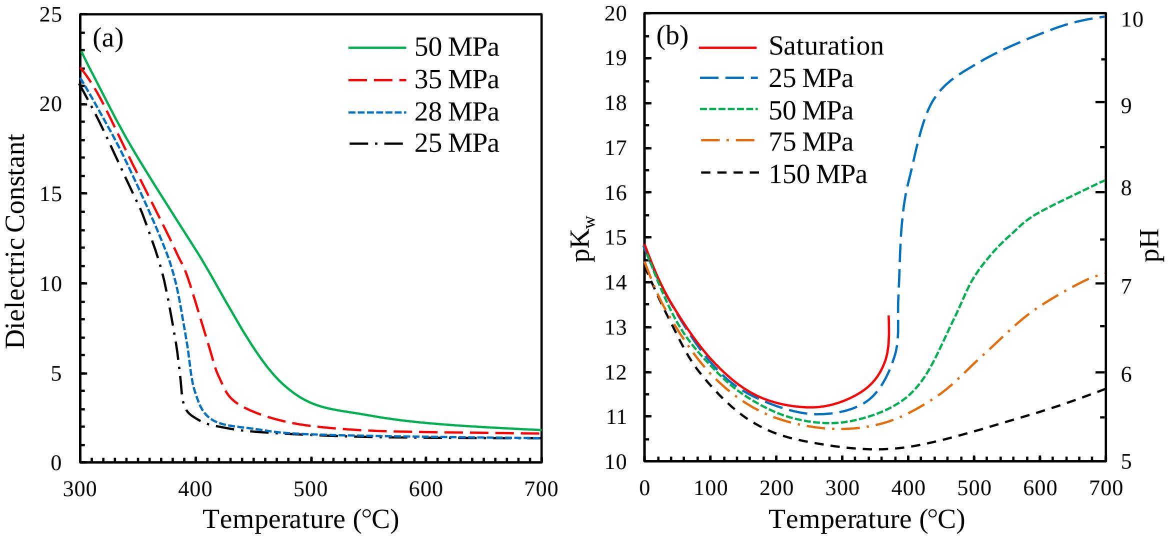

Figure 2-2(a) Dielectric constant and (b) pK_w and pH of water as a function of temperature for several supercritical pressures [15].

Figure 2-3 shows the thermodynamically calculated concentration of dissolved soluble oxides in neutral water [18]. A large drop in oxide solubility is predicted to occur across the critical temperature in response to the simultaneous decrease in the dielectric constant as the SCW becomes dominated with uncharged species [15]. Among the dissolved soluble oxide curves shown in Figure 2-3, Fe_3O_4 and Cr_2O_3 graphs are of particular interest with Cr_2O_3 having the most dissolving capability in SCW. The former (Fe_3O_4) has been repeatedly reported to be formed as an outer oxide layer on conventional austenitic stainless steels in SCW [19-22]. Cr_2O_3 layer has been reported as the major phase to be formed in high Cr-containing alloys when exposed at the elevated temperatures [23-25] (fewer studies were done on Cr_2O_3 forming alloys in SCW).

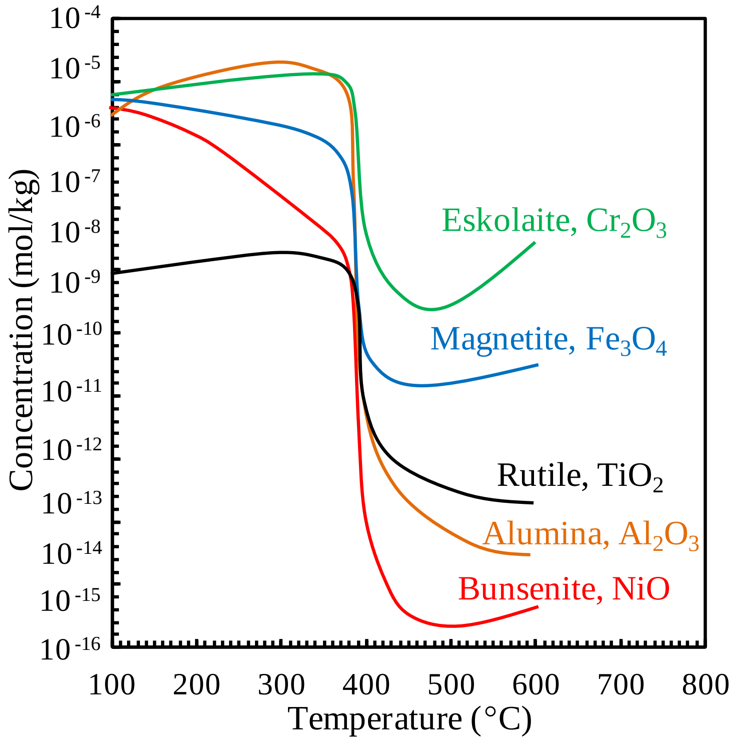

Figure 2-3 Thermodynamically predicted metal oxide solubility in water as a function of temperature at 25 MPa [18].

As implied previously, another characteristic of SCW is its ability to transit the electrochemical oxidation into chemical oxidation. D. Guzonas et al. [15] explained this transition in details. They implied that each fuel channel inside the reactor core can be divided into two regions (Figure 2-4): (i) near the inlet coolant area with small temperature increase in the bulk coolant and cladding surface and large drop in the coolant density to around 100 kg/m^3 and (ii) close to outlet coolant area with the rapid increase in the bulk coolant and cladding surface temperature while the density is almost constant. At the sub-critical region in water phase diagram (corresponding to area 1 in Figure 2-4), corrosion is an electrochemical process. This means a so-called electrical double layer will be formed on the alloy surface where the oxidation-reduction half reactions occur and corrosion continues as long as both electron transport within the alloy and ion transport in solution between anodic and cathodic sites exist (considering that the ion solubility in this region is high). As the temperature increases and the pressure drops (corresponding to area 2 in Figure 2-4), the dielectric constant and ionic conductivity decreases (Figure 2-4), therefore the ion transport in the solution reduces rapidly and a favorable transition from electrochemical oxidation to chemical oxidation occurs. The transition area where both electrochemical and chemical reactions might occur is shown with a yellow box in Figure 2-4. After the transition is completed, due to lower oxide solubility in SCW, nearly all of the oxidized metals remain on the surface and corrosion continues by the inward diffusion of anions (oxygen ions) and outward diffusion of cations through the vacancies in this layer which therefore, reduces the corrosion rate.

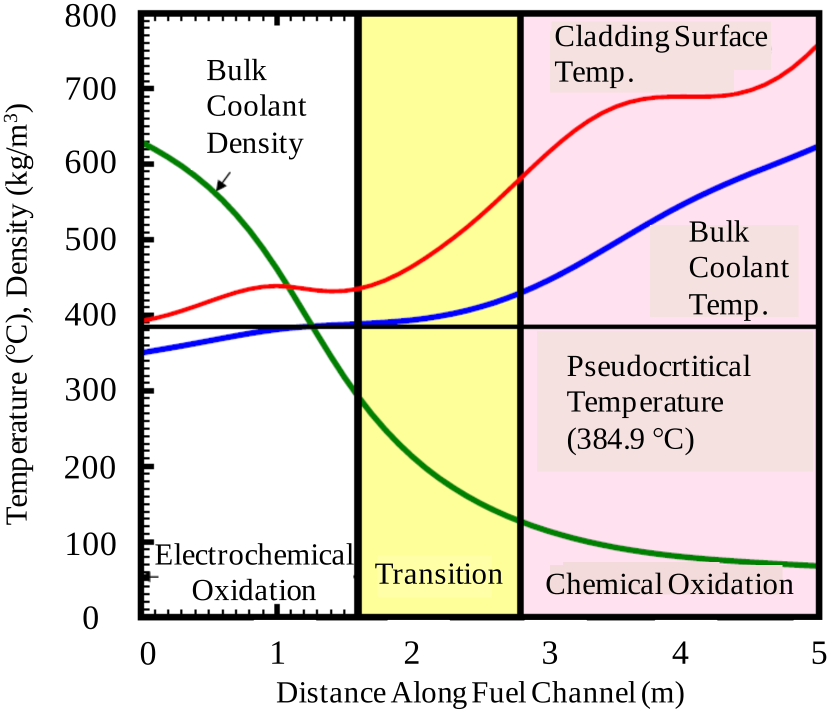

Figure 2-4 Calculated typical temperature and density variation along a fuel channel in Canadian SCWR design with 25 MPa SCW, inlet water temperature of 350 °C and outlet water temperature of 625 °C [15].

2.2. Fe-Cr-Ni Austenitic Stainless Steels in SCW

Over the past few years, several potential candidate materials have been examined to be used as the fuel cladding in SCWR such as: ferritic-martensitic (F-M) steels, austenitic stainless steels, nickel (Ni)-based alloys and titanium (Ti)-based alloys among which austenitic stainless steels have shown propitious corrosion and irradiation resistance [26-28]. Table 2-1 demonstrates the comparison between corrosion resistance, radiation damage resistance and high temperature (HT) mechanical integrity of the aforementioned alloys [29]. As can be seen, austenitic stainless steel with high Cr content (>18.5-20 wt.%) have shown promising corrosion and stress corrosion cracking resistance when exposed in SCW. It is noted that the emphasis of this work is placed on the corrosion resistance alone. A study of the stress corrosion cracking resistance deserves a separate research effort.

Table 2-1 Corrosion resistance, radiation damage resistance and HT mechanical integrity comparison between candidate fuel cladding materials [29]

Alloy Type	**Corrosion Resistance**		**Radiation Damage Resistance**		**HT Mechanical Integrity**
	General Corrosion	**SCC**[1]	**Swelling**[2]	**Embrittlement**[3]	
F-M Steels	Medium	High	High	High	Low
Austenitic Stainless Steels (Cr < 18.5-20 wt.%)	High	Medium	Low	High	Medium
Austenitic Stainless Steels (Cr >18.5-20 wt.%)	High	Medium	High	Limited Data	High
Ni-Based	High	Medium	Low	Medium	High
Ti-Based	Medium	Limited Data			Medium

[1] Stress corrosion cracking (SCC) is a simultaneous effect of stress, corrosive environment and susceptible material that forms crack in the sample.

[2] Swelling is an increase in the alloy volume as a result of very strong radiation.

[3] Embrittlement means the loss of ductility due to presence of hydrogen and helium in SCW or neutron radiation.

Up until now, a large amount of studies (e.g. L. Zhang et al. [30], G.S. Was et al. [31], D. Guzonas [32]) on 300-series stainless steel to be used as the cladding material in SCW has been published. Austenitic stainless steels have shown very low oxidation rate at temperatures below 550 °C when exposed in SCW which is comparable with Ni-based alloys [30]. However, their corrosion rate at higher temperatures increases more rapidly [30]. D. Guzonas et al. [32] implied that the role of relative parameters on general corrosion rate that is measured in different studies in the order of decreasing importance is as following: temperature ≈ surface finish > water chemistry > SCW density. Surface finishing methods (e.g. grinding, polishing, electropolishing, etc.) can result in huge differences in the corrosion results obtained from different studies [32]. Coupons that were prepared by electropolishing have shown a strain-free surface resulting in the maximum general corrosion compared to those prepared by grinding [32]. The latter provides severe cold-work in the coupons which reduces general corrosion rate significantly [32]. In addition, many experiments have been preformed with low (25 ppb) up to high (8000 ppb) dissolved oxygen (DO) concentrations implying that although the corrosion rate enhances with the increase in the amount of DO, the effect is not huge [32]. The effect of decrease in SCW pressure is its corresponding ability to decrease the oxide solubility as discussed in section 2.1. Figure 2-5(a) and Figure 2-5(b) show the Scanning Electron Microscopy (SEM) images obtained from a 316L stainless steel (SS) exposed in SCW flow loop for 500 h in plan-view and cross-section respectively. The dominant oxide phase and details of exposure test are also shown in the images. The oxide scale on 316L SS (~ 16.5 wt.% Cr) showed a double layer structure based on SEM/EDS analysis: an inner layer of spinel $[Fe,Ni,Cr]_3O_4$ and an outer layer of magnetite (Fe_3O_4) oxide due to outward diffusion of Fe from the alloy [33]. Figure 2-5(c) and Figure 2-5(d) show the SEM images obtained from an Alloy 800H (~ 20 wt.% Cr) exposed in SCW for 3000 h in plan-view and cross-section respectively [34]. L. Tan et al. [34] showed that the dominant oxide phases in Alloy 800H after long-term exposure in SCW are an outer Fe_3O_4 scale and an inner $[Fe,Cr]_3O_4$ scale. They also explained the formation of mushroom shape oxide areas in the substrate with $FeCr_2O_4$ structure as a result of the difference between the elements lattice and grain boundary diffusion coefficients. Figure 2-5(e) and Figure 2-5(f) show the recently reported SEM images obtained from a 310H SS (~ 25 wt.% Cr) exposed in SCW for 650 h in plan-view and cross-section respectively [35]. Increasing the Cr content in the austenitic SS, resulted in a huge decrease in the oxide scale thickness and changed the oxide structure to a more protective chromia (Cr_2O_3) layer. These observations bring the attention to study the mechanism of oxidation in high Cr-containing alloys that has equal to/more than 25 wt.% Cr when exposed in SCW since only few studies have been performed on such alloys (with ~ 25 wt.% Cr) and almost none on the exceeding (> 25 wt.% Cr) Cr-containing alloys such as Alloy 33 (~ 33 wt.% Cr).

As explained in Figure 2-1(b), the SCW behaviour is very much the same as the 100% SHS as the density behaviour has a linear change with temperature [15]. D.

Guzonas et al. [15] and A.T. Motta et al. [36] showed the similarity in general corrosion rate observed between several candidate alloys in SCW and SHS. As a result, the mechanism of oxide scale formation in SCW can be assumed to be somewhat similar to that in SHS. The following sections will therefore be dedicated to explain the thermodynamics and kinetics of alloy oxidation at the high temperature steam environment to better understand the oxidation mechanism in SCW.

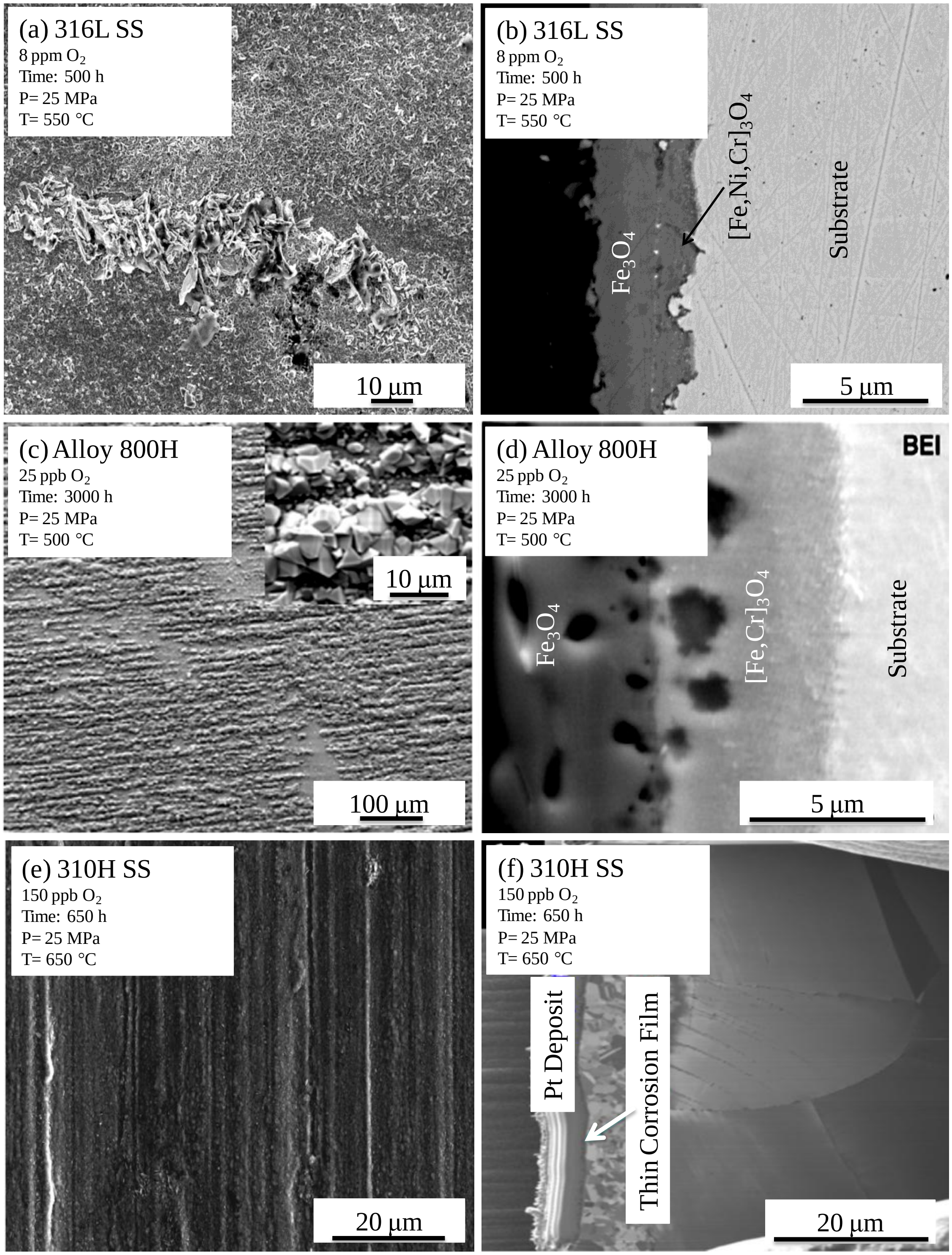

Figure 2-5 (a) Plan-view and (b) cross-section SEM images of 316L SS, (c) plan-view and (b) cross-section SEM images of Alloy 800H [33] (e) plan-view and (f) cross-section SEM images of 310SS [35] exposed in SCW.

2.3. Basic Fundamentals of Alloy Oxidation

Wagner [37] has classified simple types of oxidation into two categories. One involves a noble parent A with a reactive alloying element B, in which the noble parent is composed of elements such as Pt, Ag, Au, etc. that does not oxidized in the oxidizing environment and alloying elements such as Cr, Ni, Mn, Si, etc. that can form stable oxides in such environment [38]. Figure 2-6(a) shows the concentration profile of the reactive element B as a function of distance (x) in the alloy [39-41]. In the simplest case when diffusion coefficient of B (D_B) is less than that for O, $D_B << D_O$, BO_υ (stable oxide) forms internally in the alloy. The depth of the internal oxidation as a function of time [x(t) (cm)] can be calculated from equation (eq.) 1 [38].

$$x(t) = \left[\frac{2N_O^{(s)} D_O t}{N_B^{(O)}}\right]^{\frac{1}{2}} \tag{1}$$

$N_O^{(s)}$: Oxygen solubility in A (at%)

$N_B^{(O)}$: Bulk alloy concentration of B in A (at%)

D_O: Diffusivity of oxygen (cm^2/s)

t: time (s)

Eq. 1 readily shows that an increase in the concentration of the reactive element B decreases the depth of internal oxidation. The depth decreases until a time at which the concentration of B reaches some critical value, N_B^{crit} (at%) [Figure 2-6(b), eq. 2] at which the internal oxidation transforms into external oxidation and promotes the formation of a continuous external oxide of BO_υ [39-41].

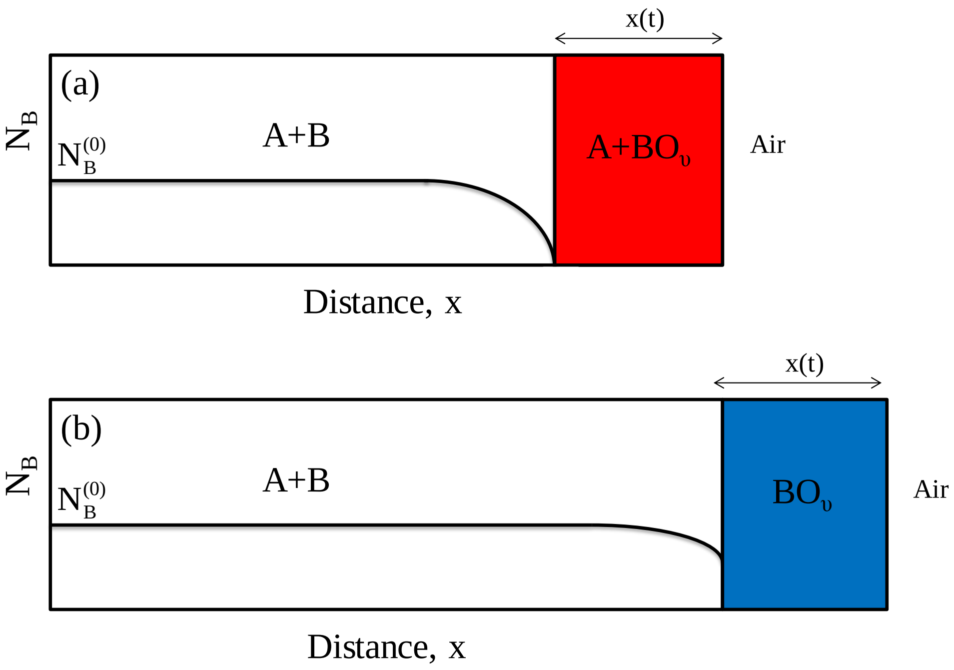

Figure 2-6 Concentration profiles of the reactive element B alloying in a noble parent for (a) a concentration of B lower than the critical value and (b) a concentration of B higher than the critical value [39-41].

$$N_B^{crit.} = \left[\frac{\pi g^*}{2} N_O^{(s)} \frac{D_O V_m}{D_B V_O}\right]^{\frac{1}{2}} \tag{2}$$

g^*: Critical volume fraction of oxide for transition ≈ 0.3

V_m: Molar volume of metal (dm^3/mol)

V_O: Molar volume of oxide (dm^3/mol)

D_B: Diffusivity of B (cm^2/s)

The other type of oxidation involves a non-noble parent with a reactive alloying element; in which the parent alloy is composed of Fe, Ni, Co, etc. that forms a moderately stable oxide and a reactive alloying elements such as Cr, Si, Al, etc. that forms a very high stable oxide [38]. Figure 2-7(a) shows the condition in which the alloy is composed of a dilute solution of B in A. In this case, a stable oxide of BO_υ forms initially due to the higher stability of the oxide when mixed with A. As soon as B is depleted in the alloy, an external oxide of AO forms on the oxide/air interface [39-41]. As the concentration of B in the alloy increases, a continuous external BO_υ forms at the alloy/air interface [Figure 2-7b)] [39-41]. For longer exposure times, more depletion of B in the alloy/oxide interface results in the formation of AO precipitates within the external BO_υ oxide [Figure 2-7(c)] [39-41].

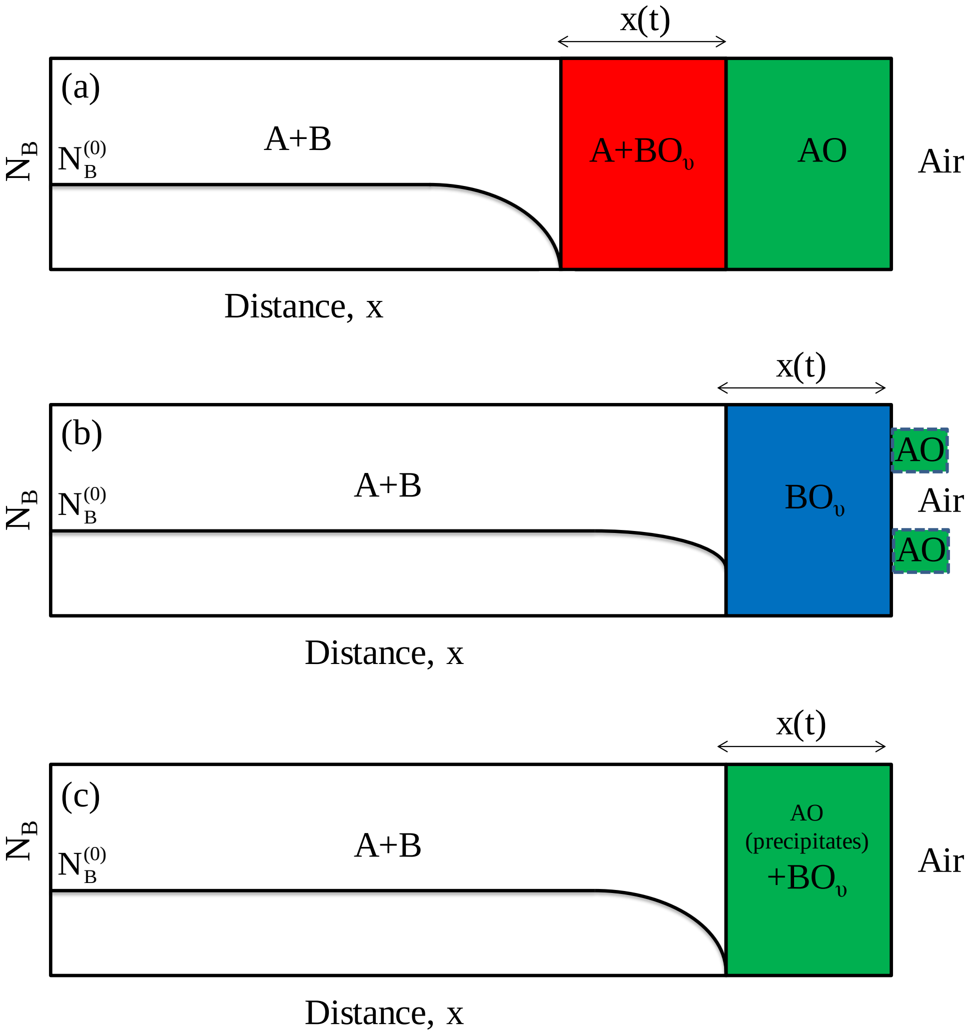

Figure 2-7 Concentration profiles of the reactive alloying element B in a non-noble parent for (a) a concentration of B lower than the critical value, (b) a concentration of B greater than the critical value after a short exposure time and (c) a concentration of B greater than the critical value after a long exposure time [37-39].

It should be noted that Figure 2-6 and Figure 2-7 simply describe a steady-state oxidation situation. More realistically speaking, AO forms along with BO initially until

BO becomes uniform (and, thus protective). This refers to "transient oxidation" [38] (shown in Figure 2-7(b) with the dashed green rectangles). This specially happens in the case where the concentration of B in the depleted zone in the substrate is lower than the critical value resulting in the easier diffusion of A through the depleted zone to form the oxide [38].

2.4. Basic Fundamentals of Steam Oxidation

G. Wright et al. [42] wrote a detailed review on the oxidation behaviour of alloys that could be used in steam boilers with a typical temperature range of 541-566 °C and a pressure up to 23.8 MPa. From the thermodynamic point of view, in an oxidizing environment for example when O_2 is provided from water dissociation in SCW (eq. 3), the most simplified type of an oxidation reaction can be written as eq. 4 where a single reactive element (M) with the activity of unity is oxidized by O_2 [38-42]. The corresponding Gibbs free energy equation for eq. 4 is given in eq. 5, in which ΔG^0 is Gibbs free energy in J/mol, R is the gas constant equal to 8.314 J/mol.K, T is the temperature in K, pO_2 is the oxygen partial pressure from water dissociation (eq. 3) in atm, $a_{M_xO_{y(S)}}$ is the oxide activity and ${a_M}^x$ is metal activity (assumed to be unity).

$$H_2O_{(g)} = \frac{1}{2}O_{2\,(g)} + H_{2\,(g)} \tag{3}$$

$$xM_{(s)} + \frac{y}{2}O_{2\,(g)} \leftrightarrow M_xO_{y\,(s)} \tag{4}$$

$$\Delta G^0 = -RT\ln K = -RT\ln\left(\frac{a_{M_xO_{y(S)}}}{({a_M}^x.(p_{O_2})_{dissosiation}{}^{\frac{y}{2}})}\right) \tag{5}$$

If the oxygen partial pressure in steam (eq. 3) is higher than that obtained from the eq. 4 [$p_{O_2} > (p_{O_2\,dissociation})$] a stable oxide of the element M can be formed. While the initial oxidation reaction is very fast, as the oxide layer grows, the oxidation rate decreases and the oxygen partial pressure in the gas will be controlled by the diffusion rate of O and M ions in the scale. If the oxide scale formed on M is adherent and free of short circuit paths (e.g. pores, cracks, grain boundaries), in other words, protective enough, then the oxide layer can act as a diffusion barrier that protects the metal against further oxidation [43,44]. In the case of alloys with several reactive elements, "selective oxidation" occurs. Oxides that are more thermodynamically stable starts to form first adjacent to the alloy/gas interface, whereas less stable oxides form afterwards [42]. A multi-layer oxide scale therefore forms on the alloy and the protection capability of the oxides then depends on the diffusion rate of oxidizing species from the alloy and gas through the multi-layer scale [42].

Figure 2-8 shows a version of the well-known Ellingham diagram [45], which graphically illustrates the thermodynamically stable oxides that can form in the steam at a particular oxygen partial pressure. The O partial pressure in 25 MPa SCW (of interest to the current work) from water dissociation is calculated with FactSage software [46] to be $10^{-8.85}$ atm. The sequence of oxide formation in a Fe-Cr-Ni alloy with Al, Ti, Si, and Mn minor alloying elements, from the most stable to the least stable oxides in the temperature range of 600 °C will therefore be: Al_2O_3, TiO_2, SiO_2, MnO, Cr_2O_3, FeO, Fe_3O_4, Fe_2O_3 and NiO.

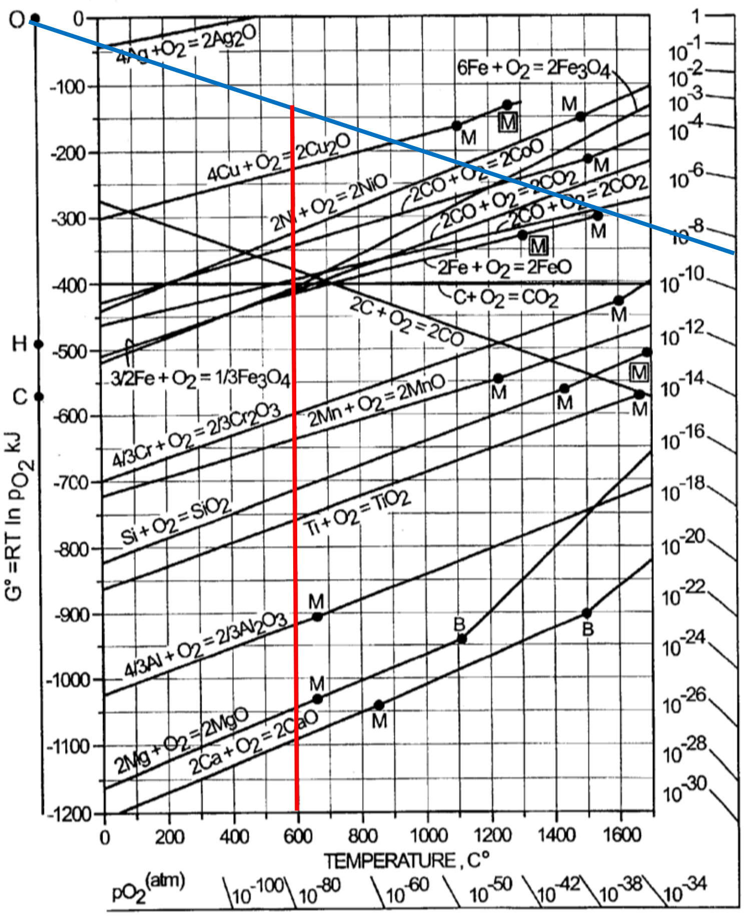

Figure 2-8 Ellingham diagram and the thermodynamically stable phases at the temperature of 600 °C and the pressure of $10^{-8.85}$ atm [45].

Kinetics of oxidation in steam (similar to that in SCW) can be explained by their growth rate which follows a parabolic law (eq. 6). This means that as the oxide thickness increases, the thickening of the oxide decreases and the rate of the oxidation is controlled by ion diffusion through the scale.

$$x^2 = 2k_p t \qquad (6)$$

x: Oxide thickness (cm)

k_p: Parabolic rate constant (cm^2/s)

t: Time (s)

Was et al. [31] discussed the temperature dependence of parabolic rate constant in Alloy D9 after 1026 h exposure in SCW. They showed that temperature increase results in the oxidation kinetics change from linear to parabolic rate [Figure 2-9(a)]. They also showed a complex effect of DO [Figure 2-9(b)]. They reported that at shorter times the higher DO (2000 ppb) content, the smaller weight gain was, whereas at longer exposure times, (300-500 h) the alloy oxidation rate exposed in high DO content SCW increased drastically. Not to mention in lower DO content SCW test, increasing the exposure time reduced the oxidation rate in parabolic law (scattered data obtained could be explained by oxide spallation in these alloys).

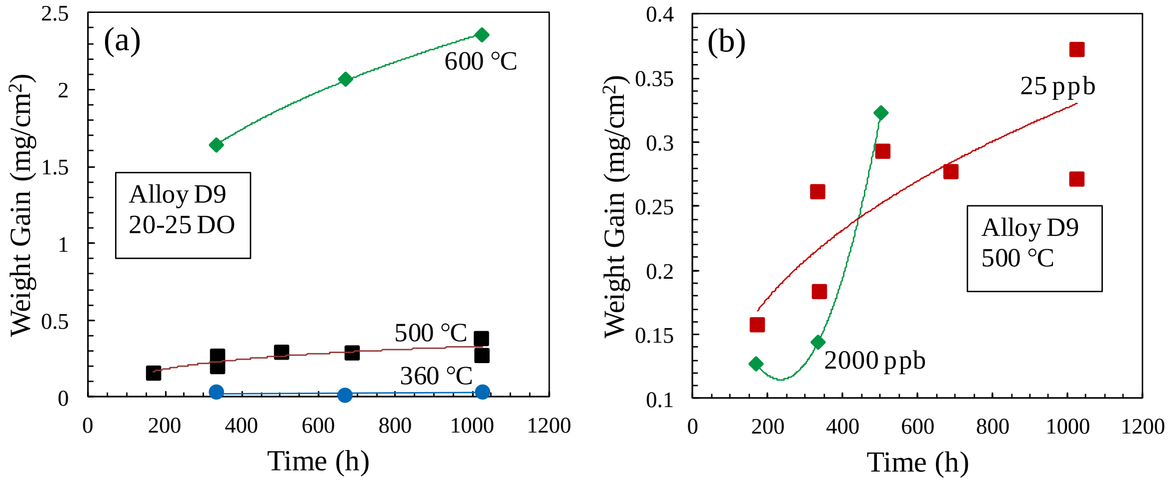

Figure 2-9 Weight gain (mg/cm^2) versus time (h) graph of Alloy D9 for (a) 20-25 ppb DO at the temperatures of 600 °C, 500 °C and 360 °C and (b) 500 °C exposure test for 25 ppb and 2000 ppb DO.

Y. Nishiyama et al. [47] reported that for a short-term test run (100 h) of austenitic stainless steels in steam, the oxidation rate decreases with the increase in the alloy Cr content. They mentioned that a Cr content of around 22 wt.% is necessary for this drop in the oxidation rate. G. Wright et al. [42] explained the role of surface finishing in the oxidation kinetics. They implied that the cold worked surfaces provide a more protective and Cr-rich oxide scale due to the presence of more Cr diffusion paths (similar to the alloys with finer grain size). The formation of such Cr-rich scales will then reduce the oxidation (corrosion) rate and favors the parabolic rate of oxidation.

It is well known that increasing the Cr content in an austenitic Fe-Cr-Ni alloy enhances its ability to form a protective Cr-rich corundum-type [M_2O_3 (M=Cr and Fe)] layer in the absence of oxide evaporation [42,48,49]. While a Cr content of approximately 20 wt.% in a Fe-Cr-Ni alloy is necessary for an external Cr-rich M_2O_3 to form [50,51], it has been reported that a Cr content of more than 25 wt.% is essential for the formation of a more uniform Cr_2O_3 layer that mostly reduces ion diffusion [52]. One major concern in increasing the Cr content within an alloy however, is the possible formation of volatile species at elevated temperatures [42, 53-57]. The Cr_2O_3 layer formed on such alloys can react with the oxygen provided from the water dissociation to form the oxy-hydroxide $CrO_2(OH)_2$ (eq. 7) [53-55].

$$1/2\ Cr_2O_{3(s)}+H_2O+3/4\ O_2= CrO_2(OH)_{2(g)} \tag{7}$$

Formation of the $CrO_2(OH)_2$ consequently removes the Cr_2O_3 layer from the surface [56]. To compensate such Cr loss, there needs to be more Cr present in the alloy to diffuse to the alloy/oxide interface in order to re-form the protective Cr_2O_3 layer. M. Halvarsson et al. [56] suggested that once the Cr vaporization from the corundum-type scale reaches a critical value, there will no longer be enough Cr supply from the substrate to the scale, therefore the oxide scale will lose its protectiveness and breakdown occurs. The critical value of this Cr vaporization from the Cr_2O_3 layer however has not been precisely measured elsewhere. H. Asteman et al. [57] pointed out that as the volatile species forms on the surface of a Cr_2O_3 layer, their diffusion into the gas environment highly depends on the gas velocity; the higher the flow rate, the easier the volatile species can be carried away. G. Wright et al. [42] also, argued that the Cr loss is very small in a steam at temperature up to 650 °C and a pressure up to 24 MPa, but it increases with a further increase in the oxidizing power of the environment (temperature, pressure, oxygen partial pressure, etc.).

2.5. Oxide Scales Characterization

Oxide characterization is typically done in plan-view and cross-section using SEM techniques when the oxide scale is relatively thick. This is because the electron interaction volume with the oxide scale (Figure 2-10) will not exceed the thickness of the oxide layer, therefore there will not be any additional data/signals from the substrate that could interfere the analysis of the oxide scale.

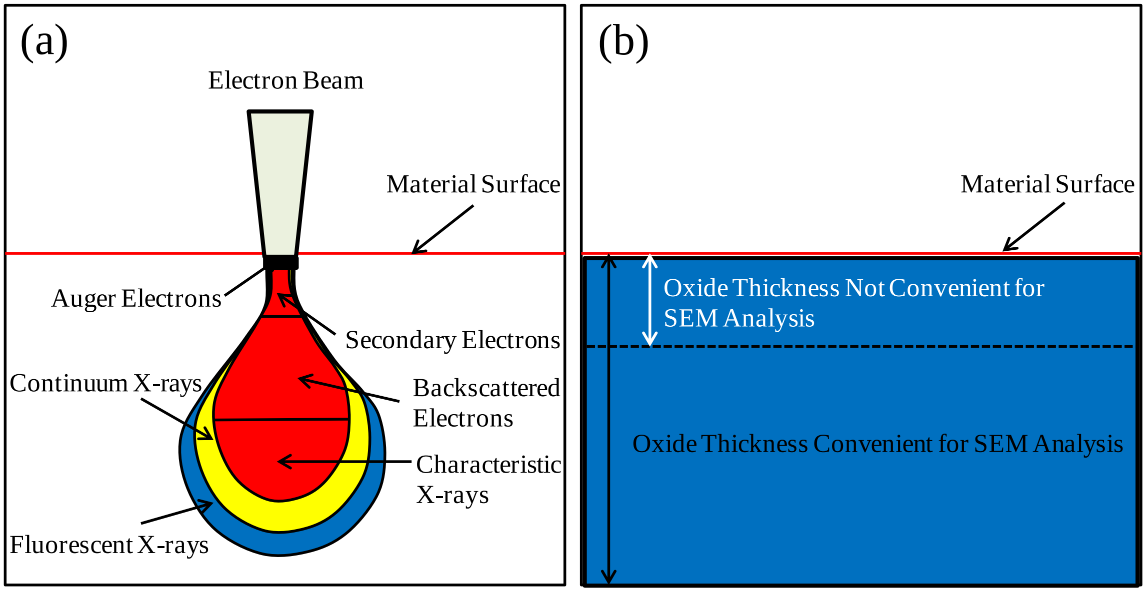

Figure 2-10(a) Electron interaction volume and the corresponding signals and (b) a typical convenient (black arrow) and not convenient (white arrow) oxide thickness for SEM analysis in cross-section.

In the case of thinner oxides (oxides about 100 nm thick within a multi-layered scale), SEM analysis cannot provide any meaningful chemical information about the oxide composition. The major method of analysis that was chosen in the current study to address this limitation is Electron Energy Loss Spectroscopy (EELS) in Scanning Transmission Electron Microscopy (STEM). EELS measures the amount of energy that has been lost after electron interaction with the very thin TEM sample which can be measured by magnetic fields in TEM [58]. EELS qualitative analysis is obtained by measuring the amount of energy loss (eV) for each of the edges that is observed in a typical EELS spectrum. EELS edges energies will be close to characteristic X-rays for each element, therefore comparing the energy loss with that for reference materials can give information on the elemental composition of the material. For characterizing different types of oxides formed on an austenitic Fe-Cr-Ni alloy, O-K, Cr-$L_{2,3}$, Fe-$L_{2,3}$, and Ni-$L_{2,3}$ edges can all be used for oxide analysis. However, the O-K edge typically shows more variation in each oxide type: thus, making the analysis more straight forward. Figure 2-11 shows the reference EELS and energy loss near-edge structure (ELNES) spectra [58-62] that were used as reference in the current study as re-plotted using the Plot Digitizer software [63].

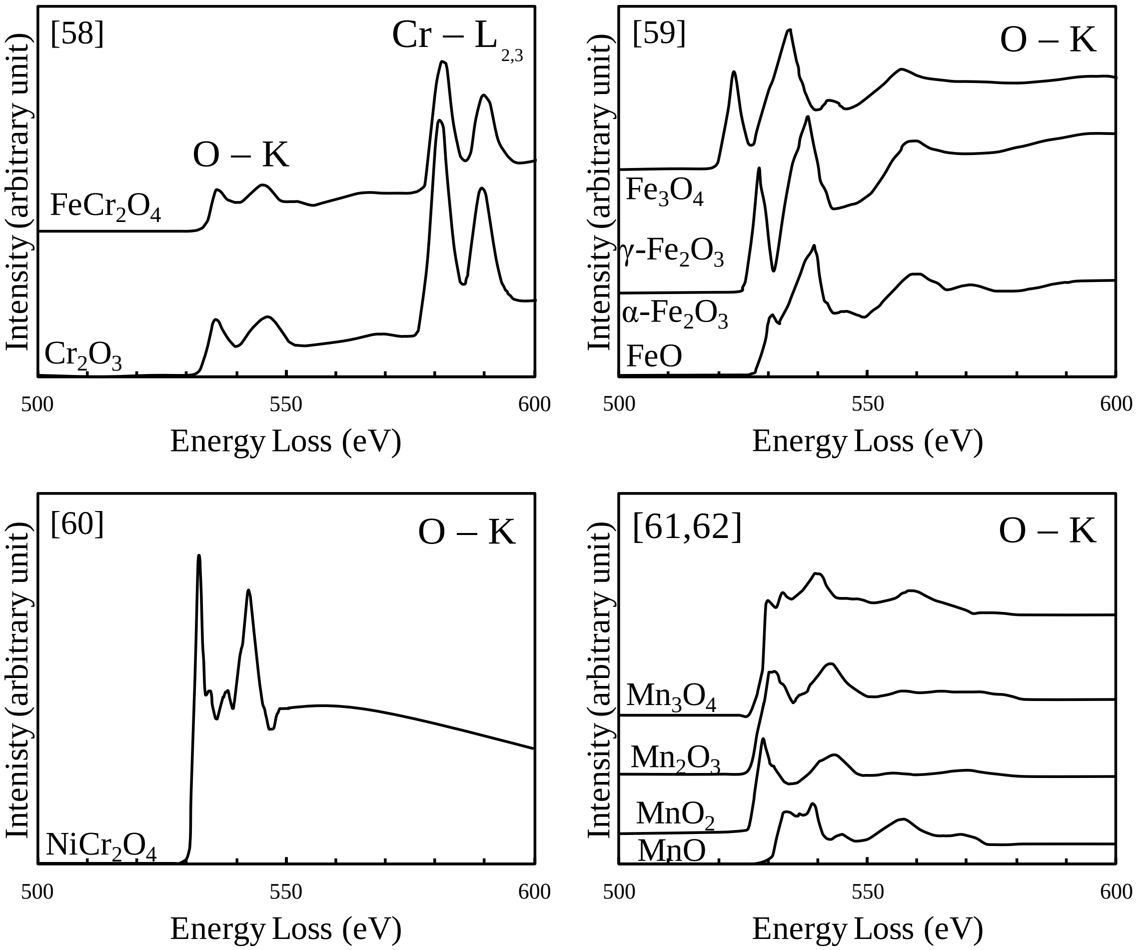

Figure 2-11 EELS spectra for $FeCr_2O_4$ and Cr_2O_3, FeO, α-Fe_2O_3, Fe_3O_4 and γ-Fe_2O_3, $NiCr_2O_4$ (ELNES), and MnO, MnO_2, Mn_2O_3, Mn_3O_4 in reference compounds [58-62].

3. Experimental Procedures

3.1. Material

Rectangular test coupons of Alloy 800HT (20×10×1 mm) and Alloy 33 (25×5×1 mm) were prepared from commercial cold-rolled and annealed plates using a diamond wheel saw. A 2 mm diameter hole was then drilled out near the top of each coupon to facilitate mounting the coupons on a coupon tree during the experiment. Figure 3-1 shows a schematic of each alloy coupon along with their dimensions, the rolling direction (RD), the transverse direction (TD) and the through thickness (TT) direction.

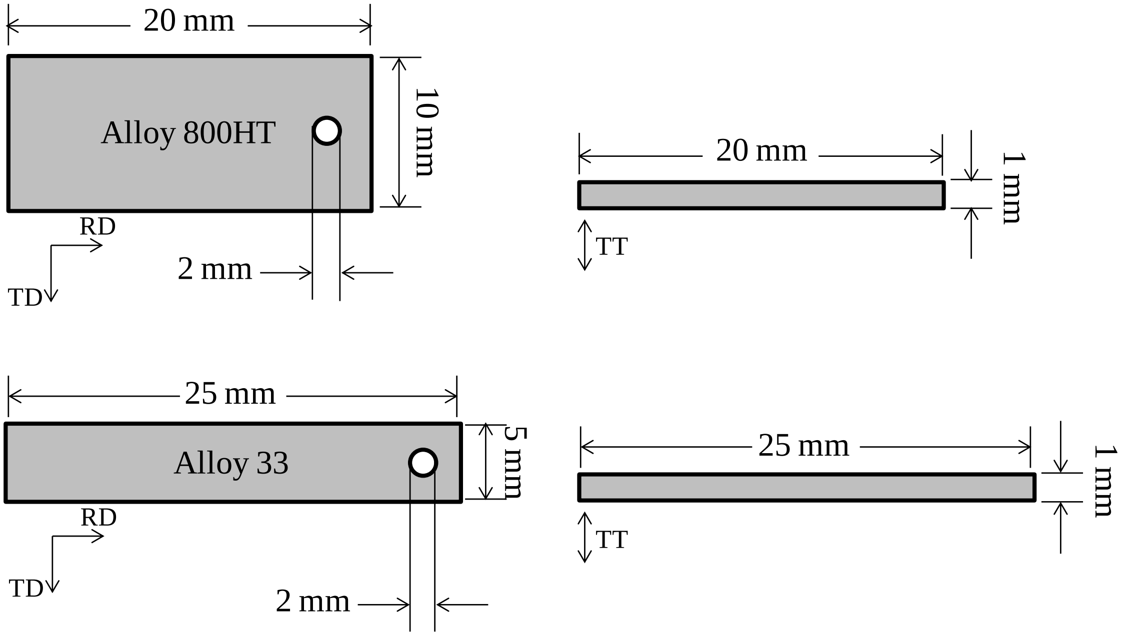

Figure 3-1 Dimensions of Alloy 800HT and Alloy 33 coupons prepared by diamond wheel saw.

The chemical compositions of the alloys are listed in Table 3-1. Information about the chemical composition of Alloy 800HT and the material sheet preparation was obtained from the Mill Test Certificate (MTC) and the Allegheny Ludlum Corporation according to ASTM B409-01. The chemical composition of Alloy 33 was acquired using

Inductively Coupled Plasma (ICP) spectrometry according to ASTM E1019-11, E1097-12 (modified) and E1479-99 performed by Cambridge Materials Testing Limited.

Table 3-1 Composition (wt%) of Alloy 800HT and Alloy 33

Alloy	Fe	Cr	Ni	C	Mn	Si	Cu	Ti	Al	Mo	N	Ce	S	P	Co
800HT	Bal.	20.6	30.7	0.07	0.6	0.3	0.03	0.6	0.5	-	-	-	<0.01	0.01	0.03
33	Bal.	33.4	31.9	0.01	0.6	0.2	0.5	<0.01	-	1.5	0.4	0.02	-	-	-

One coupon from each alloy (in the mill-annealed condition) was mounted in cross-section. Mounting was completed using a CitoPress-10 electro-hydraulic, programmable single cylinder mounting press machine. Approximately 30 g of bakelite powder was used for hot mounting the coupons. This process took 15 minutes including 10 minutes of heating the bakelite powder to 180 °C for sintering and 5 minutes of cooling. An automatic Struers Multidoser machine was used afterwards to polish the mounted samples. Table 3-2 shows the grinding and polishing steps followed to attain a mirror surface finish for each alloy.

Table 3-2 List of grinding and polishing steps used

Step	Surface	Lubricant	Time (min.)	Force (N)	RPM*	Direction*
1	SiC 800 #	Water	1:30	25	300	>>
2	SiC 1200 #	Water	1:30	20	300	>>
3	SiC 2400 #	Water	1:30	20	300	>>
4	SiC 4000 #	Water	1:30	20	300	>>
5	MD*-Dac 3 μm	Blue*	5:00	20	150	><
6	MD-Dur 1 μm	Blue	5:00	20	150	><

RPM: Rotations Per Minute
Direction: >> Clockwise, >< Counter clockwise
MD: Magnetic Disk
Blue: 80% Ethanol + 10% Ethylene Glycerol

After each grinding step, the coupon surfaces were rinsed with ethanol and dried with a hot air stream. After each polishing step, the coupon surfaces were cleaned with soap, rinsed with ethanol and dried with a hot air stream. The cleaned coupons were also examined after each polishing step using an Olympus light optical microscope to confirm that all surface scratches were removed before proceeding to the next polishing step.

The polished Alloy 800HT coupon surface was etched using 3 drops of glycerol added to a hydrochloric acid: nitric acid: acetic acid mixture with a ratio of 1.5:1:1 for 30 s. The polished Alloy 33 coupon surface was etched using a hydrochloric acid: nitric acid mixture with a ratio of 6:1 for 200 s. Figure 3-2 shows an image of the alloy microstructure in a RD-TT planar surface obtained with a LV100-Nikon optical microscope. The average grain diameter was measured using "Image Processing and Analysis in Java" (ImageJ) software [64] in accordance with the ASTM E112-12 standard practice. The average grain diameter in Alloy 800HT and Alloy 33 (with 95% confidence intervals) was 94±6 μm and 58±5μm respectively. Both microstructures exhibited equiaxed grains.

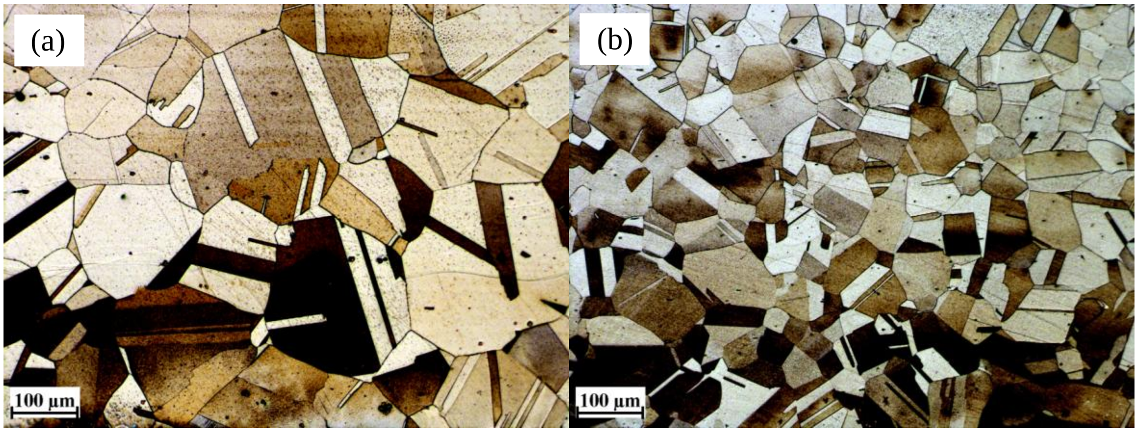

Figure 3-2 Light optical microscopy image of the etched RD-TT cross-section planar surface of: (a) Alloy 800HT and (b) Alloy 33.

3.2. SCW Corrosion Testing

Two sets of coupons (one set for each objected exposure temperature) were punched with numbers 1, 2, 3 and 4 and manually ground to an 800 grit surface finish using SiC abrasive papers and water as a lubricant, rinsed with ethanol and then dried with a hot air stream. With the knowledge that surface preparation has a distinct influence on corrosion in SCW [32] the 800 grit surface finish was set by the Canadian Gen IV team as a standard sample preparation outline to promote a meaningful comparison among the different laboratories performing the corrosion testing. Figure 3-3 shows a photograph of the coupons in the as-prepared condition prior to exposure in SCW.

Figure 3-3 Coupons of Alloy 800HT and Alloy 33 prior to exposure in SCW.

A static autoclave test facility (located at CanmetMATERIALS) made of Alloy 625 with a total chamber volume of 1045 ml was used for the exposure of the coupons. Two separate exposure temperatures, namely 550 °C and 625 °C, were considered.

3.2.1. Corrosion Testing at 25 MPa and 550 °C SCW

The first set of manually ground coupons (four of Alloy 800HT and four of Alloy 33) were suspended on a coupon tree made of Alloy 625 (shown in Figure 3-4). Along with the aforementioned alloys coupons of Type 316L stainless steel were also examined in the same testing autoclave. The coupons were then inserted into the autoclave and exposed to ASTM D1193-99 Type IV deionized water heated to 550±1 °C and pressurized to 25±2 MPa (density of 85.168 kg/m^3) for 500 h. Figure 3-4 shows the temperature and pressure profiles of the SCW test environment (as recorded and provided by CanmetMATERIALS). The initial dissolved oxygen (DO) content in the water was 8 ppm (air saturation at room temperature). No attempt was made to maintain this level during the 500 h exposure.

Figure 3-4 Picture of coupon tree loaded with coupons.

(a) Temperature Profile

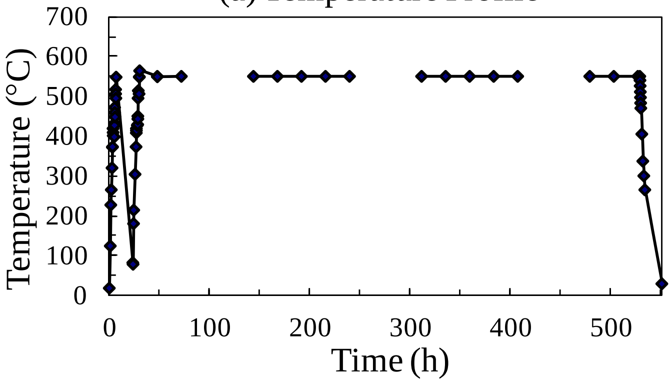

(b) Pressure Profile

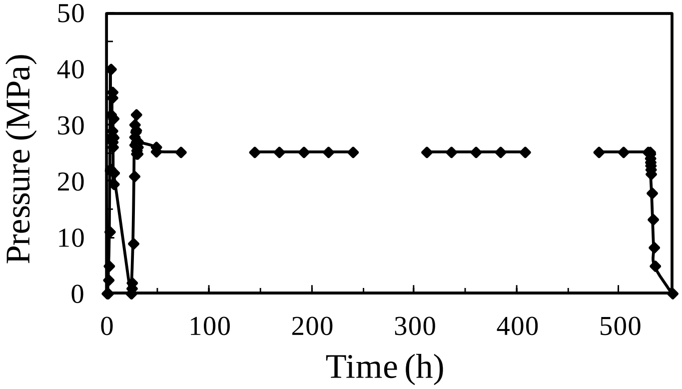

Figure 3-5(a) Temperature profile and (b) pressure profile of the SCW test environment during coupon exposure in the static autoclave.

3.2.2. Corrosion Testing at 25 MPa and 625 °C SCW

The second set of manually ground coupons (four of Alloy 800HT and four of Alloy 33) were suspended on the sample tree made of Alloy 625 and exposed to ASTM D1193-99 Type II deionized water in the static autoclave also made of Alloy 625 and heated to 625±2 °C and pressurized to 25±0.5 MPa for 500 h. Along with the abovementioned alloys, coupons of P91, AL6X+N, 310S, 316L, 304H alloys were also examined in the same testing autoclave. Figure 3-6 represents the temperature and pressure profiles of the SCW test environment (as recorded and provided by

CanmetMATERIALS). Consistent with the previous test, the initial DO content in the water was 8 ppm (air saturation at room temperature) and no attempt was made to maintain this level during the 500 h exposure.

(a) Temperature Profile

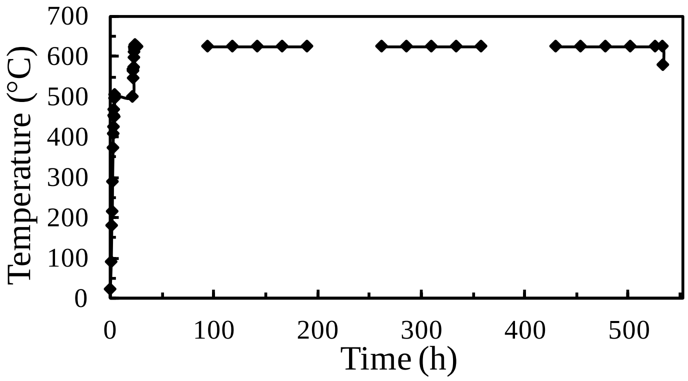

(b) Pressure Profile

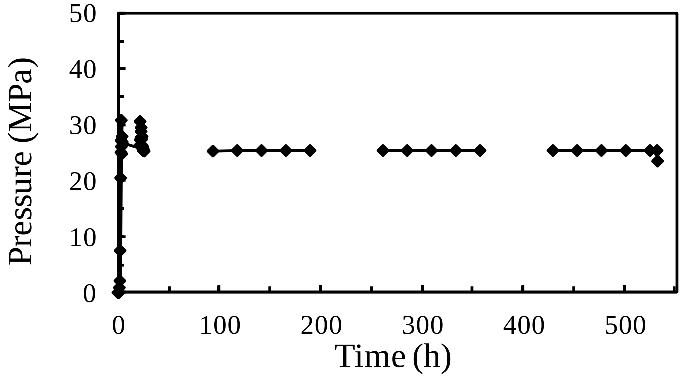

Figure 3-6(a) Temperature profile and (b) pressure profile of the SCW test environment during coupon exposure in the static autoclave.

3.3. Gravimetric Measurements

Each coupon was weighed before and after exposure using an analytical Mettler Toledo Balance at CanmetMATERIALS with the precision of 0.000001 g in order to determine the amount of weight gained (or lost) during the 500 h exposure. A weight loss measurement was also conducted after removing the oxide scale from one coupon of each set of four in order to confirm the comparative results of the weight gain. This measurement was performed with a balance with the precision of 0.0001 g at McMaster University. Only one coupon was selected in order to save the remaining three for the electron microscopy examination of the oxide scale formed. The oxide scale was removed using the following procedure [15]:

Solutions:

(a)	Citric Acid	2.0%
	Dibasic Ammonium Citrate	5.0%
	Disodium EDTA	0.5%
(b)	Potassium Permanganate	10.0%
	Caustic Soda	4.0%

1. Hang samples in a stirred solution of (a) for 60 minutes at 90 °C
2. Remove samples and sonicate in methanol for 15 minutes
3. Allow samples to dry and weigh
4. Hang samples in a stirred solution of (b) for 60 minutes at 90 °C
5. Remove samples and sonicate in methanol for 15 minutes
6. Allow samples to dry and weigh
7. Hang samples in a stirred solution of (a) for 30 minutes at 90 °C
8. Remove samples and sonicate in methanol for 15 minutes
9. Allow samples to dry and weigh
10. Repeat steps 7-9 in cycles until weight loss stabilizes

An unexposed coupon of each alloy was also included in the above descaling procedure to act as the control. The effectiveness of this procedure has been demonstrated elsewhere [15].

3.4. Electron Microscopy Examination

Scanning Electron Microscopy (SEM) was initially used for a plan view examination of the nature and morphology of the oxide scales formed on both alloys. A schematic of the SEM sample preparation is depicted in Figure 3-7. First, the corroded coupons were cleaned and degreased using acetone and dried with a N_2 stream. One coupon of Alloy 800HT and one coupon of Alloy 33 for each temperature experiment were then mounted in plan-view on aluminum (Al) SEM pin-type stubs. This was done using an adhesive air drying silver (Ag) paste which forms a conductive film between the coupons and SEM stubs. The coupons attached to the stubs were inserted in an oven at 50 °C for 30 minutes to dry the Ag paint. Coupons attached to the stubs were then slowly passed through a Demagnetizer Bergeon 2321 unit which removes the built-up magnetic field by randomizing the magnetized domain in the sample. This method is particularly useful for better imaging of steels and samples containing Fe_3O_4 which can exhibit a magnetic field in the SEM vacuum chamber and thus affect the imaging quality.

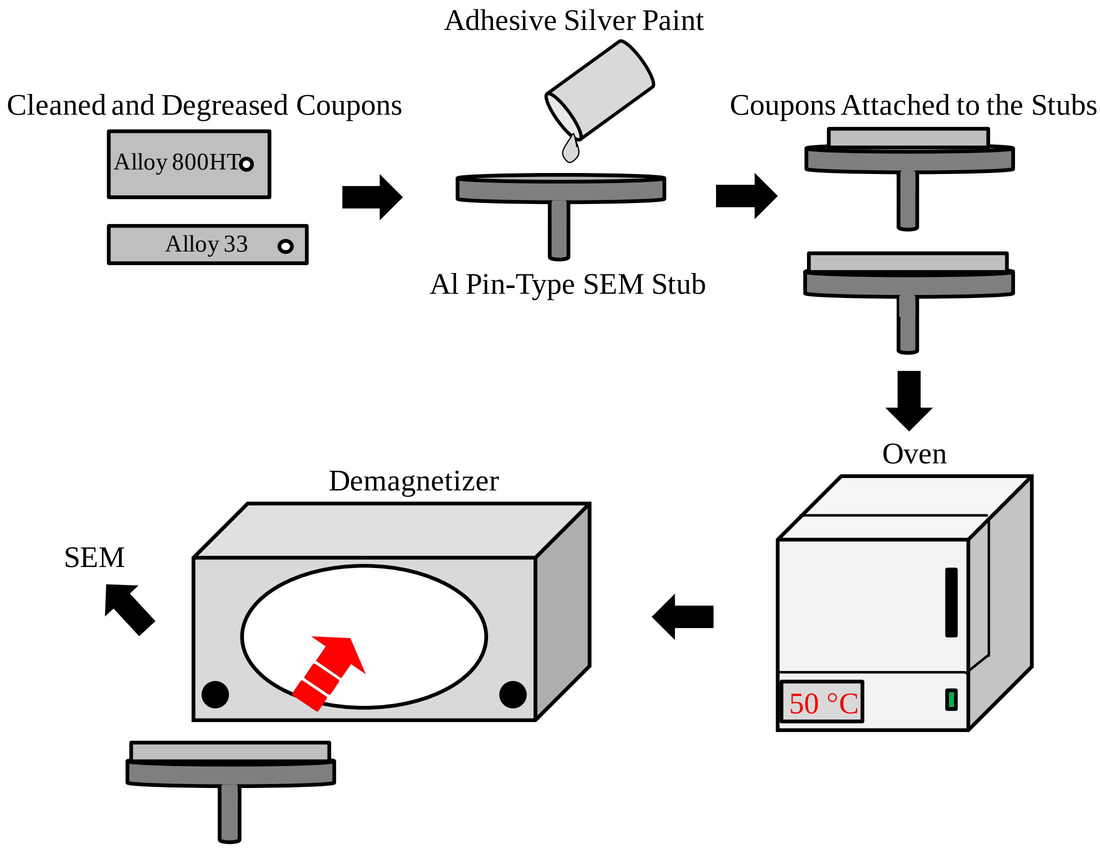

Figure 3-7 Schematic of SEM/FIB sample preparation procedure.

The SEM characterization was done using a Zeiss NVision 40 focused ion beam (FIB/SEM) microscope equipped with a Schottky Field Emission Gun (FEG) filament, a silicon drift detector (SDD) and an integrated Oxford Synergy system with INCA energy dispersive spectroscopy (EDS) X-ray micro-analysis. The coupons were tilted to 54° during imaging. An accelerating voltage of 5 kV and a working distance of 10 mm was used for topographic images. An accelerating voltage of 10 kV with a working distance of 10 mm was then used for the SEM/EDS analysis.

Site-specific thin cross-section foils of the oxide scale/alloy interfaces were prepared from a corroded Alloy 800HT and Alloy 33 coupon surface using FIB with a gallium (Ga) ion beam voltage of 30 kV, a beam current of 80 pA and a working distance of 5.6-5.9 mm. A tungsten (W) strap (2 μm thick) was first deposited on the oxide scale to protect it during ion milling. Ion-induced Secondary Electron (ISE) images of the milled-cross section foils were acquired to obtain better grain contrast in the alloys. This was done with a 30 kV Ga ion beam, a current beam of 80 pA and a working distance of 5.8-6.0 mm. Subsequent examination was conducted using a JEOL 2010F STEM/TEM field emission Transmission Electron Microscope (TEM), equipped with an Oxford INCA EDS system and an operating voltage of 200 kV. The STEM/EDS technique was used to acquire both elemental line scan/depth profiles and elemental phase maps. The acquisition time for each point analysis was 60 s in the STEM/EDS analysis.

To characterize the nature of the large crystalline regions in the coupons, SAD patterns were obtained from different areas larger than 500 nm across the oxide scale/alloy interface. To do so, the smallest SAD aperture with 10 μm diameter (an effective 150 nm diameter on the image) was used. The acquisition time for obtaining the SAD patterns was 30 s. Reference data of the expected oxide compounds as part of the scale formed on the surface of both alloys [65] were used to simulate their SAD patterns using the software package JEMS [66]. The acquired SAD patterns were then superimposed to those of the reference compounds for a better comparison.

An EELS analysis with a dispersion of 0.2 eV/pixel was also conducted on different regions across the oxide scale/alloy interface in dark-field (DF) STEM mode. Table 3-3 shows the energy windows (ranges) for the major alloying elements that were expected to have formed oxides in Alloy 800HT and Alloy 33 [67]. The principle edges are highlighted in grey for all the elements.

Table 3-3 Major and minor energy-loss edges for the expected major oxide forming alloying elements present in Alloy 800HT and Alloy 33

Element	**Major Edges (eV)**				**Minor Edges (eV)**	
	K_1	$M_{2,3}$	L_3	L_2	M_1	L_1
Fe	-	54	708	721	93	846
Cr	-	42	575	584	74	695
Ni	-	68	855	872	112	1008
Mn	-	49	640	651	84	769
Ti	4966	35	456	462	60	564
Si	1839	-	99	99	-	149
Al	1560	-	73	73	-	118
O	532	-	-	-	-	-

The O-K edge typically shows more variation in each oxide type: thus, making the analysis more straight forward. Therefore, all the EELS analyses in the current work were mainly focused on the O-K edges. However, the Cr-$L_{2,3}$, Mn $L_{2,3}$ and Fe-$L_{2,3}$ energy windows were also chosen in order to track the existence of trace elements in the oxides. The Ni-$L_{2,3}$ energy window was excluded from the EELS spectra because the larger range of energy loss required for analysis was expected to produce very small changes in the intensity peaks that would no longer be visible. Nonetheless, this did not affect the attempt to characterize the oxide chemistry since the Ni oxides could be detected using the O-K edge EELS spectra. The acquired EELS spectra were analyzed using the Digital Micrograph software [67] and were compared with the reference spectra of expected oxide compounds to delineate the composition of the oxide scale.

Auger electron spectroscopy (AES) was performed with a JEOL JAMP-9500F AUGER/FE-SEM on the corroded surface of both alloys in plan-view to corroborate the results obtained by STEM/TEM. AES can provide a chemical state analysis within a 10 nm analysis depth in the sample. This can assure that the substrate will not have any effect on the characterization of the very thin oxide scale. The analysis consisted of acquiring a sputter depth profile from three distinct areas of the corroded surface. Prior to the AES analysis, the corroded coupons (one per exposure condition) were cleaned to remove the residual contamination by sputtering with an argon (Ar) ion beam with a 3 kV accelerating voltage for 30 s. A 3 kV Ar ion beam with a 30° tilting angle and a working distance of 20-23 mm was then used to sputter the surface layers away in successive steps. A 3kV electron beam was then used to interact with the sample to obtain the AES depth profiles with the same microscope settings mentioned above. Standard deconvoluted curves were used for each expected oxide compounds to best fit the element peaks. Atomic percent depth profiles of the alloying elements as a function of the sputtering time were then constructed from the intensity profile spectra using the JEOL microscope software.

4. Results

4.1. Corrosion Testing at 25 MPa and 550 °C SCW

4.1.1. Alloy 800HT

Figure 4-1 shows the photograph of the corroded Alloy 800HT coupons after exposure in SCW at 550 °C for 500 h. Surface of the coupons had spotted matte surface with "rainbow" appearance in dark colors. Macroscopic cracks or blisters were not observed on any of the coupon surfaces.

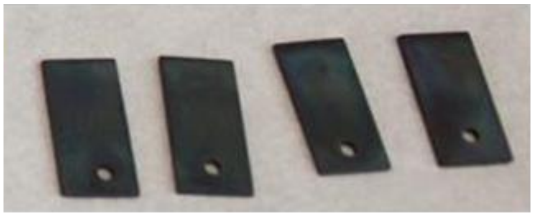

Figure 4-1 Image showing the appearance of the exposed Alloy 800HT coupons after exposure in 25 MPa SCW at 550 °C for 500 h.

Table 4-1 shows the average (avg.) coupons weight gain (WG) after exposure in SCW. The avg. WG for the corroded Alloy 800HT coupons using the 95% Confidence Intervals (CI) was ~ 7.9 ± 1.8 (mg/dm^2). Note that values in Table 4-1 were rounded to the nearest 4 decimal places.

Table 4-1 WG measurement data on the four corroded Alloy 800HT coupons exposed in SCW at 550 °C for 500h

Coupon #	WG (mg/dm^2)	Avg. WG (mg/dm^2)	WG by 95% CI (mg/dm^2)
(1)	7.0643	7.8876	7.8876 ± 1.7578
(2)	9.3353		
(3)	6.9865		
(4)	8.1642		

The descaling process to measure the WL in the corroded coupons was performed only on one coupon (coupon number 3 with ~ 7.0 mg/dm^2 WG) in order to keep the rest of the coupons for electron microscopy characterization. Table 4-2 shows the WL value was ~ 22.9 mg/dm^2. A reference coupon of Alloy 800HT was also exposed in the same descaling run to make sure the subsurface was not removed by the descaling solution during the procedure.

Table 4-2 WL measurement data on the corroded Alloy 800HT coupon (coupon number 3 with ~ 7.0 mg/dm^2 WG) exposed in SCW at 550 °C for 500h

Coupon Type	**WL (mg/dm^2)**
Corroded	22.9065 ~ 22.9
Reference	0.0003

Figure 4-2(a) and (b) presents typical low and high magnification SEM plan view images of Alloy 800HT coupon surface after exposure (coupon with ~ 9.3 mg/dm^2 WG). The surface consisted of oxide "islands" residing on top of a "clean" oxide scale.

The oxide islands were typically larger than 2 μm and had a cubic/octahedral morphology. An SEM/EDS analysis showed these islands were enriched in O and Fe. The clean oxide scale consisted of a granular structured grains also with cubic/octahedral morphology. The SEM/EDS analysis of the clean oxide scale was considered non trustworthy since the electron interaction volume was expected to be much larger than the scale thickness. The clean oxide surface was also decorated with a random distribution of fine spherical particles. An SEM/EDS analysis revealed that these particles were enriched in silver (Ag). These Ag particles were most likely an artifact from the static autoclave exposure since an Ag plated gasket was used to seal the autoclave lid. Thus, these Ag particles were not expected to have had any influence whatsoever on the formation of the protective oxide scale. Figure 4-2(c) shows the site-specific location that was chosen to prepare the thin film cross-section via FIB milling for subsequent examination by TEM. The site was selected to contain a portion of both the oxide islands and the clean oxide scale. Figure 4-2(d) shows an ISE image of the final thin foil attached to a TEM copper (Cu) grid. A distinct feature is the localized corroded area (oxide “crater”) that formed internally directly underneath the oxide island. Interestingly, the oxide crater appeared to have formed in between a set of twin boundaries in the alloy. Moreover, recrystallized grains were observed in the alloy at the clean oxide scale/alloy interface. This is most likely a consequence of the plastic deformation accumulated in this region during sample preparation (mechanical abrasion). An additional FIB-milled trench excavated through two other oxide islands present on the surface far from the one depicted in Figure 4-2(d) revealed that the observations noted above are indeed typical [Figure 4-2(e) and Figure 4-2(f)].

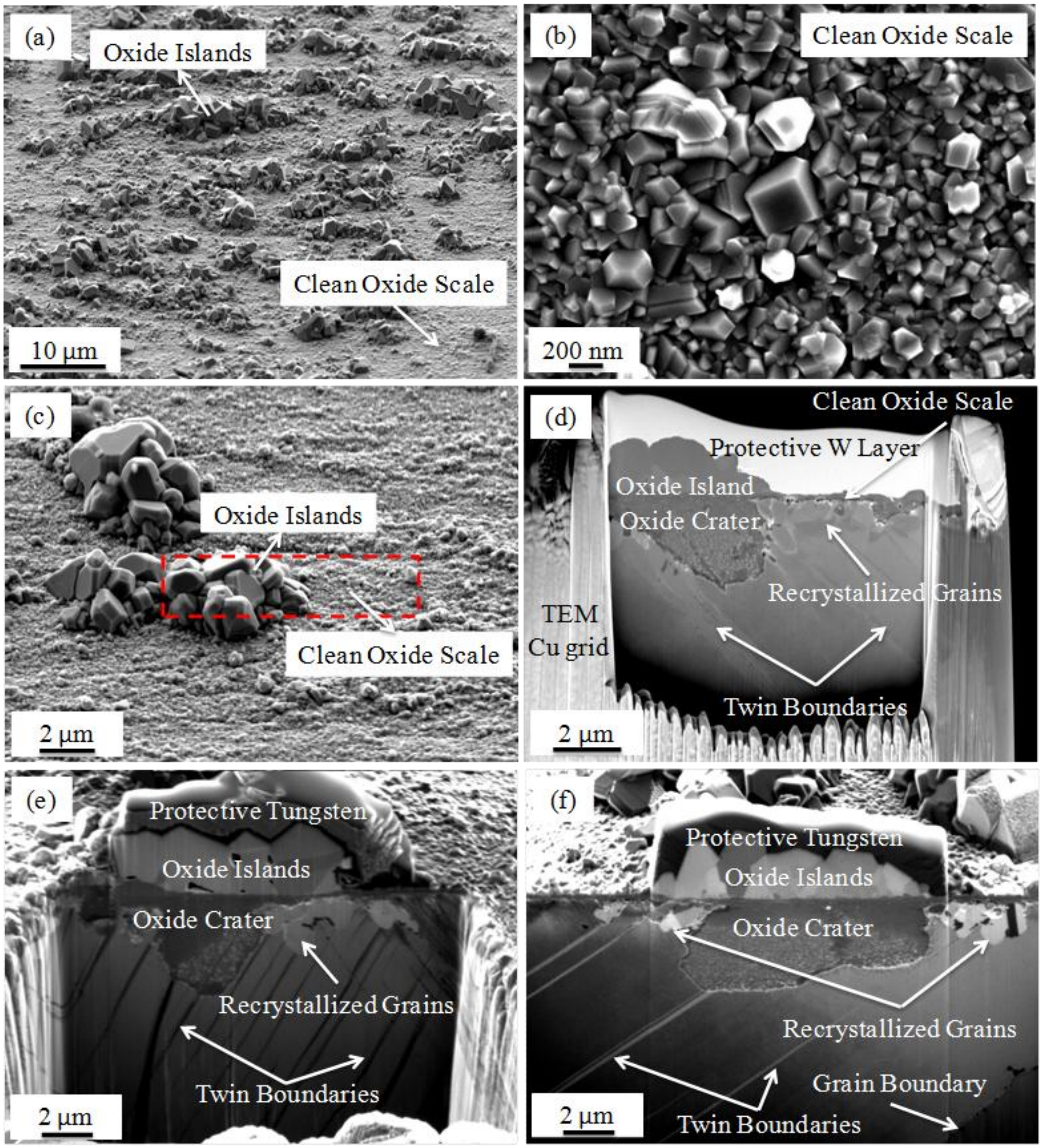

Figure 4-2(a) Low magnification and (b) high magnification plan view SEM images of the corroded Alloy 800HT surface, (c) plan view SEM image showing an area of interest, framed with a dashed rectangle, on the corroded Alloy 800HT surface for TEM sample preparation, (d) cross-section ISE image of the final TEM oxide-scale/alloy thin foil attached to a TEM Cu grid, (e) and (f) images of the FIB-milled trenches excavated through two other oxide islands.

Figure 4-3(a) shows a low magnification BF-STEM image of the corroded Alloy 800HT coupon in cross section. The protective W layer deposited on the oxide scale is shown in W STEM/EDS elemental map in Figure 4-3(b). Figure 4-3(c)-(j) illustrates the associated STEM/EDS maps of elements present in the coupon that were believed to form a possible oxide that could affect the alloy corrosion resistance. Oxide islands formed on the clean oxide scale were enriched in Fe and O. Oxide crater was enriched in O, Cr, Fe and Mn. Also Ni was observed in the oxide crater but closer to the substrate. Cr, Fe and Mn were found in the clean oxide scale. Ni was mostly enriched at the alloy/oxide interface. Ti and small amount of Si and Al were found to be present below the oxide scale and oxide crater along with O.

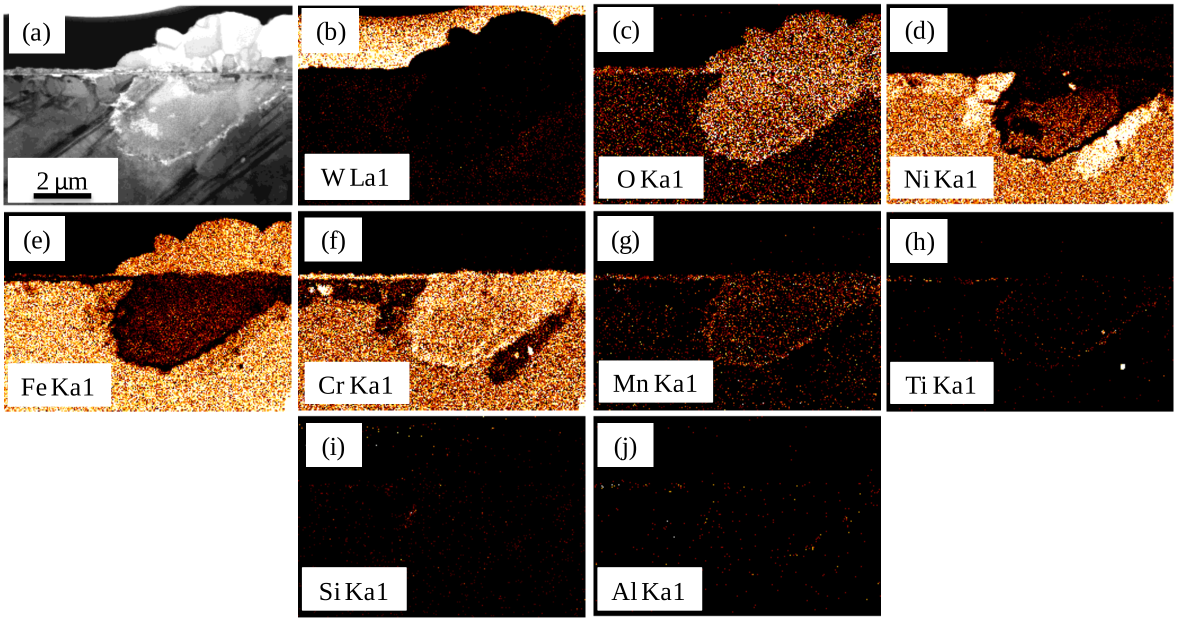

Figure 4-3(a) Low magnification BF-STEM image and (b)-(j) STEM/EDS elemental maps for W, O, Ni, Fe, Cr, Mn, Ti, Si and Al in the corroded Alloy 800HT.

Figure 4-4 shows the BF-STEM image along with the results of the SAD and EELS analysis of selected area 1 (oxide island) and 2 (oxide crater). The oxide islands were best characterized as being comprised of Fe_3O_4. The SAD pattern [Figure 4-4(b)] matched well with the reference diffraction pattern obtained from the JEMS software. The EELS O-K and Fe-$L_{2,3}$ edges [Figure 4-4(c)] also matched well with the the reference spectra. The oxide crater was best characterized as being composed of $FeCr_2O_4$. The SAD pattern

[Figure 4-4(e)] matched well with the reference diffraction pattern obtained from the JEMS software. The EELS spectra particulary in O-K edge [Figure 4-4(g)] showed the characteristic feature of $FeCr_2O_4$: small intensity shoulder peak close to 540 eV. The formation of $NiCr_2O_4$ in the oxide crater was also possible in the areas adjacent to the oxide crater/alloy interface due to subsitution of Fe ions by Ni ions. Furthermore, the Mn small intensity peak observed in the EELS spectrum [Figure 4-4(f)] implied the possbile formation of $[Fe,Cr,Mn]_3O_4$. STEM/EDS analysis in the oxide crater confirmed the presence of low concentration of Mn (up to 1.5 wt.%) in this area.

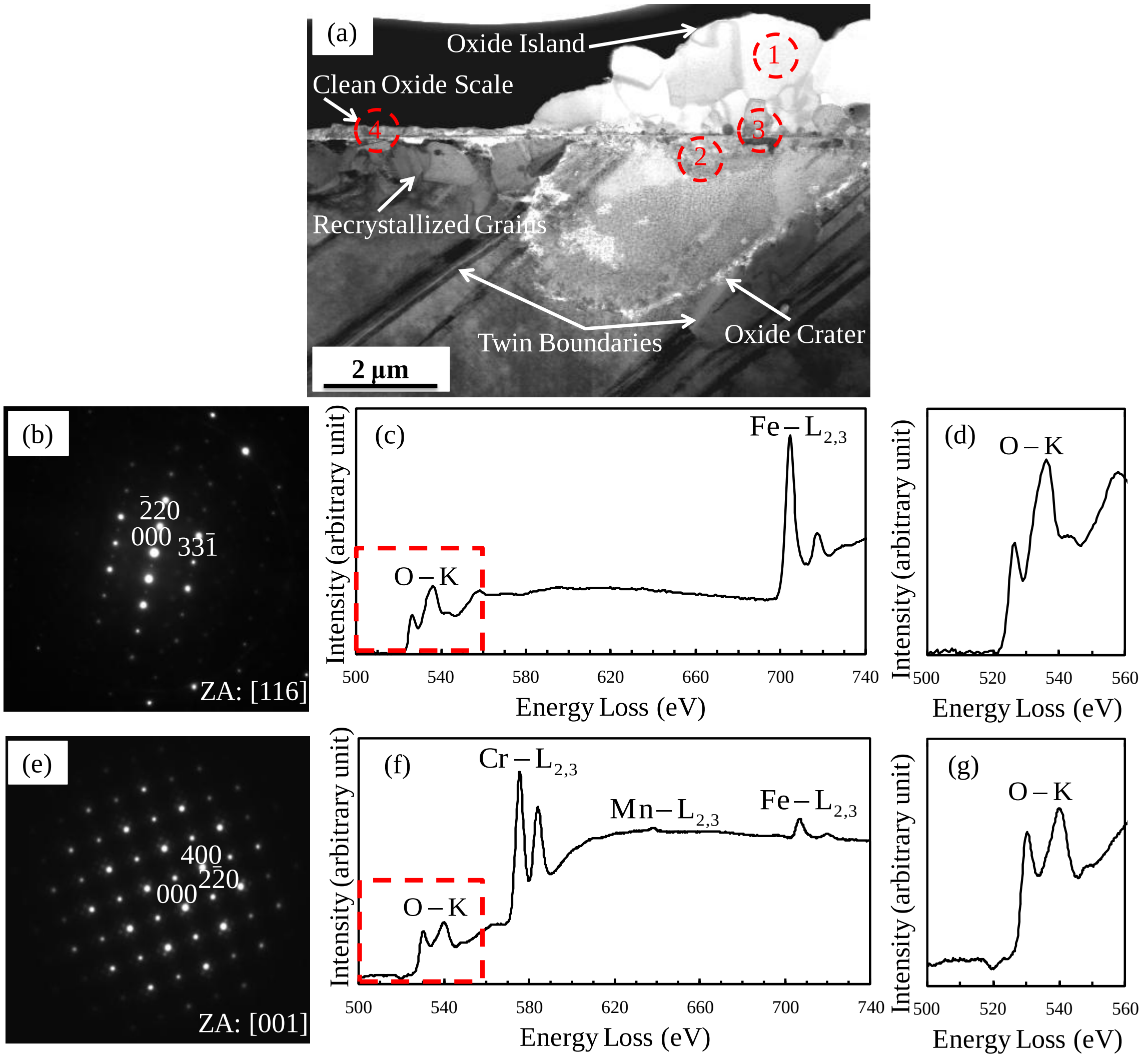

Figure 4-4(a) BF-STEM cross-section image of corroded Alloy 800HT, (b) SAD pattern of area 1 (Fe_3O_4), (c) and (d) EELS spectra of Fe_3O_4 (e) SAD pattern of area 2 ($FeCr_2O_4$), (f) and (g) EELS spectra of $FeCr_2O_4$.

Figure 4-5(a) shows a high magnification BF-STEM image of area 3 in Figure 4-4(a). A fine-grained oxide layer was observed to exist in between the oxide crater and the oxide island. An EELS analysis [Figure 4-5(b) and Figure 4-5(c)] of this intermediate layer indicated that it was comprised of $[Cr,Fe]_2O_3$.

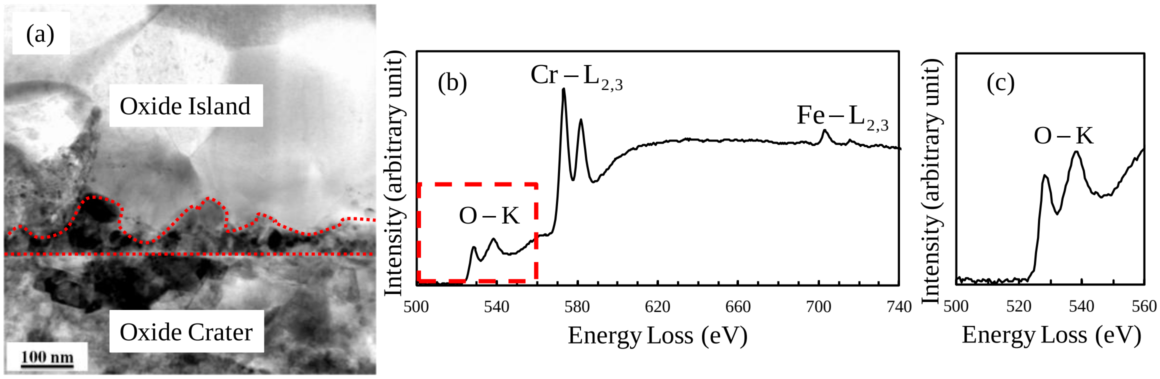

Figure 4-5(a) High magnification BF-STEM image of the oxide island/oxide crater interface of Alloy 800HT, (b) EELS spectra of the assigned area shown in part (a), and (c) the corresponding O-K edge EELS spectra of the dashed rectangular area shown in part (b).

Figure 4-6(a) shows a BF-STEM image of the clean oxide scale [area 4 in Figure 4-4(a)]. The associated set of STEM/EDS elemental maps from all the major elements that were expected to form an oxide is shown in Figure 4-6(b)-(j). The elemental maps indicated the formation of a multi-layer oxide consisting of an outer Fe-rich layer residing on top of a Cr-rich intermediate layer and a very thin oxide inner layer containing Ti and Si. The thickness of the Ti-Si-O layer was 15±3 nm measured by ImageJ software [64]. Ni was found to be present along with Fe in the outer layer, whereas Mn was found to be present with Cr in the intermediate layer. The maps also indicated that a zone (851±19 nm deep) depleted in Cr and Mn and enriched in Ni was formed in the alloy.

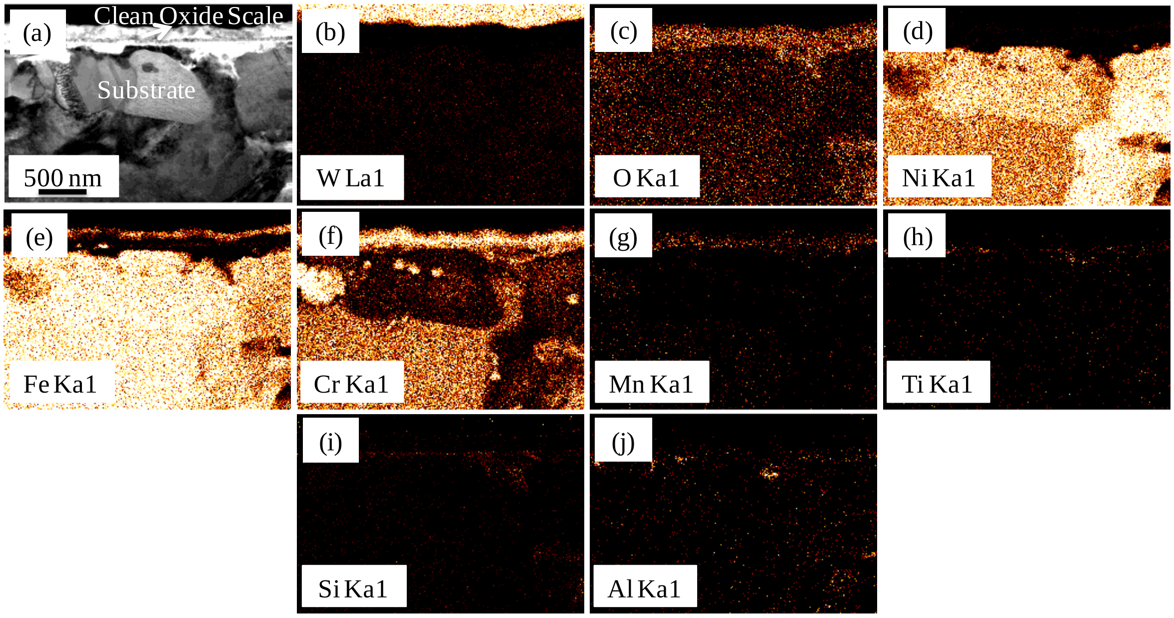

Figure 4-6 BF-STEM image and STEM/EDS elemental maps of the clean oxide scale/alloy interface for W, O, Ni, Fe, Cr, Mn, Ti, Si and Al in Alloy 800HT.

An EELS analysis was performed on a line scan across the clean oxide scale/alloy interface; area 4 in Figure 4-4(a). The spectrum for three areas corresponding to observed changes in composition were examined. The core-loss $L_{2,3}$ EELS edges for Ni are 872 eV and 855 eV respectively. However, Ni was excluded from the spectrum in order to obtain the fine edge structure EELS spectra (e.g. small intensity characteristic peaks) from the oxide scale. The three spectra shown in Figure 4-7 reveal that Fe, Cr and O were present in area 2 and area 3. Mn showed a small yet noticeable intensity peak in area 1. Figure 4-7(c) shows the magnified O-K edges in EELS spectra for each area. Using the O-K edge peaks in Figure 2-11 as the reference, area 3 was best characterized to be comprised of $[Fe,Cr]_3O_4$, whereas areas 1 and 2 were best characterized to be comprised of $[Cr,Fe]_2O_3$.

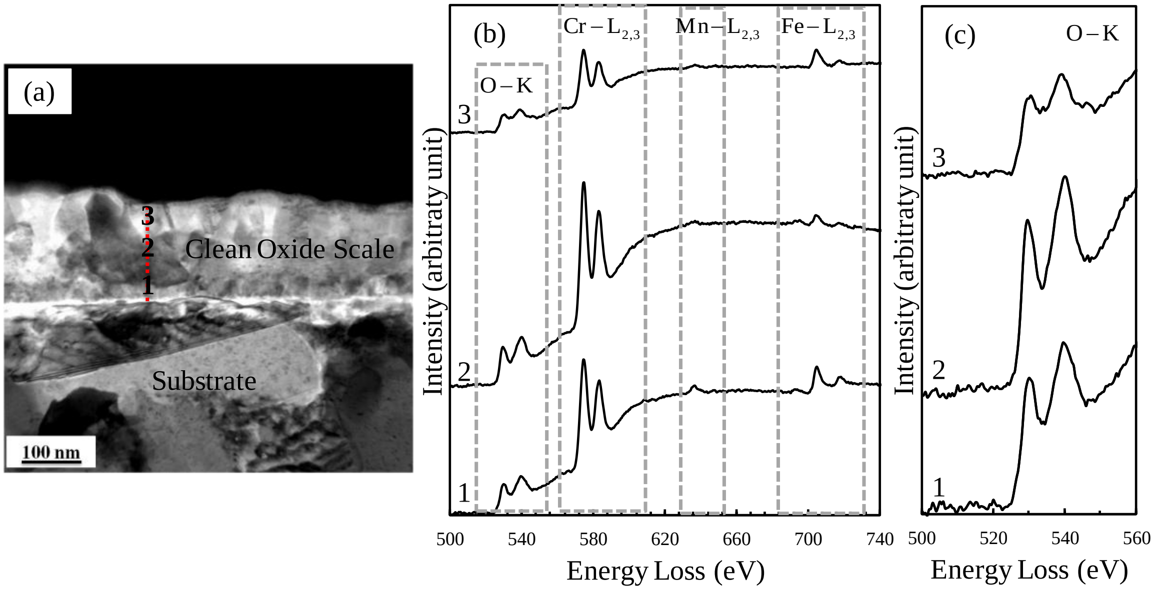

Figure 4-7(a) High magnification BF-STEM image of the clean oxide scale/alloy interface of Alloy 800HT, (b) EELS spectra of areas 1, 2 and 3, and (c) the corresponding O-K edge EELS spectra for areas 1, 2 and 3.

The results of the elemental depth profiles acquired by AES through the “clean” oxide scale formed on Alloy 800HT are shown in Figure 4-8. This test was repeated three times for confidence in reporting the results. The oxide scales were found to be enriched in Fe, Cr and O and small Ni content on top and Cr and O near the alloy/oxide interface consisted to be $[Fe,Cr]_3O_4$ and $[Cr,Fe]_2O_3$ respectively. It should be noted that the total thickness of the oxide scale and Cr depleted zone in Alloy 800 HT was larger than 1 μm which made it not possible to measure the Cr depleted zone in the same acquisition time. For this reason, STEM/EDS line scan through the oxide scales and substrate were used and results will be shown later on in the discussion section.

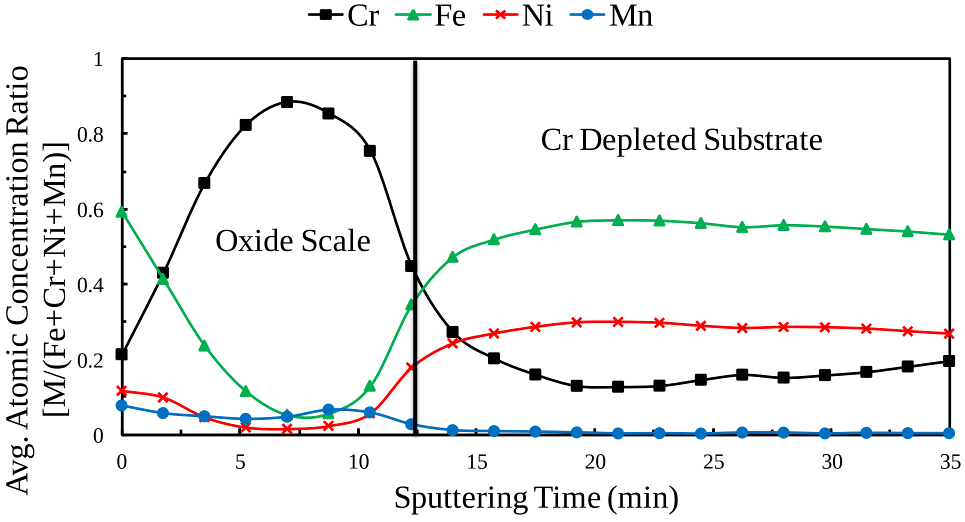

Figure 4-8 Avg. atomic concentration ratio depth profile for Cr, Fe, Ni and Mn obtained by AES in Alloy 800HT exposed in SCW at 550 °C for 500 h.

4.1.2. Alloy 33

Figure 4-9 shows the photograph of the corroded Alloy 33 coupons after exposure in SCW at 550 °C for 500 h. Surface of the coupons had a shiny, multi-colored "rainbow" appearance in bright hues. No macroscopic cracks or blisters were observed on any of the coupon surfaces.

Figure 4-9 Image showing the appearance of the exposed Alloy 33 coupons after exposure in 25 MPa SCW at 550 °C for 500 h.

Table 4-3 shows the avg. coupons WG after exposure in SCW. The avg. WG for the corroded Alloy 33 coupons using the 95% Confidence Intervals (CI) was ~ 6.5 ± 0.3 (mg/dm^2). Note that values in Table 4-3 were rounded to the nearest 4 decimal places.

Table 4-3 WG measurement data on the four corroded Alloy 33 coupons exposed in SCW at 550 °C for 500h

Coupon #	WG (mg/dm^2)	Avg. WG (mg/dm^2)	WG by 95% CI (mg/dm^2)
(1)	6.2077	6.4503	6.4503 ± 0.3103
(2)	6.3827		
(3)	6.6410		
(4)	6.5701		

The descaling process to measure the WL was performed only on coupon number 2 with ~ 6.4 mg/dm^2 WG. Table 4-4 shows the WL value was ~ 12.9 mg/dm^2. A reference coupon of Alloy 33 was also exposed in the same descaling run to make sure the subsurface was not removed by the descaling solution during the procedure..

Table 4-4 WL measurement data on the corroded Alloy 33 coupon (coupon number 2 with ~ 6.4 mg/dm^2 WG) exposed in SCW at 550 °C for 500h

Coupon Type	WL (mg/dm^2)
Corroded	12.9204 ~ 12.9
Reference	0.0001

Figure 4-10(a) presents a high magnification SEM plan view image of the Alloy 33 surface after exposure (with 6.6 mg/dm^2 WG). The surface consisted mostly of a granular clean oxide scale. Particles rich in Ag were observed scattered on the clean oxide scale (similar to that observed on the corroded Alloy 800HT surface). In addition, some scattered Ce-rich nodules were detected on the corroded surface [Figure 4-10(b)]. The Ag-rich particles were considered an experimental artifact, but the Ce-rich nodules are believed to have formed during exposure, since Ce is intentionally added as to Alloy 33 as a minor alloying element for unspecified metallurgical reasons. Figure 4-10(b) shows the site-specific location that was chosen to prepare the thin film cross-section via FIB milling for subsequent examination by TEM. The site was selected to contain a portion of both a Ce-rich nodule and the clean oxide scale. Figure 4-10(c) shows an ISE image of the final TEM oxide-scale/alloy thin foil attached to a TEM Cu grid.

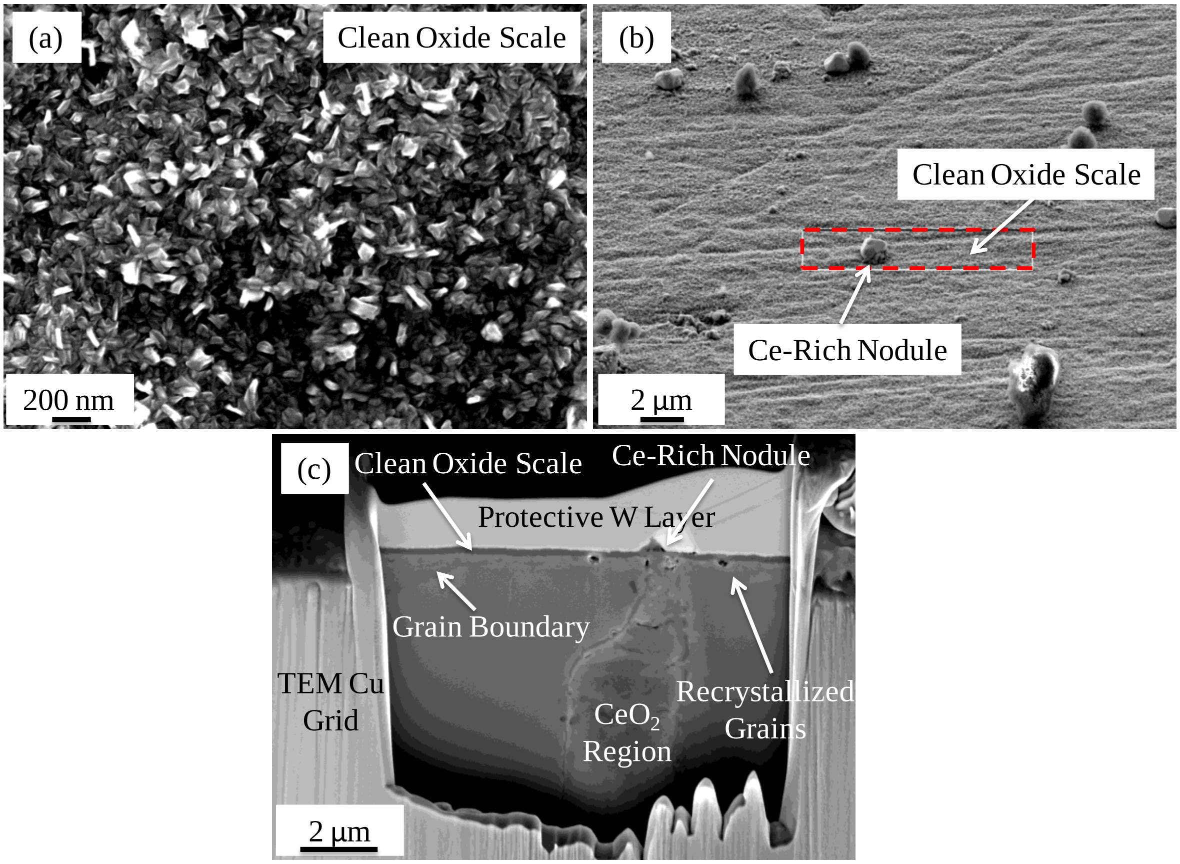

Figure 4-10(a) Plan view high magnification SEM image of the corroded Alloy 33 surface (b) plan view SEM image showing an area of interest, framed with a dashed rectangle, on the corroded Alloy 33 surface for TEM sample preparation and (c) cross-section ISE image of the final TEM oxide-scale/alloy thin foil attached to a TEM Cu grid.

A low magnification BF-STEM image and a set of STEM/EDS elemental maps are shown in Figure 4-11(a)-(j). The clean oxide scale was only consisted of Cr and O. The particle on top of the corroded alloy was verified to be rich in Mn, Ce and O. Also, the region below the particle was confirmed to be enriched in Ce and O most likely a CeO_2 region.

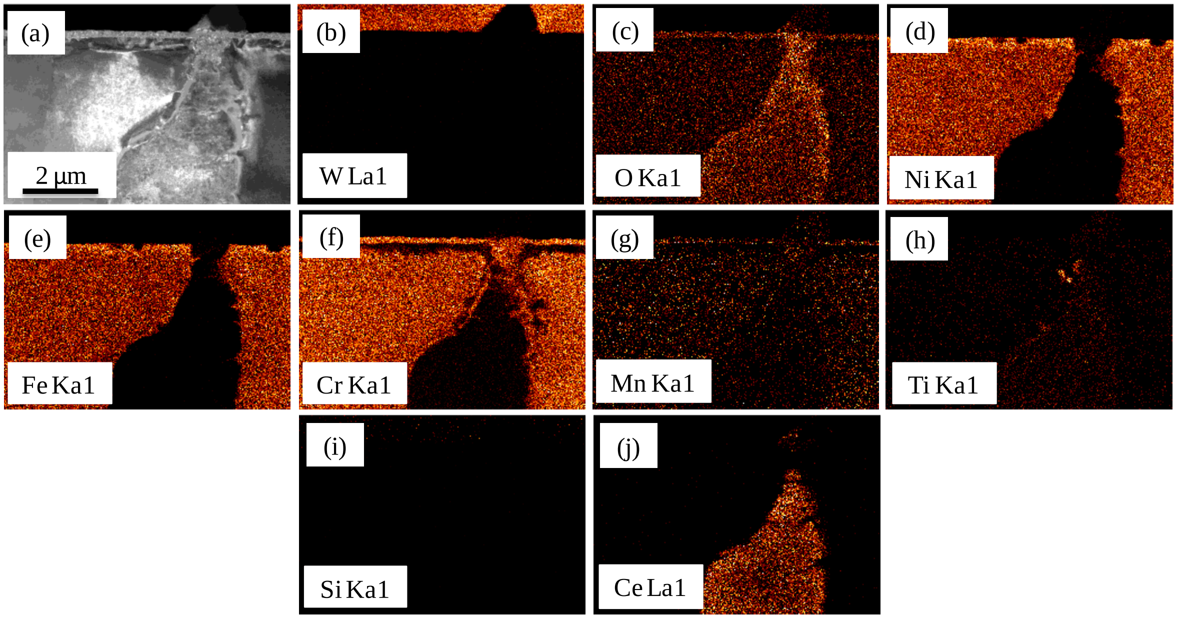

Figure 4-11(a) Low magnification BF-STEM image and (b)-(j) STEM/EDS elemental maps for W, O, Ni, Fe, Cr, Mn, Ti, Si and Ce in the corroded Alloy 33.

Figure 4-12 shows a set of STEM/EDS elemental maps of the clean oxide scale/alloy interface with all the major alloying elements that can form oxide in this alloy. The maps indicate that an oxide layer enriched with Cr had formed on top of a very thin oxide layer enriched in Si. Thickness of the Si rich layer was 13±2 nm measured by ImageJ software [64]. Mn was found to be present along with Cr in the outer layer. The maps also indicate that a zone with significant Cr and Mn depletion and Fe and Ni enrichment had formed in the alloy adjacent to the oxide scale interface. The depth of this zone was 242±24 nm.

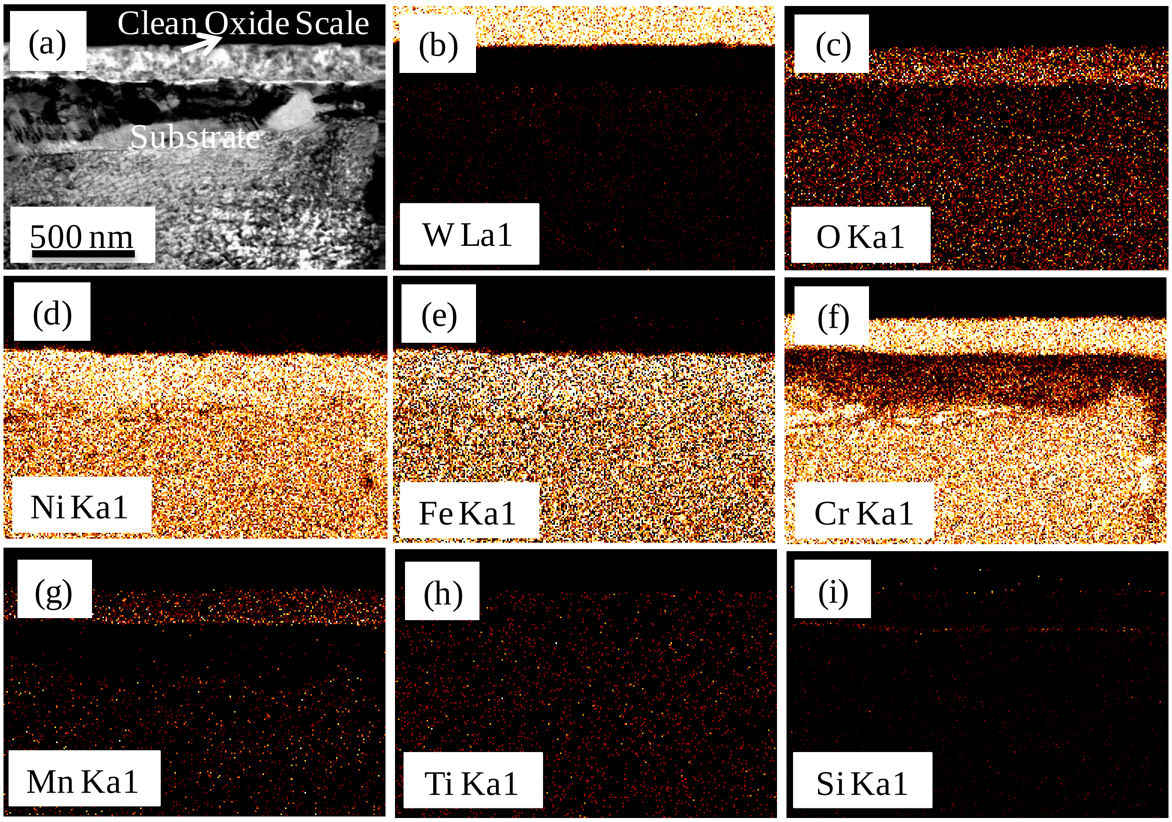

Figure 4-12 BF-STEM image and STEM/EDS W, O, Ni, Fe, Cr, Mn, Ti and Si elemental maps of the clean oxide scale/alloy interface of Alloy 33.

An EELS analysis was performed on a line scan across the clean oxide scale/alloy interface and the results (spectra) were examined in detail for three different areas. Figure 4-13 presents the set of three spectra. No Fe peak was observed in any of the three spectra whereas small intensity Mn peaks were detected mainly in area 1 and area 2. Figure 4-13(c) shows the magnified O-K edges in EELS spectra for each area. Again using the O-K edge peaks shown in Figure 2-11 as a reference, the Cr-rich oxide layer was best characterized as being comprised of Cr_2O_3.

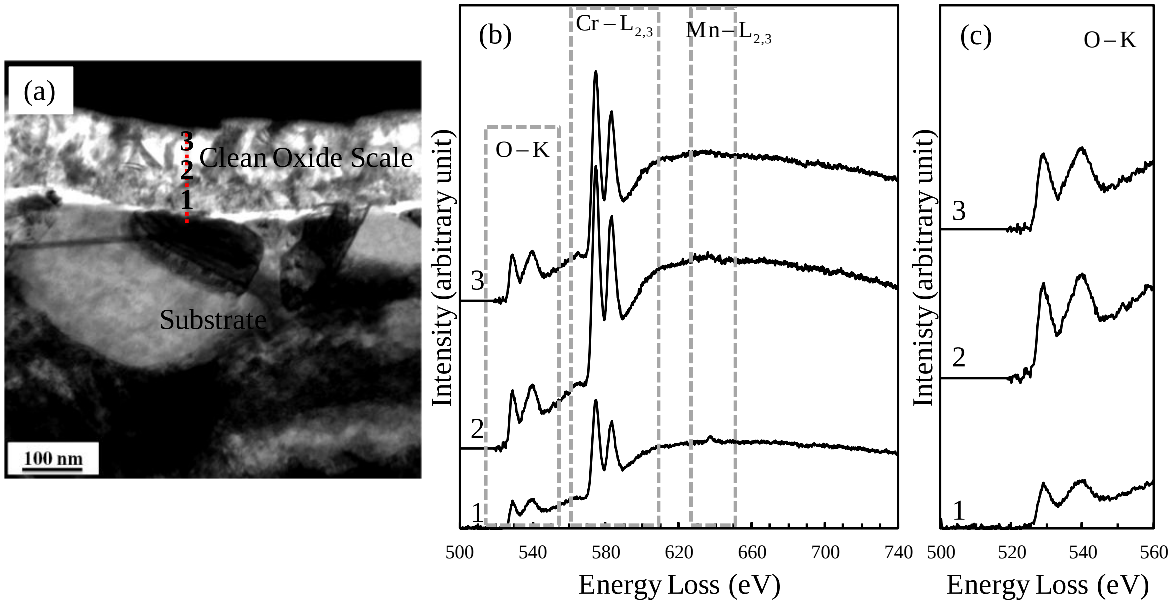

Figure 4-13(a) High magnification BF-STEM image of the clean oxide scale formed on Alloy 33, (b) EELS spectra of areas 1, 2 and 3 all representing Cr_2O_3 and (c) the corresponding O-K edge EELS spectra.

Average atomic concentration ratio for Cr, Fe, Ni and Mn AES depth profiles obtained from three different clean oxide scale area formed on Alloy 33 is shown in Figure 4-14. The oxide scale was consisted of a Cr-rich layer. Very small concentration of Fe, Ni and Mn were observed at the oxide surface but not enough to form a spinel scale. Mn was however, mostly enriched at the oxide/alloy interface. Furthermore, the Cr depleted zone in the substrate was small enough that could be detected in the AES depth profile and was smaller than that for Alloy 800HT.

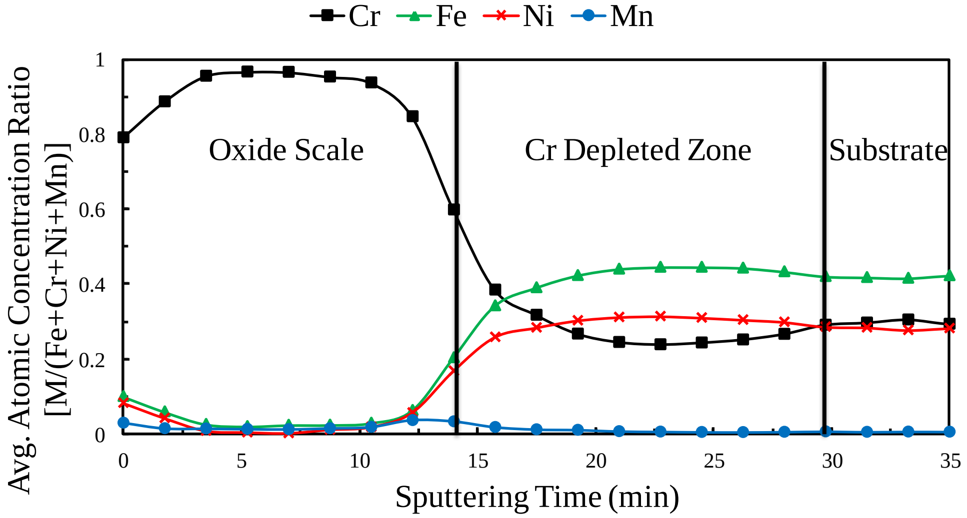

Figure 4-14 Avg. atomic concentration ratio depth profile for Cr, Fe, Ni and Mn obtained by AES in Alloy 33 exposed in SCW at 550 °C for 500 h.

4.2. Corrosion Testing at 25 MPa and 625 °C SCW

4.2.1. Alloy 800HT

Figure 4-15 shows the photograph of the corroded Alloy 800HT coupons after exposure in SCW at 625 °C for 500 h. Surface of the coupons same as when they were exposed in 550 °C SCW had spotted matte surface with "rainbow" appearance in dark colors. Also, macroscopic cracks or blisters were not observed on any of the coupon surfaces.

Figure 4-15 Image showing the appearance of the exposed Alloy 800HT coupons after exposure in 25 MPa SCW at 625 °C for 500 h.

Table 4-5 shows the avg. coupons WG after exposure in SCW. The avg. WG for the corroded Alloy 800HT coupons using the 95% Confidence Intervals (CI) was ~ 3.3 ± 2.1 (mg/dm^2). Note that values in Table 4-5 were rounded to the nearest 4 decimal places.

Table 4-5 WG measurement data on the four corroded Alloy 800HT coupons exposed in SCW at 625 °C for 500h

Coupon #	WG (mg/dm^2)	Avg. WG (mg/dm^2)	WG by 95% CI (mg/dm^2)
(1)	3.5687	3.3298	3.3298 ± 2.0569
(2)	3.8179		
(3)	1.4738		
(4)	4.4587		

The descaling process to measure the WL was performed only on coupon number 2 with ~ 3.8 mg/dm^2 WG. Table 4-4 shows the WL value was ~ 13.7 mg/dm^2. A reference coupon of Alloy 800HT was also exposed in the same descaling run to make sure the subsurface was not removed by the descaling solution during the procedure..

Table 4-6 WL measurement data on the corroded Alloy 800HT coupon (coupon number 2 with ~ 3.8 mg/dm^2 WG) exposed in SCW at 625 °C for 500h

Coupon Type	WL (mg/dm^2)
Corroded	13.7482 ~ 13.7
Reference	0.0002

Low and high magnification SEM plan view images of a corroded Alloy 800HT coupon (with 3.6 mg/dm^2 WG) are shown in Figure 4-16. Plate-like oxide islands were embedded on the corroded surface. SEM/EDS analysis on the oxide islands indicated that they were enriched in Fe, Cr, Mn and O. Figure 4-16(b) shows a high magnification image of the clean oxide scale on the surface. These area seemed to have a slightly rough surface consisted of nano grains. Since the oxide thickness was much smaller than the electron interaction volume, an SEM/EDS analysis on the clean oxide scale was not reliable to be deemed. The following TEM analysis was conducted on the site-specific location in the sample, shown in Figure 4-16(c) with a red dashed rectangle which was prepared via FIB milling. An ISE image of the final TEM sample attached to a TEM copper (Cu) grid [Figure 4-16(d)] showed that a localized corroded area (oxide crater) was formed directly below the oxide island and further away from a grain boundary. Recrystallized grains were also observed at the alloy/oxide interface. To ensure the above perception is not centralized in one spot, two more remote region oxide islands were ion milled via FIB and ISE images were obtained from their cross sections [Figure 4-16(e) and Figure 4-16(f)].

Also, some scattered nodules were observed on the oxide scale on Alloy 800HT coupon. Figure 4-17 shows SEM images of these nodules that were cut across using FIB. SEM/EDS analysis on the particles showed they were enriched in carbon (C), calcium (Ca), Cr and O. The presence of C and Ca was most probably as a result of surface contamination. As no oxide crater was observed below these nodules they were most likely deposited from solution therefore were not accounted as corrosion products.

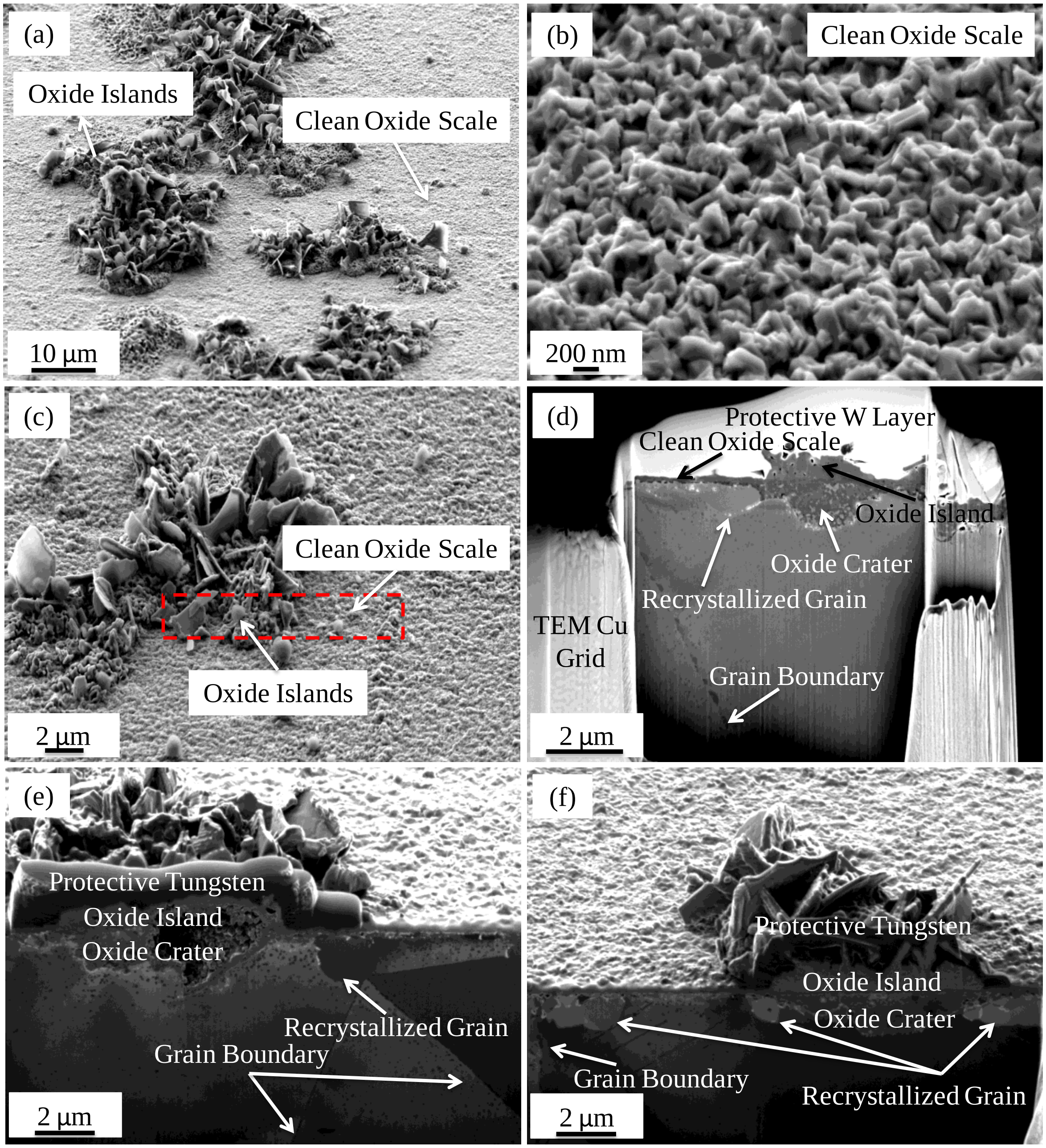

Figure 4-16(a) Low magnification and (b) high magnification plan view SEM images of the corroded Alloy 800HT surface, (c) plan view SEM image showing an area of interest, framed with a dashed rectangle, on the corroded Alloy 800HT surface for TEM sample preparation, (d) cross-section ISE image of the final TEM oxide-scale/alloy thin foil attached to a TEM Cu grid, (e) and (f) ISE images of the FIB-milled trenches excavated through two other oxide islands.

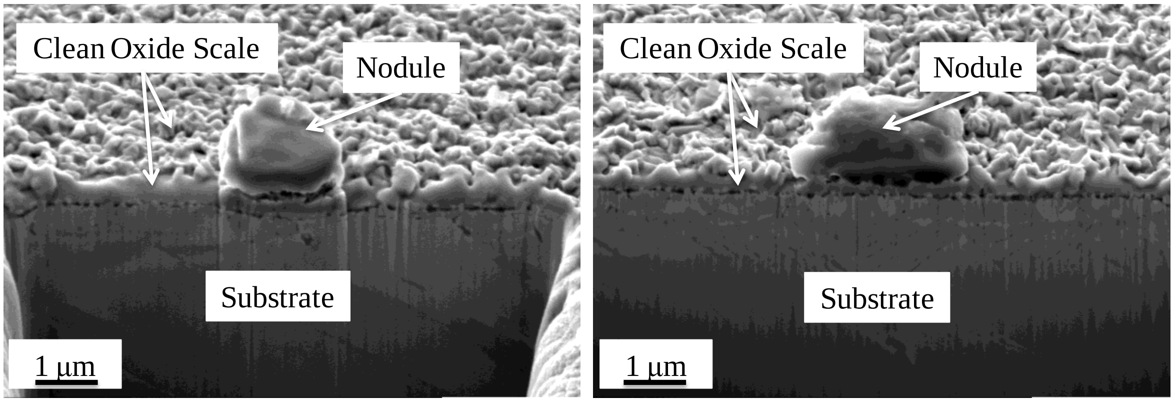

Figure 4-17 SEM cross-section images from the scattered nodules deposited from solution on Alloy 800HT coupon exposed 25 MPa SCW at 625 °C for 500 h.

Figure 4-18(a) shows a low magnification BF-STEM image of the corroded Alloy 800HT coupon in cross section. Figure 4-18(b)-(j) illustrates the associated STEM/EDS maps of the protective W layer deposited on the coupon and all the elements present in the coupon that were believed to form a possible oxide that could affect the corrosion resistance of the alloy. Oxide island formed on the clean oxide scale were enriched in Cr, Fe, Mn and O. Oxide crater was enriched in Cr, Mn and O. Also Fe and Ni were observed in the oxide crater but closer to the substrate. Cr, Fe, Mn and O were found in the clean oxide scale. Ni was mostly enriched at the alloy/oxide interface. Very small amount of Si, Ti and Al accompanied with O was also seen below the clean oxide scale.

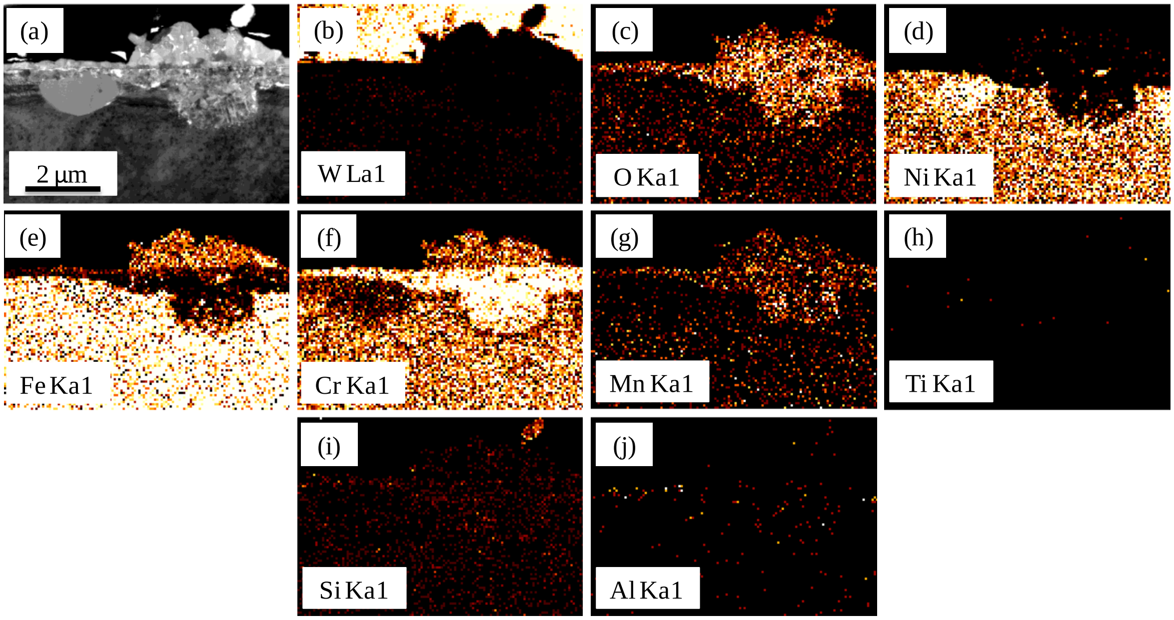

Figure 4-18 (a) Low magnification BF-STEM image and (b)-(j) STEM/EDS elemental maps for W, O, Ni, Fe, Cr, Mn, Ti, Si and Al in the corroded Alloy 800HT.

BF-STEM image of the Alloy 800HT TEM sample is shown in Figure 4-19(a). Oxide islands were affirmed to have two dissimilar types of grains yet same spinel structure. SAD patterns were an excellent match to $[Fe,Mn,Cr]_3O_4$ [area 1 in Figure 4-19(a)] and $[Fe,Mn]Cr_2O_4$ [area 2 in Figure 4-19(a)] reference patterns whereas all core-loss EELS spectra, specifically O-K edges were a clear representative of both phases having the same spinel structure. Area 3 in Figure 4-19(a) also known as oxide crater was characterized using both SAD and EELS. Although the small grain size of the oxide crater resulted in extra spots in the SAD pattern, it was best fitted as being composed of $[Cr,Mn]_2O_3$. STEM/EDS analysis showed the presence of up to 4 wt% dissolved Fe and Ni in the oxide crater precisely in the areas closer to the oxide crater/substrate which can result in the formation of a mixed spinel $[Cr,Mn,Fe,Ni]_3O_4$.

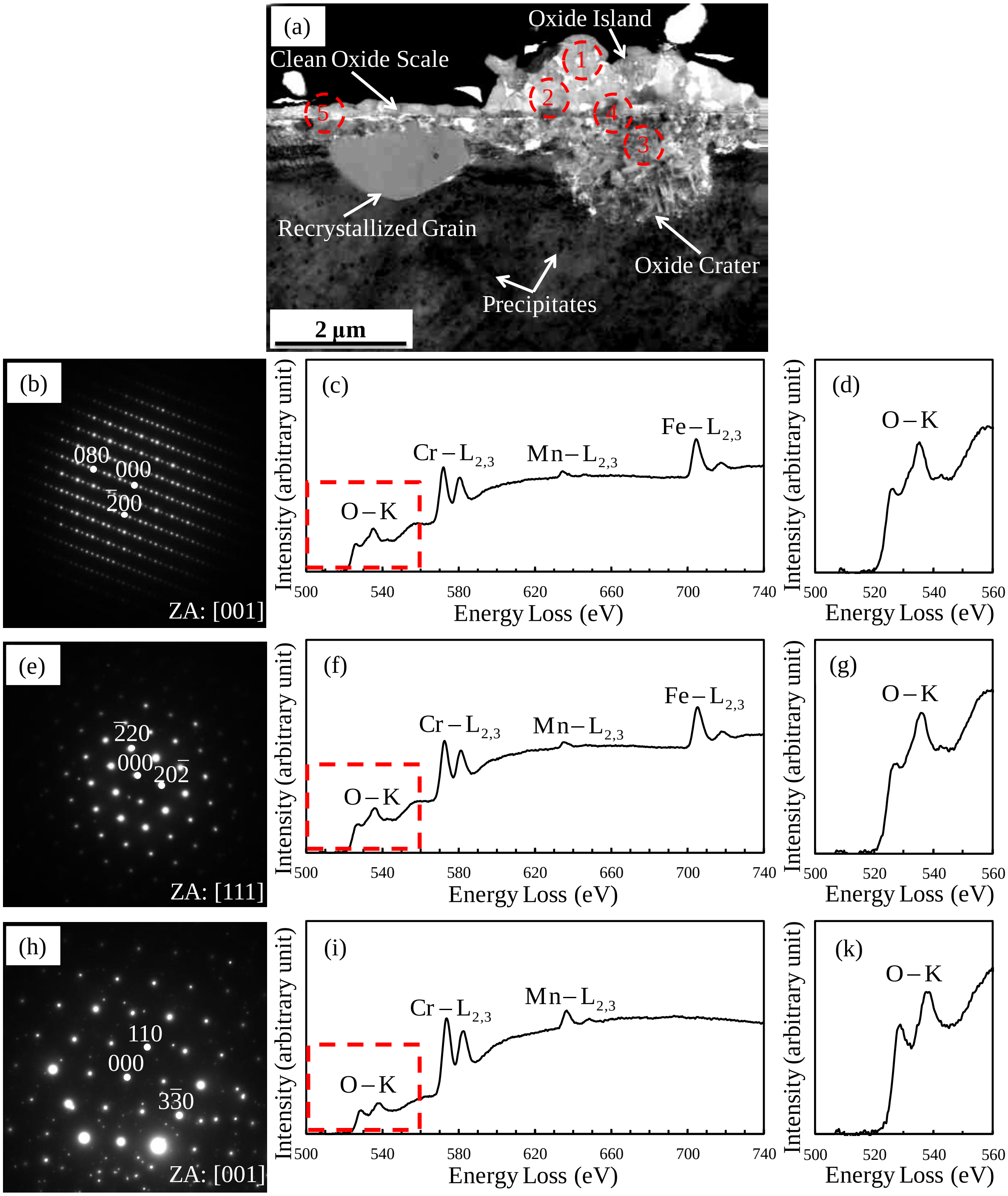

Figure 4-19(a) BF-STEM cross-section image of corroded Alloy 800HT, (b) SAD pattern of area 1, $[Fe,Mn,Cr]_3O_4$, (c) and (d) EELS spectra of $[Fe,Mn,Cr]_3O_4$ (e) SAD pattern of area 2, $[Fe,Mn]Cr_2O_4$, (f) and (g) EELS spectra of $[Fe,Mn]Cr_2O_4$, (h) SAD pattern of area 3, $[Cr,Mn]_2O_3$, (c) and (d) EELS spectra of $[Cr,Mn]_2O_3$.

High magnification BF-STEM image of area 4 in Figure 4-19(a); area between oxide island and oxide crater; is represented in Figure 4-20(a). It seemed as to this area was composed of fine grains. EELS spectra within the red dashed line were best fitted as to be $[Cr,Fe]_2O_3$ [Figure 4-20(b) and Figure 4-20(c)].

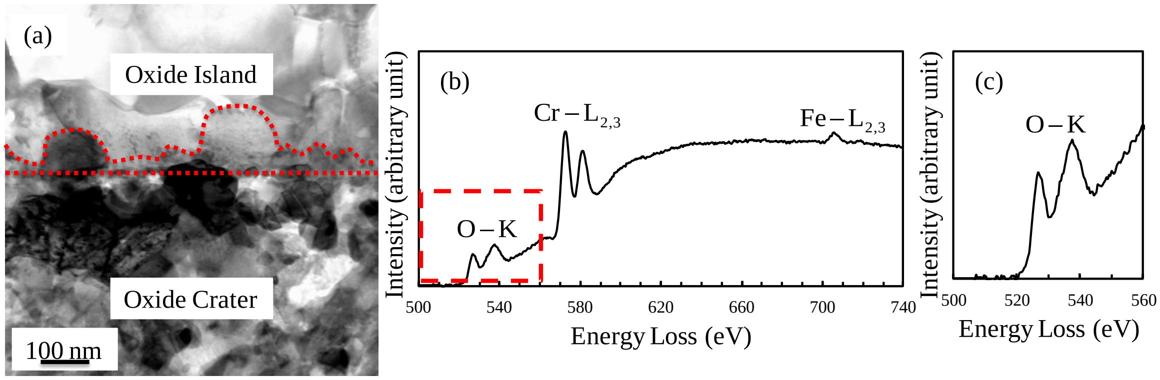

Figure 4-20(a) High magnification BF-STEM image of the oxide island/oxide crater interface of Alloy 800HT, (b) EELS spectra of the assigned area shown in part (a), and (c) the corresponding O-K edge EELS spectra of the dashed rectangular area shown in part (b).

Figure 4-21(a) represents a BF-STEM image of the clean oxide scale formed on Alloy 800HT and the STEM/EDS elemental maps of the possible oxide forming alloying elements are shown in Figure 4-21(b)-(j). The clean oxide scale was enriched in Cr, Mn and O while small amount of Fe was also observed in this scale. The area beneath the clean oxide scale with the thickness of 633±62 nm was depleted in Cr and Mn and was enriched in Fe and Ni instead. A very thin layer below the clean oxide scale was enriched in Ti, Si and O. The thickness of this layer was 62±8 nm measured by ImageJ software [64]. Also Al enrichment was detected in some scattered area in the substrate.

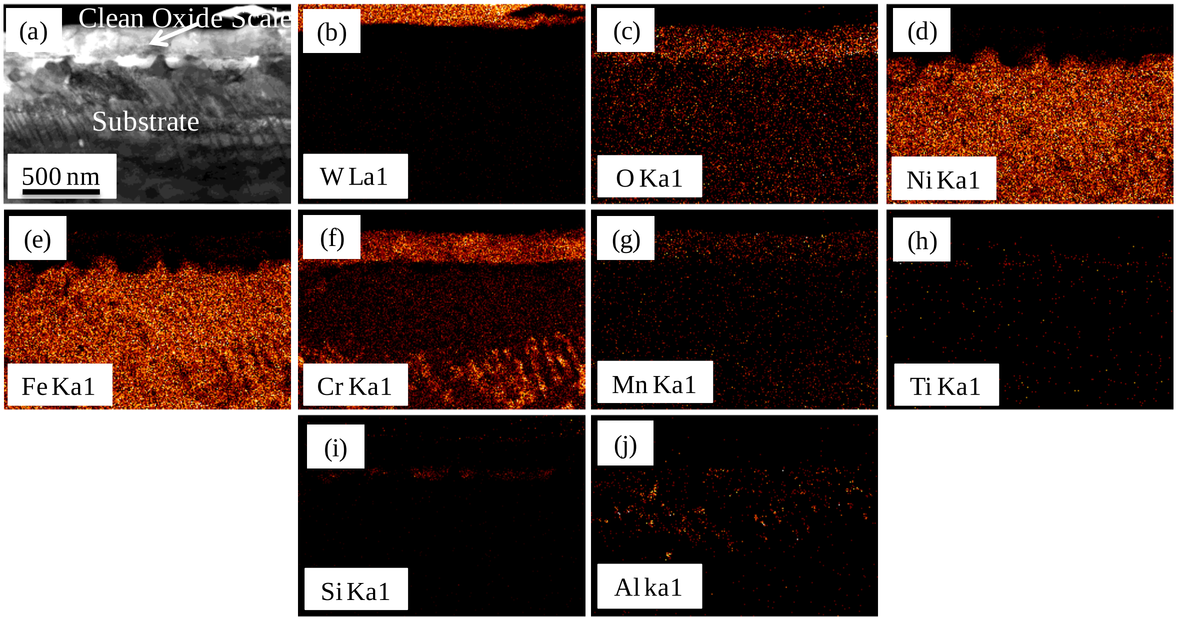

Figure 4-21 BF-STEM image and STEM/EDS elemental maps of the clean oxide scale/alloy interface for W, O, Ni, Fe, Cr, Mn, Ti, Si and Al in Alloy 800HT.

Figure 4-22 shows a BF-STEM image of the clean oxide scale and the three areas through the scale where the following EELS spectra were extracted. Near to alloy/oxide interface (area 1) the dominate phase was best characterised to be $[Cr,Fe]_2O_3$ where almost no Mn was detected. In areas 2 and 3 however, Mn-$L_{2,3}$ peaks were visibly identified. It seemed that unlike our previous 550 °C results, the higher exposure temperature used here (625 °C), assisted Mn diffusion all through the scale to incorporate in the formation of an outer $[Fe,Mn]Cr_2O_4$ spinel scale.

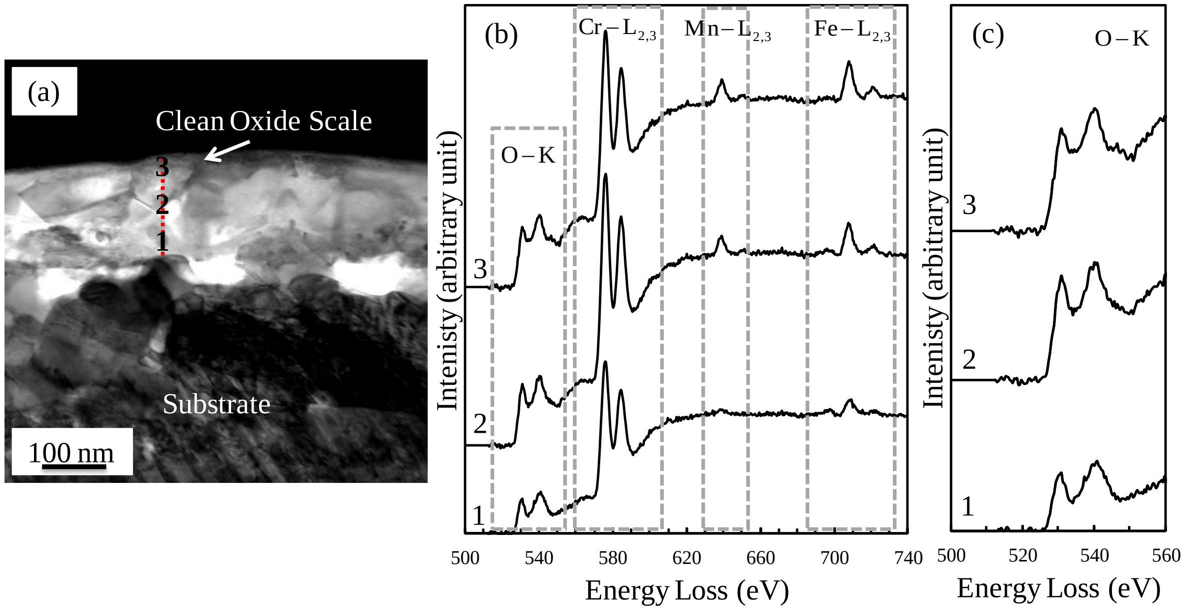

Figure 4-22(a) High magnification BF-STEM image of the clean oxide scale formed on Alloy 800HT, (b) EELS spectra of areas 1, 2 and 3 representing $[Cr,Fe]_2O_3$, $[Cr,Fe,Mn]_2O_3$ and $[Fe,Mn]Cr_2O_4$ and (c) the corresponding O-K edge EELS spectra.

Figure 4-23 presents the average atomic concentration ratio for Cr, Fe, Ni and Mn acquired by AES after three separate measurements on the clean oxide scales. The top most areas in the oxide scale were enriched in Cr, Fe, Mn and also less amount of Ni which was consistent with the formation of the spinel layer on top of a $[Cr,Fe]_2O_3$ layer. Not to mention, depth of Cr depleted zone was larger than the AES depth profile measured.

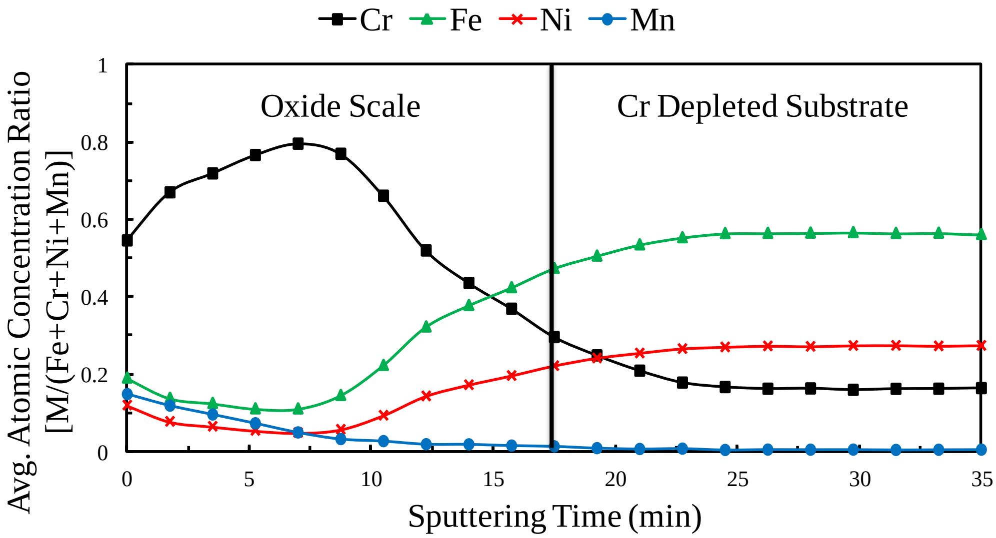

Figure 4-23 Avg. atomic concentration ratio depth profile for Cr, Fe, Ni and Mn obtained by AES in Alloy 800HT exposed in SCW at 625 °C for 500 h.

Two diverse morphologies of precipitates were formed in Alloy 800HT coupon which are shown in the BF-STEM images in Figure 4-24. Within the grains [Figure 4-24(a)], precipitates had cuboidal morphology. STEM/EDS point analysis on these precipitates showed they were enriched in Cr with up to ~ 49 wt.% and the C content up to 1.1 wt.% which is a lot larger than the C content in matrix of Alloy 800HT (with 0.07 wt.%). Therefore, they were most probably $M_{23}C_6$. Precipitates along the grain boundary [Figure 4-24(b)] seemed somewhat brighter with trapezoid shape. STEM/EDS analysis showed they were enriched in Cr , Ti and C most likely to be Cr-rich $M_{23}C_6$ precipitates as well. Figure 4-24(c) shows a STEM/EDS line scan across the grain boundary with precipitate which shows the Cr depletion around the precipitate (<100 nm) and Cr enrichment in the precipitate together with C and Ti enrichment.

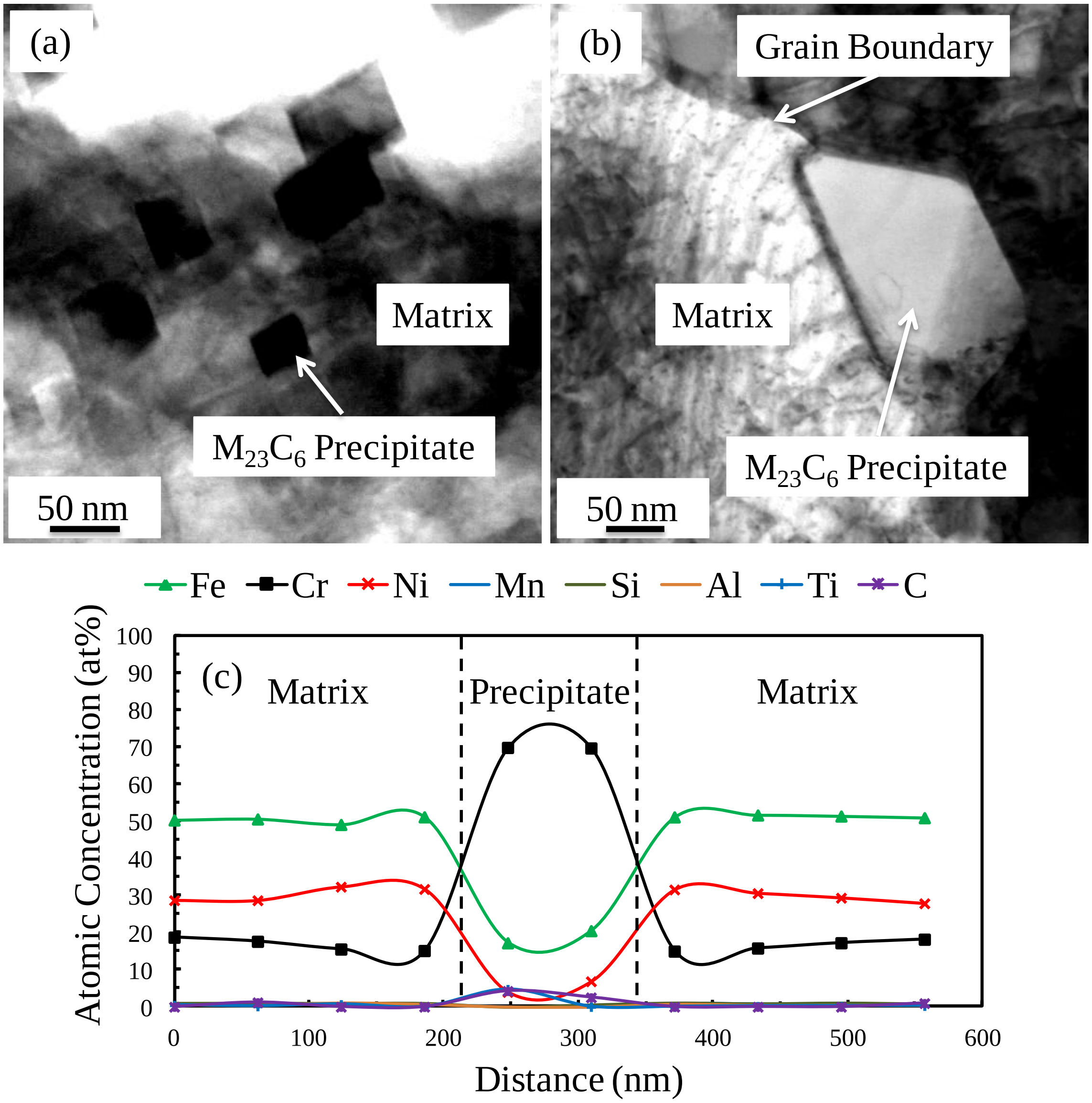

Figure 4-24 BF-STEM images of $M_{23}C_6$ precipitates formed in the corroded Alloy 800HT coupon (a) inside the grain and (b) in the grain boundary.

4.2.2. Alloy 33

Figure 4-25 shows the photograph of the corroded Alloy 33 coupons after exposure in SCW at 625 °C for 500 h. Coupons surfaces same as when they were exposed in 550 °C SCW had "rainbow" appearance in bright colors. In addition, no macroscopic cracks or blisters were observed on the coupon surfaces. However, coupon number 1 surface had an area with slightly different colored, close to purple, surface.

Figure 4-25 Image showing the appearance of the exposed Alloy 33 coupons after exposure in 25 MPa SCW at 625 °C for 500 h.

Table 4-7 shows the avg. coupons WG after exposure in SCW. The avg. WG for the corroded Alloy 33 coupons using the 95% Confidence Intervals (CI) was ~ 2.2 ± 1.2 (mg/dm^2). Note that values in Table 4-7 were rounded to the nearest 4 decimal places.

Table 4-7 WG measurement data on the four corroded Alloy 33 coupons exposed in SCW at 625 °C for 500h

Coupon #	WG (mg/dm^2)	Avg. WG (mg/dm^2)	WG by 95% CI (mg/dm^2)
(1)	1.0938	2.2382 ~ 2.2	2.2382 ± 1.2166
(2)	2.5992		
(3)	2.6913		
(4)	2.5683		

The descaling process to measure the WL was performed only on coupon number 1 with ~ 1.1 mg/dm^2 WG. Table 4-8 shows the WL value was ~ 12.0 mg/dm^2. A reference coupon of Alloy 33 was also exposed in the same descaling run to make sure the subsurface was not removed by the descaling solution during the procedure.

Table 4-8 WL measurement data on the corroded Alloy 33 coupon (number 1) exposed in SCW at 625 °C for 500h

Coupon Type	WL (mg/dm^2)
Corroded	11.9873 ~ 12.0
Reference	0.0001

High magnification SEM plan view image of a corroded Alloy 33 coupon (2.6 mg/dm^2 WG) is shown in Figure 4-26(a). Surface of the alloy was mostly covered with a clean oxide scale with finer surface than Alloy 800HT consisting nano grain oxides. Unlike Alloy 800HT no oxide island was seen on top of the oxide formed on Alloy 33. Very few scattered nodules were observed on the surface of the alloy. SEM/EDS confirmed that a few of these particles were enriched in Ce which did not have any contribution in the oxide formation [68]. Other nodules were enriched mostly in Cr and Mn on the other hand. The following TEM analysis was conducted on the site-specific location in the sample, shown in Figure 4-20(b) with a red dashed rectangle which was prepared via FIB milling. This site was chosen in order to include both clean oxide scale and one of the [Cr,Mn]-rich particles in the final sample. An ISE image of the final TEM sample attached to the TEM Cu grid is brought in Figure 4-20(c). Recrystallized grains were observed in the alloy/oxide interface. Also, close to the alloy/oxide interface precipitates were formed most probably in the direction as the grain orientation.

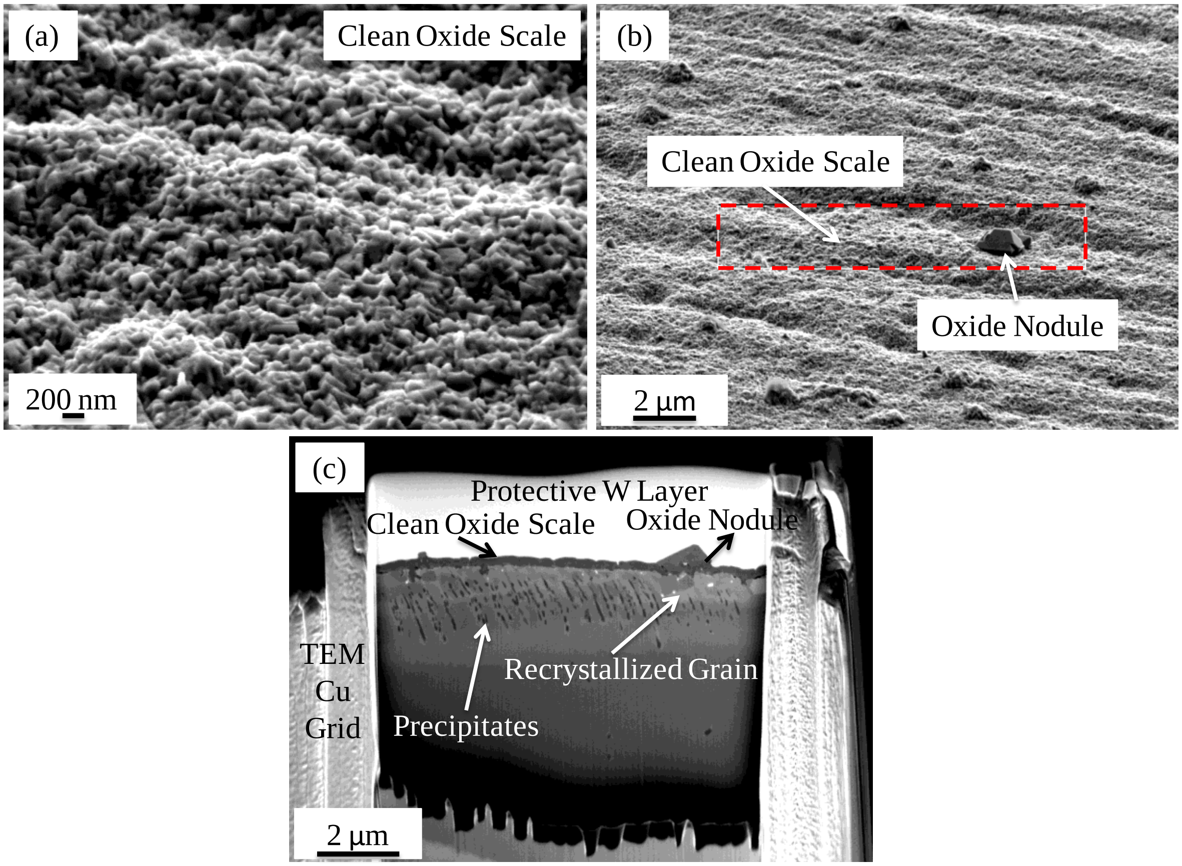

Figure 4-26(a) Plan view high magnification SEM image of the corroded Alloy 33 surface (b) low magnification image plan view SEM image showing an area of interest, framed with a dashed rectangle, on the corroded Alloy 33 surface for TEM sample preparation and (c) cross-section ISE image of the final TEM oxide-scale/alloy thin foil attached to a TEM Cu grid.

STEM/EDS analysis on some other scattered particles (very few decorated the surface) that were not enriched in Ce showed the presence of Cr and O in them. Figure 4-27 shows the SEM images of the nodules cut in cross-section using FIB. As no oxide crater was seen below the oxide nodules they were most likely deposited from solution therefore were not accounted as a corrosion product to be examined in the current work.

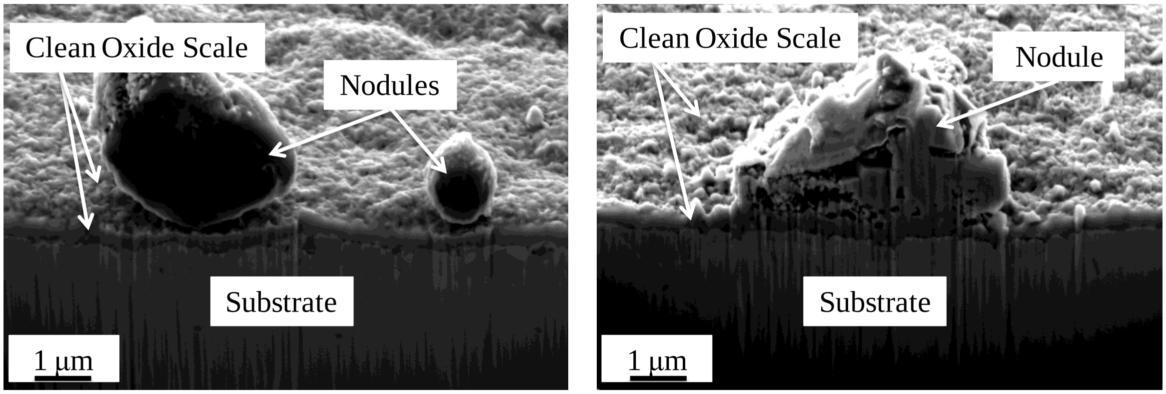

Figure 4-27 SEM cross-section images from the scattered nodules deposited from solution on Alloy 33 coupon exposed 25 MPa SCW at 625 °C for 500 h.

Figure 4-28(a) shows a low magnification BF-STEM image of the corroded Alloy 33 coupon in cross section. Figure 4-28(b)-(j) illustrates the associated STEM/EDS maps of the protective W layer deposited on the coupon and all the elements present in the coupon that were believed to form a possible oxide that could affect the corrosion resistance of the alloy. Oxide nodule on the clean oxide scale was enriched in Cr, O, Mn, Fe and small amount of Ni. No oxide crater was seen below the nodule. These oxide nodule could be deposited from the solution or could be a corrosion product. Nonetheless, due to high Cr content in Alloy 33 substrate that can fill in the clean oxide scale and provide Cr loss from nodule formation, the presence of such low population nodules on the surface were not appeared to cause any interference in the corrosion resistance behaviour of Alloy 33. Very small amount of Si and Ti accompanied with O was also seen below the clean oxide scale.

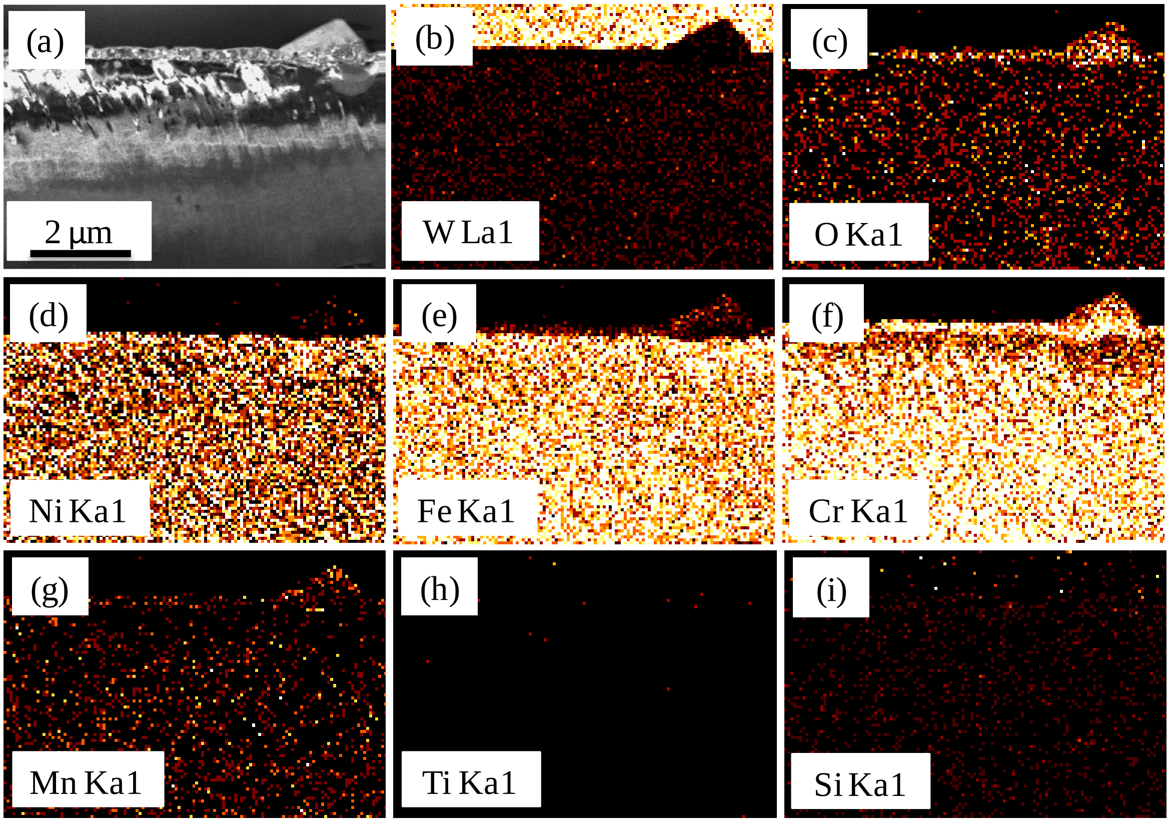

Figure 4-28(a) Low magnification BF-STEM image and (b)-(j) STEM/EDS elemental maps for W, O, Ni, Fe, Cr, Mn, Ti and Si in the corroded Alloy 33.

A BF-STEM image is shown in Figure 4-29(a) followed by a series of STEM/EDS elemental maps from the clean oxide scale/substrate area in Alloy 33 [Figure 4-29(b)-(h)]. The clean oxide scale was enriched in Cr and O with ~80 wt.% Cr. Mn was also seen in the clean oxide scale mostly enriched in the top most area. Also Fe was observed in the clean oxide scale. Almost no Ti was detected in the elemental map due to its low concentration in the alloy. Si and O enrichment was however seen below the clean oxide scale. The thickness of the Si-O-rich layer was 46±7 nm. A depleted Cr and Mn zone was formed below the original surface of the alloy with the depth of 401±43 nm. In addition, directed precipitates mostly enriched in Cr and Mn and depleted in Fe and Ni were found to be formed after the Cr and Mn depleted zone.

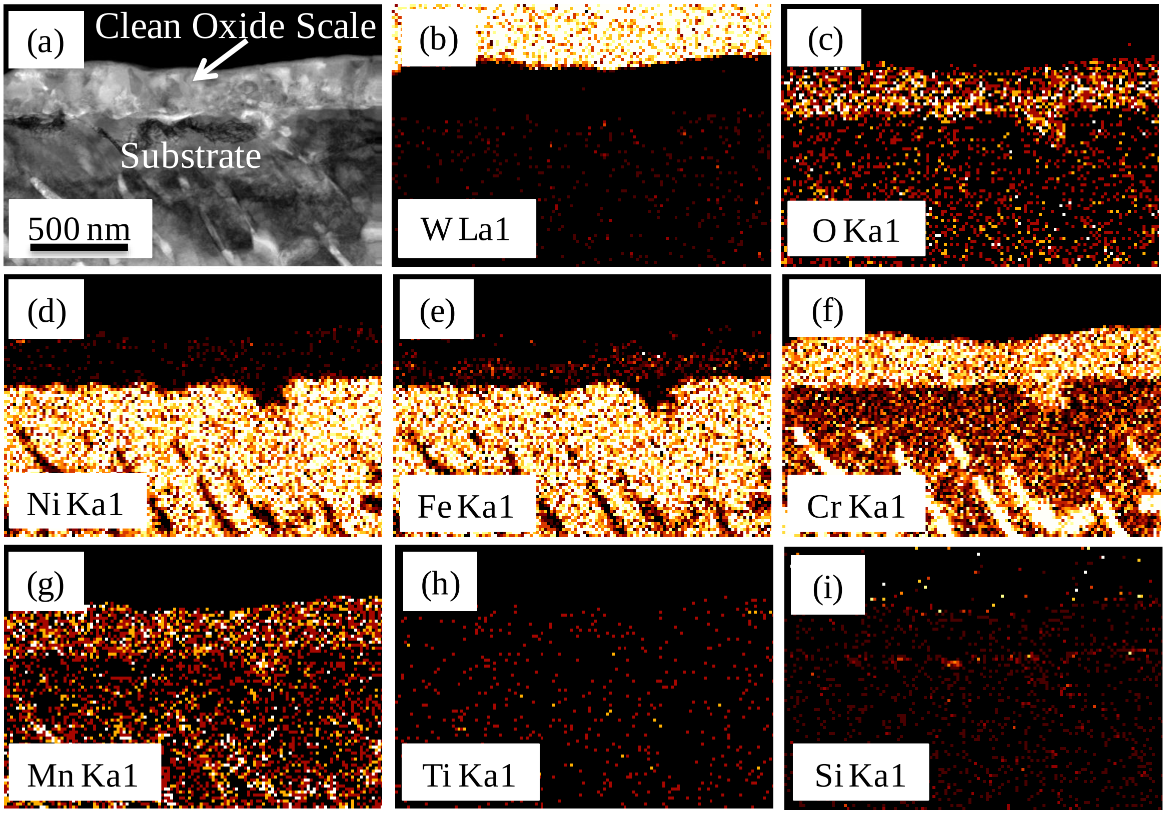

Figure 4-29 BF-STEM image and STEM/EDS elemental maps of the clean oxide scale/alloy interface for Cr, O, Ni, Fe, Mn, Ti and Si in Alloy 33.

Figure 4-30(a) shows a BF-STEM image of the clean oxide scale and the three areas through the scale where the following EELS spectra were extracted. Near to alloy/oxide interface and in the middle of the oxide scale (areas 1 and 2) the dominate phases were best characterised to be $[Cr,Fe]_2O_3$ where almost no Mn was detected. Same as Alloy 800HT, In area 3 however, Mn-$L_{2,3}$ peaks were evidently recognized. The EELS spectra from area 3 was best characterized to be $[Cr,Fe,Mn]_2O_3$.

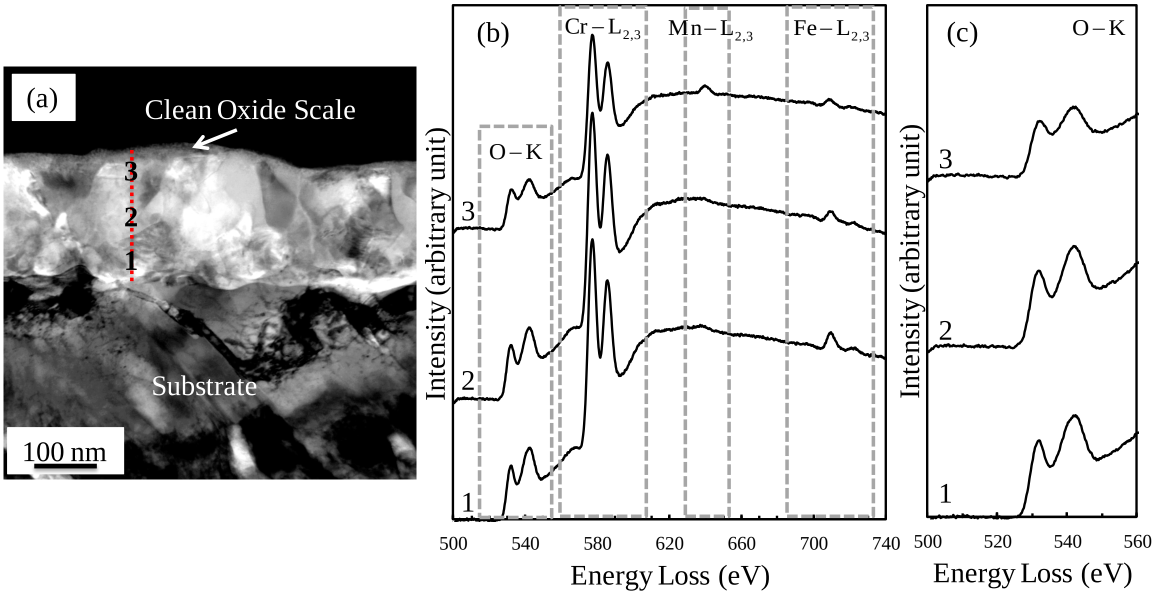

Figure 4-30(a) High magnification BF-STEM image of the clean oxide scale formed on Alloy 33, (b) EELS spectra of areas 1, 2 and 3 representing $[Cr,Fe]_2O_3$, $[Cr,Fe]_2O_3$ and $[Cr,Fe,Mn]_2O_3$ and (c) the corresponding O-K edge EELS spectra.

Figure 4-31 shows a BF-STEM image of the precipitate forming in the corroded Alloy 33 and the relative EELS spectra. STEM/EDS analysis showed that precipitates were enriched in up to 90 wt.% Cr and up to 0.9 wt.% C (compared with 0.01 wt.% C existing in the matrix). EELS spectra confirmed the presence of Cr, Mn-$L_{2,3}$ as well as Fe-$L_{2,3}$ edges. Fe and Mn peaks were likely coming from substrate (Figure 4-29).

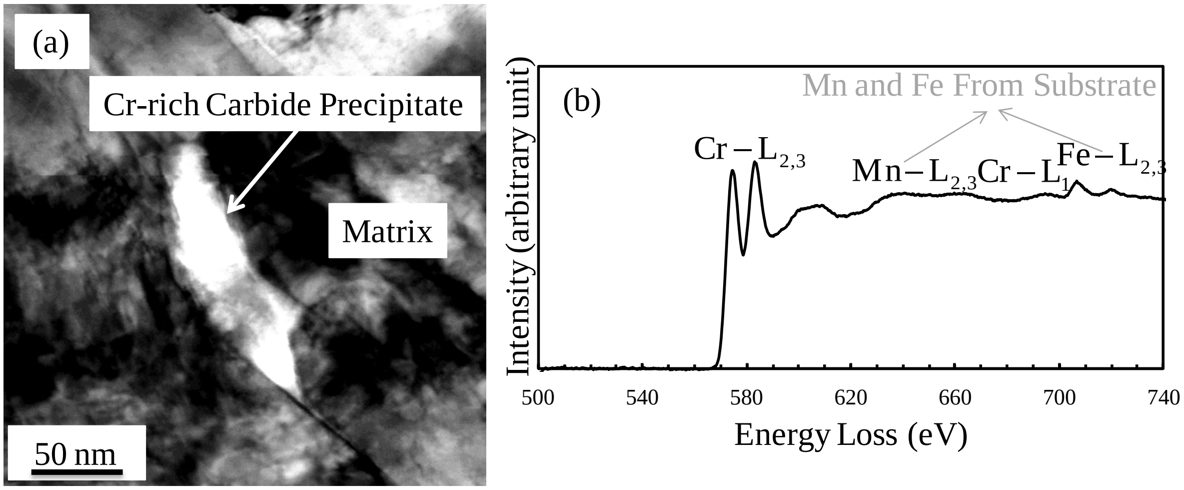

Figure 4-31(a) BF-STEM image of Cr-rich carbide precipitate formed in the corroded Alloy 33 coupon and (b) corresponding EELS spectra.

The average atomic concentration ratio for Cr, Fe, Ni and Mn acquired by AES after three separate measurements on the clean oxide scales is illustrated in Figure 4-32. The top most areas in the oxide scale were enriched in Cr, Fe, Mn and also less amount of Ni. The inner layer on the other hand, had corundum M_2O_3 structure. It is worth mentioning that Fe was detected more in the surface of oxide scale from the AES depth profile than from the STEM/EDS analysis. The reason for this is not clear, however, this might be due to Fe and Cr very close intensity peaks that can overlap during AES results processing.

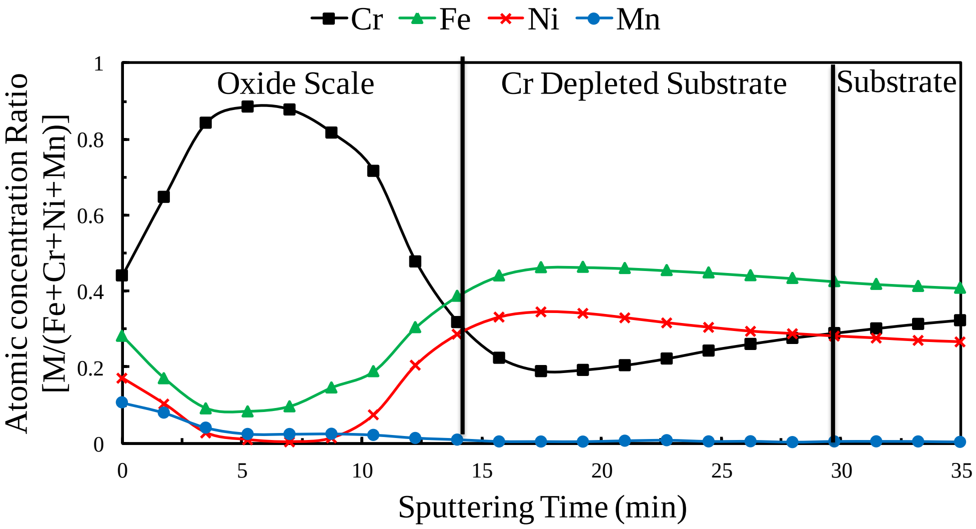

Figure 4-32 Avg. atomic concentration ratio depth profile for Cr, Fe, Ni and Mn obtained by AES in Alloy 33 exposed in SCW at 625 °C for 500 h.

5. Discussion

5.1. Corrosion Resistance at 25 MPa and 550 °C SCW

Figure 5-1 shows a schematic summary of the multi-layer oxide scale that formed on each alloy after short-term exposure (500 h) in 25 MPa SCW at 550 °C. A similar schematic for Type 316L stainless steel is provided for context. The higher bulk Cr content in both Alloy 800HT and Alloy 33 promoted the formation of a corundum-type M_2O_3 (where M = Fe, Cr and Mn) external base layer, which did not form on Type 316L stainless steel. The composition of the corundum-type M_2O_3 external layer depended on the alloy: the layer formed on Alloy 33 contained a significantly lower Fe content than that formed on Alloy 800HT. The higher bulk Cr content of Alloy 33 prevented the formation of an outer spinel-type M_3O_4 (where M = Fe, Cr and Ni) external layer, which had formed on Alloy 800HT. The higher bulk Cr content of Alloy 33 also prevented an apparent twin boundary-induced enhanced internal oxidation zone that formed a multi-layer scale resembling what formed on Fe-Cr-Ni alloys with a lower Cr content (Type 316L stainless steel in this case).

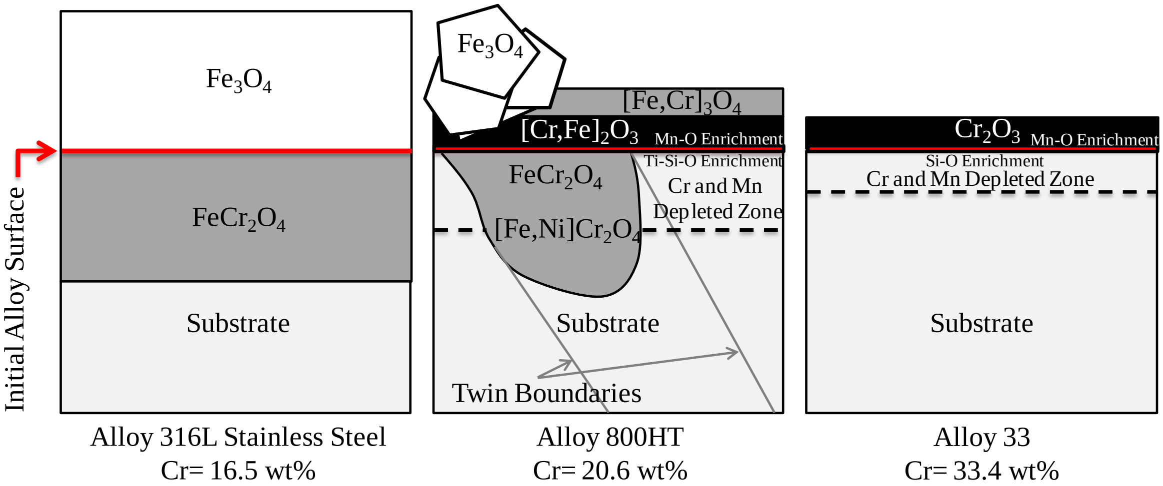

Figure 5-1 Summary of oxide scale structure and composition formed on austenitic Fe-Cr-Ni alloys after exposure in 25 MPa SCW at 550 °C for 500 h.

The critical Cr concentration for transforming less-protective internal oxidation ($FeCr_2O_4$) into more-protective external oxidation (M_2O_3) which decreases O inward diffusion in the substrate in an austenitic Fe-Cr-Ni alloys is reported to be approximately 20 wt.% [42, 50, 51]. It has been argued that a spinel $FeCr_2O_4$ layer is less protective than a Cr-rich M_2O_3 layer because Fe diffusion in a spinel $FeCr_2O_4$ layer is three times faster than Cr [69], whereas Fe and Cr diffusion coefficients in a Cr_2O_3 layer are reported to be quite similar [70]. The formation of a $[Fe,Cr]_3O_4$ layer on top of the protective corundum-type M_2O_3 external layer has been explained by the solubility of Fe in Cr_2O_3, which permits its outward diffusion to the oxide surface [71,72]. The critical Cr concentration to prevent this formation from happening is reported to be 25 wt.% [52]. It has been argued that an increase in the bulk Cr content reduces the Fe activity in the near-surface region, correspondingly reducing the Fe solubility in Cr_2O_3 [73]. The formation of a corundum-type M_2O_3 external layer on Alloy 800HT (20.6 wt.% Cr) and Alloy 33 (33.4 wt.% Cr) as well as the absence of an outer $[Fe,Cr]_3O_4$ layer formed on Alloy 33 is consistent with these reported tendencies. Thus, the formation of the corundum-type M_2O_3 external layer was likely responsible for the improved corrosion resistance of Alloy 800HT and Alloy 33 relative to Type 316L stainless steel [Figure 5-1(a)]. Moreover, the higher bulk Cr content and correspondingly lower Fe activity in Alloy 33 was likely responsible for the improved corrosion resistance relative to Alloy 800HT [Figure 5-1(b)].

The sustained growth of the protective M_2O_3 external layer is well known to be dependent on the Cr diffusion: not only from grains and grain boundaries in the near-surface region, but also from grains and grain boundaries deeper in the alloy [74-76]. Such a condition tends to form a measurable Cr-depleted zone in the alloy: the higher the alloyed Cr content, the shallower the depleted zone. Figure 5-2 shows the average normalized concentration (STEM/EDS) depth profiles for each of the alloying elements that incorporated into the protective M_2O_3 external layer, as acquired from three sets of measurements across the oxide scale/alloy interface. As expected, depth of the Cr-depleted zone formed in Alloy 800HT was significantly deeper (nearly four times as deep) than that formed in Alloy 33. The difference in depletion zone depth was likely influenced by differences in both the bulk Cr content and the grain size (grain boundary area): a higher bulk Cr content and smaller grain size leading to a significantly shallower Cr-depleted zone in Alloy 33. In addition, Fe concentration in the oxide scale formed on Alloy 800HT was somewhat more than that in the Alloy 33 oxide layer, representing a less protective oxide scale formed on Alloy 800HT.

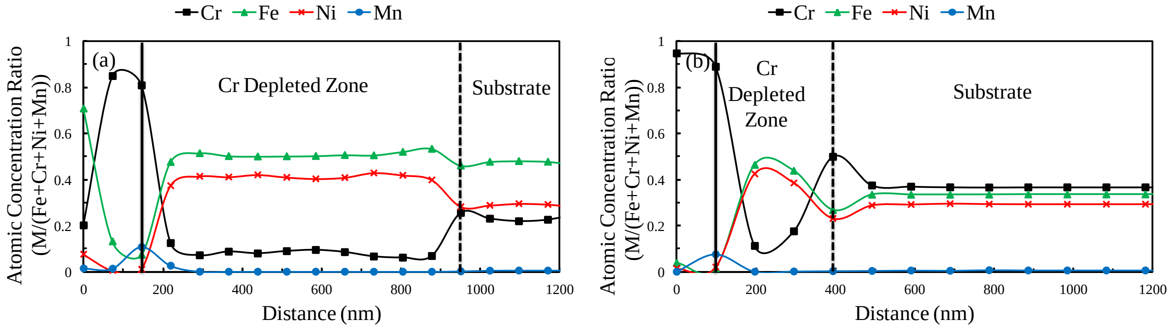

Figure 5-2 Atomic concentration ratio depth profile of Cr, Fe, Ni and Mn for (a) Alloy 800HT and (b) Alloy 33 exposed to 25 MPa SCW at 550 °C for 500 h.

Table 5-1 lists the thickness of the major M_2O_3 oxide layers formed on Alloy 800HT and Alloy 33 obtained from STEM images of the thin foil cross-sections measured using the ImageJ software [64]. The table includes the ratio of average thickness (t_{avg}) to the maximum thickness (t_{max}), which follows the rationale that this value can be used to semi-quantitatively compare the uniformity and compactness of a given oxide layer [34]. The closer this ratio is to 1, the more uniform and compact and, thus protective the oxide layer is assumed to be. Based on the total oxide scale thickness observed, the M_2O_3 layer formed on Alloy 33 is expected to be the most protective, whereas the M_2O_3 layer formed in between the oxide island and crater on Alloy 800HT is expected to be the least protective. The values of the t_{avg}/t_{max} ratio listed in Table 5-1 are consistent with this expectation: 0.91 for the M_2O_3 layer formed on Alloy 33, 0.65 for the clean M_2O_3 layer formed on Alloy 800HT and 0.56 for the M_2O_3 layer formed in between the oxide island and crater formed on Alloy 800HT.

Table 5-1 Oxide thickness measurement using ImageJ software [64]

		Oxide Thickness (nm)		
Alloy	**Oxide Type Formed On The Alloy**	t_{max}	t_{avg}	t_{avg}/t_{max}
800HT	$[Fe,Cr]_3O_4$	71	41±9	0.58
	Clean Oxide Scale: $[Cr,Fe]_2O_3$	182	118±12	0.65
	Oxide Island/Crater Int.: $[Cr,Fe]_2O_3$	117	66±12	0.56
33	Cr_2O_3	154	140±6	0.91

The apparent increased susceptibility to corrosion by SCW exhibited by the twins present in Alloy 800HT is not clear at this time. The formation of an oxide scale similar in composition and structure to the one formed on a Fe-Cr-Ni alloy with a Cr content less than the critical 20 wt.% Cr (Type 316L in this case) suggests that the twins had a lower Cr content than the grain in which they formed. However, no such obvious Cr depletion relative to the bulk was found upon conducting an EDS spot analysis at several locations in the matrix ahead of the internal (crater) oxidation front. A more detailed examination of this behavior will be the focus of future work. Regardless, the formation of the internal $FeCr_2O_4$ craters on Alloy 800HT is undesirable from a corrosion resistance perspective since this oxide phase readily supports significant Fe diffusion and, thus mass loss.

As already mentioned, the oxide scales that formed on both Alloy 800HT and Alloy 33 were multi-layered in structure. It has been argued that the corrosion resistance of both alloys is controlled to a large extent by the formation the external M_2O_3 layer. A very thin oxide layer was found to have formed in between the clean M_2O_3 external layer and alloy substrate on both alloys. This thin oxide layer was enriched with Ti and Si on Alloy 800HT and just Si on Alloy 33. Since Ti oxide (TiO_2) and Si oxide (SiO_2) are more stable than Cr_2O_3, they tend to form a layer/precipitate underneath a M_2O_3 layer on Fe-Cr-Ni alloys when present as a minor alloying element above a critical concentration [77-80]. The thickness of the Ti-Si oxide layer (Alloy 800HT) and Si oxide layer (Alloy 33) was measured to be 15±3 nm and 13±2 nm respectively. Such thin scales are not considered to have played an important role in affecting the key diffusion processes involved in oxide scale formation and, thus corrosion resistance [78]. Finally, it is worth mentioning that Ce oxides below the Cr_2O_3 scale too are well known to improve the high temperature corrosion resistance of Fe-Cr-Ni alloys when Ce is present as a minor alloying element above a critical concentration by increasing the adhesion of the oxide scale [81-84]. This effect was not observed in Alloy 33. The origins of the formation of the internal CeO_2 zone observed in the Alloy 33 substrate is not clear at this time. Regardless, this oxide phase is believed to not have had any significant influence on the formation and protectiveness of the external M_2O_3 layer.

5.2. Corrosion Resistance at 25 MPa and 625 °C SCW

Figure 5-3 shows a schematic summary of the multi-layer oxide scale that formed on each alloy after short-term exposure (500 h) in 25 MPa SCW at 625 °C. As explained earlier, the formation of a corundum-type M_2O_3 external base layer on Alloy 800HT and Alloy 33 is due to the presence of at least 20 wt.% Cr content in these alloys which is believed to be around the critical value for the transition from internal to external oxidation in Fe-Ni-Cr austenitic alloys: thus forming a single M_2O_3 (M=Cr and/or Fe) layer mixed with alloying element oxides [42,50,51]. Also, presence of a Cr content higher than 25 wt.% (as in Alloy 33) prevented the formation of an outer spinel M_3O_4–type (where M = Fe, Cr, Mn and Ni) layer on top of the M_2O_3 layer, therefore a slightly thinner oxide scale was formed on Alloy 33.

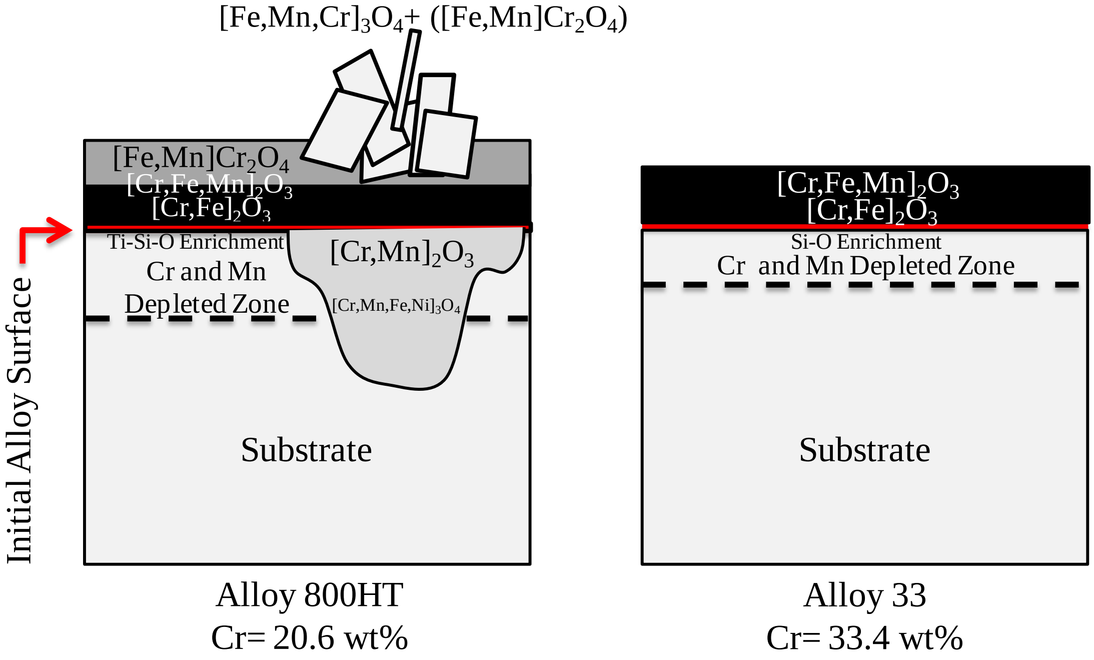

Figure 5-3 Summary of oxide scale structure and composition formed on austenitic Fe-Cr-Ni alloys after exposure in 25 MPa SCW at 625 °C for 500 h.

A comparison between Figure 5-1 and Figure 5-3 show that while the oxide scales structure on both Alloy 800HT and Alloy 33 at higher exposure temperature remained the same, diffusion of alloying elements such as Fe, Mn and/or Ni through the M_2O_3 layer increased with the increase in temperature as expected. Therefore, it is important to discuss the role of the increased dissolved ion concentration in the M_2O_3 layer on the oxide layer protectiveness. This is especially true for Fe and Mn since they are the major alloying elements that were observed in the M_2O_3 layer (considering Ni showed very small diffusivity in the M_2O_3 scale).

Fe diffusion in Cr_2O_3 is at the same rate as Cr diffusion in Cr_2O_3 and smaller than Fe diffusion in Fe_2O_3 [70,85]. From the latter it can be concluded that Fe_2O_3 is less protective than Cr_2O_3 in austenitic stainless steels. Therefore, at higher SCW temperature, Fe at the alloy/oxide interface can diffuse more easily through the Cr_2O_3 scale to form a very common Fe_2O_3-Cr_2O_3 solid solution [86,87]. H. Asteman et al. [88] implied that a Cr-rich $[Cr,Fe]_2O_3$ (as in Alloy 800HT and Alloy 33) can have the identical electronic and transport properties as pure Cr_2O_3, whereas an Fe-rich $[Cr,Fe]_2O_3$ can have similar properties as a less protective Fe_2O_3. During oxidation, if the critical Cr concentration in the oxide falls below the critical value for the formation of a Cr-rich $[Cr,Fe]_2O_3$ (as quite possibly the case for Alloy 800HT in long-term exposure) the oxide will eventually transform into a Fe-rich $[Cr,Fe]_2O_3$, well known as Fe_2O_3 and can also break down to form Fe-rich magnetite islands on top [88].

The formation of a more protective $[Cr,Fe]_2O_3$ layer on Alloy 33 than Alloy 800HT can also be supported by the Cr-depleted zone depth in the subsurface in both alloys. Figure 5-4 shows the average normalized concentration depth profiles for each of the alloying elements that incorporate into the $[Cr,Fe]_2O_3$ layer from three sets of measurements through the scale and substrate. Similar to the explanation provided in Section 5.1, the larger Cr-depleted zone formed in Alloy 800HT (633±62 nm) was due to the less Cr content present at the alloy/oxide interface to facilitate the formation of the $[Cr,Fe]_2O_3$ layer for which Cr needs to diffuse from deeper areas in the alloy. The Cr-depleted zone was shallower (401±43 nm) in Alloy 33 as more Cr was available to diffuse into the interface to maintain the existence of $[Cr,Fe]_2O_3$. Also, Fe and Mn concentration in the oxide scale formed on Alloy 800HT was somewhat higher than that observed in the Alloy 33 oxide layer, showing a less protective oxide scale formed on Alloy 800HT.

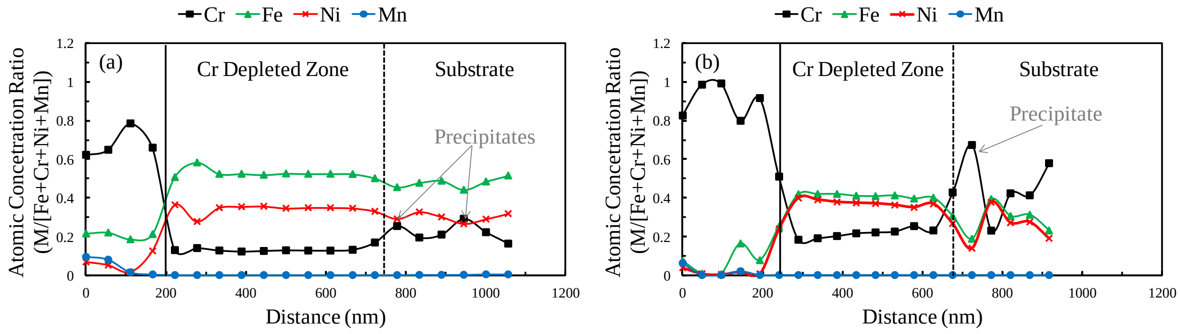

Figure 5-4 Atomic concentration ratio depth profile of Cr, Fe, Ni and Mn for (a) Alloy 800HT and (b) Alloy 33 exposed to SCW at 625 °C for 500 h.

Mn can be present in the oxide scales formed on high Cr-containing alloys (alloys with the capability to form Cr_2O_3) in both types of MnO (solid solution with Cr_2O_3) and

$MnCr_2O_4$ spinel on top of the Cr_2O_3 layer [89]. Mn concentration in both Alloy 800HT and Alloy 33 is very low (0.6 wt%). Nonetheless, in all cases in the current study, Mn formed a solid solution with the $[Cr,Fe]_2O_3$ layer, except for the case of Alloy 800HT after exposure in 625 °C SCW in which a $[Fe,Mn]Cr_2O_4$ spinel formed on top of the $[Cr,Fe]_2O_3$ layer. Not to mention, the Mn concentration in the $[Cr,Fe]_2O_3$ formed on Alloy 33 was much less (Figure 4-30). Presence of Mn along with Fe in the $[Fe,Mn]Cr_2O_4$ spinel layer can be an indication of less Fe diffusion through the $[Cr,Fe]_2O_3$ layer on Alloy 800HT therefore, assisting the corrosion resistance behaviour of the alloy.

Table 5-2 shows the oxide thickness (t) comparison between the major components of the scale formed on Alloy 800HT with that formed on Alloy 33. The t_{avg}/t_{max} ratio for the M_2O_3 formed on Alloy 800HT was slightly lower (0.82) than Alloy 33 (0.88). Also no secondary oxide phase was formed on the oxide M_2O_3 layer on Alloy 33, whereas a spinel $[Fe,Mn]Cr_2O_4$ layer was formed on top of the M_2O_3 layer on Alloy 800HT. This confirms that the M_2O_3 on Alloy 800HT was acting as a less protective layer.

Table 5-2 Oxide thickness measurement using ImageJ software [64]

		Oxide Thickness (nm)		
Alloy	**Oxide Type Formed On The Alloy**	**t_{max}**	**t_{avg}**	**t_{avg}/t_{max}**
800HT	$[Fe,Mn]Cr_2O_4$	88	62±9	0.70
	Clean Oxide Scale: $[Cr,Fe]_2O_3$	158	130±11	0.82
	Oxide Island/Crater Int.: $[Cr,Fe]_2O_3$	165	126±11	0.76
33	$[Cr,Fe]_2O_3$	232	205±14	0.88

A comparison between low magnification SEM images from the corroded surfaces of Alloy 800HT after 550 °C and 625 °C SCW test revealed that the volume concentration of oxide islands that were observed on Alloy 800HT at 625 °C was very much less than that at 550 °C, it seems as though the $[Cr,Fe]_2O_3$ layer formed on Alloy 800HT was somewhat more protective at 625 °C, which might be due to Mn diffusion through the scale. As mentioned earlier, presence of Mn in the $[Cr,Fe]_2O_3$ layer even though very small seemed to decrease the Fe concentration in the $[Cr,Fe]_2O_3$ layer. However, this effect needs to be studied in further detail.

The oxide scale formed on both alloys was a multi-layered structure. The scale on Alloy 800HT also consisted of a Ti-Si oxide layer, whereas the scale formed on Alloy 33 consisted of a Si oxide layer at the 625 °C SCW. The thickness of these layers was measured to be 62±8 and 46±7 nm respectively. Such small thicknesses however, were not believed to play a role in controlling the corrosion rate in the alloys (section 5.1) [78].

Figure 5-3 also illustrates formation of the oxide islands formed on Alloy 800HT right above the oxide crater in the alloy subsurface. Formation of such islands however, was not associated with the twin boundaries as was the case for the 550 °C test. One possible reason for this can be the faster Cr diffusion along the grain boundaries compared with bulk diffusion [70]. As a result, areas further away from the grain boundaries tend to be more susceptible to form a less protective $[Cr,Fe]_2O_3$ with smaller grains which can facilitate inward diffusion of O into the alloy as well as outward diffusion of Mn, Cr and Fe to form the oxide islands on the alloy surface [56]. Such behaviour however, needs to be investigated in more details.

Presence of precipitates formed in both alloys at 625 °C exposure in SCW are also important to discuss. J. Erneman et al. [90] reported the formation of Cr-rich precipitates along grain boundary and inside grains in Alloy 800HT after it was aged at 600 °C for 85,388 h. They characterized such precipitates to be $M_{23}C_6$. Cr-rich carbide precipitates in Alloy 33 seemed to have formed below the Cr depleted zone after enough Cr was diffused out to form the $[Cr,Fe]_2O_3$ and also in the direction of micro twins that could be formed during coupon grinding prior to exposure [91]. Existence of such precipitates in both Alloy 800HT and Alloy 33 were not been considered to be playing a controlling role in the formation of a protective $[Cr,Fe]_2O_3$ and the following corrosion resistance in both alloys. However, they will likely have important consequences affecting the mechanical integrity of these alloys. Such an examination and discussion is beyond the scope of this work.

5.3. Cr Volatization in SCW

As mentioned in section 2.4, one major concern in using high Cr-containing alloys is the Cr volatization possibility. To address this issue, a simple mass balance approximation on Alloy 33 with higher Cr content was performed. Only Alloy 33 was used for this measurement for the following reasons : (i) the oxide (M_2O_3) on Alloy 33 had a more uniform structure compared with the more complex oxide structure on Alloy 800HT and (ii) if the higher Cr-containing alloy (Alloy 33) did not show any Cr volatization, the possibility of the alloy with the less Cr content (Alloy 800HT) exposed in the same condition in Cr volatization would be less. Figure 6-1 shows the cross-section of Alloy 33 and the oxide layer on top of the Cr-depleted substrate. It should be noted that in both cases for simplicity in calculations, the oxide scale was assumed to be a uniform pure Cr_2O_3 layer. The mass balance calculation for both temperatures studied is shown below. Values used for these calculations are also shown in Table 5-3.

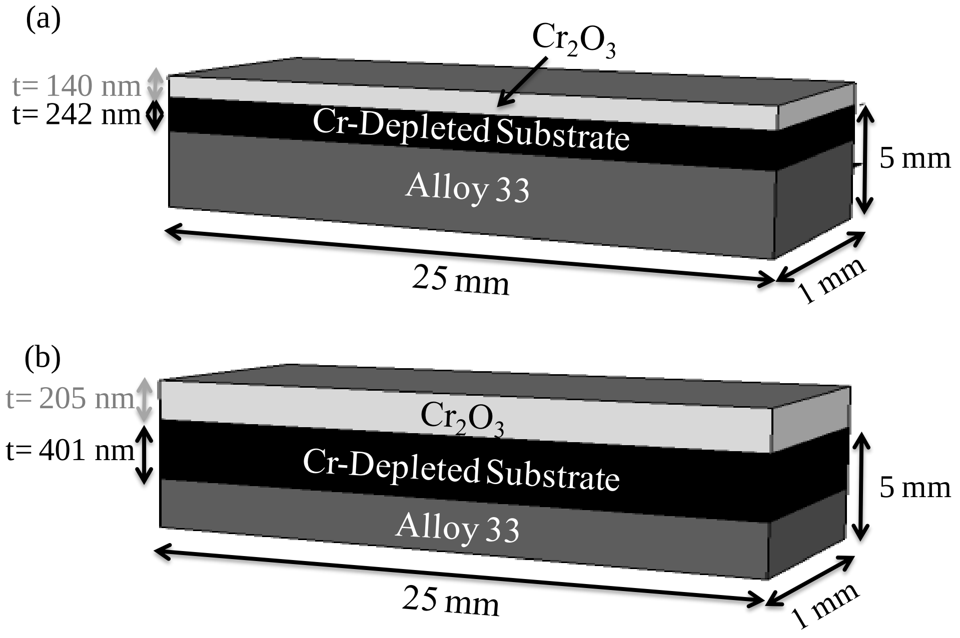

Figure 5-5 Cross-section model of Alloy 33 after exposure in 25 MPa SCW with the assumed pure Cr_2O_3 oxide scale on one surface for the exposure temperature of (a) 550 °C and (b) 625 °C.

To calculate the simplified mass balance approximation, the following approach is performed. Firstly the amount of Cr^{3+} in the Cr_2O_3 layer was measured. To do so, the Cr_2O_3 layer volume [$V_{Cr_2O_3}$(cm^3)] was measured with the previous knowledge about the coupons dimension and the thickness of the oxide layer measured from STEM analysis. These values are also shown in Figure 6-1. Using the Cr_2O_3 density [$\rho_{Cr_2O_3}$(g/cm^3)], the Cr_2O_3 mass [$m_{Cr_2O_3}$(g)] was calculated. Then a simple mass molarity calculation was performed to measure the Cr^{3+} concentration [$C_{Cr^{3+}\text{in } Cr_2O_3 \text{ Layer}}$(mg)]. Secondly, the amount of Cr^{3+} in the Cr-depleted zone was measured. For this purpose, Cr-depleted zone volume [$V_{\text{Cr-Depleted Zone}}$(cm^3)] was calculated using the coupons dimension and the Cr-depleted depth measured via STEM (Figure 6-1). Then knowing the density of Alloy 33 [$\rho_{\text{Alloy 33}}$ (g/cm^3)], sum of the three major alloying elements (Fe, Ni and Cr) masses [$m_{(Fe+Ni+Cr)}$ (g)] was measured. As the chemical composition of Alloy 33 includes 33.4 wt.% Cr, Cr concentration in the Cr-depleted zone [$C_{\text{Cr in Cr}-\text{Depleted Zone}}$(mg)]$_1$ was measured. However, as the amount of Cr in the depleted zone after exposure did not go to zero, there still existed some Cr which could be detected using STEM/EDS analysis. This value was subtracted from the initially measured Cr concentration in the depleted zone [$C_{(\text{Cr in Cr}-\text{Depleted Zone})}$]$_2$. It is worth mentioning that if:

$$C_{(Cr^{3+}\text{in } Cr_2O_3 \text{ Layer})} \geq [\, C_{(\text{Cr in Cr}-\text{Depleted Zone})}]_2$$

then Cr_2O_3 volatization is less likely to occur as nearly all the Cr present in the alloy was consumed to form the oxide layer and no Cr^{3+} was dissolved from the oxide layer.

Table 5-3 Parameter values used for the first approximate mass balance performed on Alloy 33 after 500 h exposure in 25 MPa SCW

SCW Temp. (°C)	**Coupon Dimension (mm)**	**$\rho_{\text{Alloy 33}}$ (g/cm^3)**	**Actual Oxide Layer**	**Assumed Oxide Layer**	**$\rho_{Cr_2O_3}$ (g/cm^3)**	**t_{oxide} (nm)**	**$t_{\text{Cr-Depleted Substrate}}$ (nm)**
550	25 × 5 × 1	7.90	Cr_2O_3	Cr_2O_3	`5.22	140	242
625			$[Cr,Fe]_2O_3$			205	401

5.3.1. Alloy 33 Exposed in 25 MPa and 550 °C SCW

- **Calculations for Cr^{3+} Concentration in the Cr_2O_3 Layer:**

Firstly, $m_{Cr_2O_3}$ was measured from eq. 8 and by calculating the $V_{Cr_2O_3}$ value.

$$\rho = \frac{m}{V} \tag{8}$$

$$V_{Cr_2O_3} = 25 \times 10^{-3} \times 5 \times 10^{-3} \times 140 \times 10^{-9} = 1.75 \times 10^{-11} \mathrm{m}^3 = \mathbf{1.75 \times 10^{-5}}\ \mathrm{cm}^3$$

Knowing that $\rho_{Cr_2O_3}$ is $5.22 \frac{\mathrm{g}}{\mathrm{cm}^3}$ $\therefore$ $m_{Cr_2O_3} = \mathbf{9.14 \times 10^{-5}}\mathrm{g}$

Then, a simple mass molarity calculation was performed as following to measure the Cr^{3+} concentration in the Cr_2O_3 layer:

$$C_{Cr^{3+} \mathrm{in}\ Cr_2O_3\ \mathrm{Layer}} = 9.14 \times 10^{-5}\mathrm{g}\ Cr_2O_3 \times \frac{1\ \mathrm{mole}\ Cr2O3}{152\ \mathrm{g}\ Cr2O3} \times \frac{2\mathrm{mole}\ Cr}{1\mathrm{mole}\ Cr2O3} \times \frac{52\ \mathrm{g}\ Cr}{1\ \mathrm{mole}\ Cr} =$$
$$6.25 \times 10^{-5}\mathrm{g} = \mathbf{0.06}\ \mathrm{mg}\ Cr^{3+}\ \mathrm{in}\ Cr_2O_3$$

- **Calculations for Cr^{3+} Concentration in the Cr-Depleted Substrate:**

Same approach was used to measure the $m_{(Fe+Ni+Cr)}$ in the Cr-depleted zone from eq. 8 and by calculating the $V_{\text{Cr-Depleted Zone}}$ value:

$$V_{\text{Cr-Depleted Zone}} = 25 \times 10^{-3} \times 5 \times 10^{-3} \times 242 \times 10^{-9} = 3.03 \times 10^{-11} m^3$$
$$= \mathbf{3.03 \times 10^{-5}}\ cm^3$$

Knowing that $\rho_{\text{Alloy 33}}$ is $7.9 \frac{\mathrm{g}}{\mathrm{cm}^3}$ $\therefore$ $m_{(Fe+Ni+Cr)} = 2.39 \times 10^{-4} g = \mathbf{0.24}\ mg$

According to ICP test, Cr concentration in Alloy 33 is 33.4 wt.%. Therefore, the Cr^{3+} concentration in the 0.24 mg of Alloy 33 is 0.08 mg.

However, as explained, according to STEM/EDS analysis the Cr content does not drop to zero. It drops to 9-13 wt.% which is ~ 0.02 mg Cr that is still present in the Cr-depleted zone. Therefore 0.08-0.02 = 0.06 mg is the amount of Cr that has left the alloy. In other words:

Cr^{3+} that is present in Cr_2O_3 layer: 0.06 mg

Cr^{3+} that has left the Cr depleted zone: 0.06 mg

As can be seen, the amount of Cr^{3+} that has left the alloy substrate matches well to the amount of Cr^{3+} that is present in the oxide scale. This suggests the presence of an Fe-free Cr_2O_3 oxide scale formed on Alloy 33 at 550 °C. It also shows that the Cr volatization from the scale in the 550 °C in the essentially deaerated SCW is unlikely, albeit after a very short exposure time (circa 500 h).

5.3.2. Alloy 33 Exposed in 25 MPa and 625 °C SCW

- **Calculations for Cr^{3+} Concentration in Cr_2O_3 Layer:**

Using eq. 8, the $m_{Cr_2O_3}$ was measured after calculating the $V_{Cr_2O_3}$.

$$V_{Cr_2O_3} = 25 \times 10^{-3} \times 5 \times 10^{-3} \times 205 \times 10^{-9} = 2.56 \times 10^{-11} m^3 = \mathbf{2.56 \times 10^{-5}} \, cm^3$$

Knowing that the $\rho_{Cr_2O_3}$ is $5.22 \frac{g}{cm^3}$ $\therefore$ $m_{Cr_2O_3} = \mathbf{1.34 \times 10^{-4}} g$

Then, by performing a mass molarity measurement as below, Cr^{3+} concentration value in the Cr_2O_3 layer was obtained:

$$C_{Cr^{3+} \text{in } Cr_2O_3 \text{ Layer}} = 1.34 \times 10^{-4} g \, Cr_2O_3 \times \frac{1 \text{ mole Cr2O3}}{152 \text{ g Cr2O3}} \times \frac{2 \text{mole Cr}}{1 \text{mole Cr2O3}} \times \frac{52 \text{ g Cr}}{1 \text{ mole Cr}} =$$

$9.15 \times 10^{-5} = \mathbf{0.09}$ mg Cr^{3+} in Cr_2O_3

- **Calculations for Cr^{3+} in the Cr-Depleted Substrate:**

Same approach was used to measure the $m_{(Fe+Ni+Cr)}$ in the Cr-depleted zone from eq. 8 and by calculating the $V_{\text{Cr-Depleted Zone}}$ value:

$$V_{\text{Cr-Depleted Zone}} = 25 \times 10^{-3} \times 5 \times 10^{-3} \times 401 \times 10^{-9} = 5.01 \times 10^{-11} m^3$$
$$= \mathbf{5.01 \times 10^{-5}} \, cm^3$$

Knowing that $\rho_{\text{Alloy 33}}$ is $7.9\,\frac{g}{cm^3}$ $\therefore$ $m_{(Fe+Ni+Cr)}= 3.95 \times 10^{-4} g = \mathbf{0.40}\ mg$

According to ICP test, Cr concentration in Alloy 33 is 33.4 wt.%. Therefore, the Cr^{3+} concentration in the 0.40 mg of Alloy 33 is 0.13 mg.

However, according to STEM/EDS analysis, the Cr content in the Cr-depleted substrate after exposure does not go to zero. It goes to around 16 < wt.% which is ∼ 0.06 mg Cr that is still present in the Cr depleted zone:

Cr^{3+} that is present in Cr_2O_3 layer: 0.09 mg

Cr^{3+} that has left the Cr-depleted zone: 0.07 mg

As shown above, the amount of Cr^{3+} present in the oxide layer is almost equal to the amount of Cr^{3+} that has left the underneath substrate. This can represent the very low possibility of Cr volatization from the layer formed on Alloy 33 exposed in 625 °C and 25 MPa SCW for a short-term run in the degassed static autoclave. It should be noted that the slightly higher amount of Cr^{3+} in the Cr_2O_3 layer that is calculated can be due to the assumption that the oxide is purely Cr_2O_3 without any Fe and/or Mn whereas it was shown earlier in the results section that the scale formed on Alloy 33 at 625 °C has slightly amount of Fe and Mn ions dissolved in it.

6. Conclusions

- Gravimetric measurements and electron microscopy techniques were used to relate the short-term (500 h) corrosion resistance of austenitic Fe-Cr-Ni alloys in 25 MPa SCW at 550 ºC and 625 ºC to the structure and composition of the oxide scale formed.

- Corrosion resistance increased in the expected manner with an increase in the bulk Cr content (Type 316L << Alloy 800HT < Alloy 33).

- The higher bulk Cr content in both Alloy 800HT and Alloy 33 after exposure in 25 MPa and 550 ºC SCW resulted in the following conclusions: (i) the formation of a corundum-type M_2O_3 (where M = Cr and Fe) external layer that did not form on Type 316L stainless steel. The composition of the corundum-type M_2O_3 external base layer depended on the alloy: the layer formed on Alloy 33 contained a significantly lower Fe content than that formed on Alloy 800HT, (ii) the formation of an outer spinel-type M_3O_4 (where M = Fe, Cr and Ni) external layer, which had formed on Alloy 800HT, was prevented in Alloy 33 and (iii) an apparent twin boundary-induced enhanced internal oxidation zone in Alloy 800HT that formed a multi-layered scale was prevented in Alloy 33.

- Oxide scales structure formed on Alloy 800HT and Alloy 33 after exposure in 25 MPa and 625 ºC SCW was similar to that observed at 550 °C test except higher Mn concentration was detected in the scales formed on both alloys. However, the outer spinel-type M_3O_4 (M= Fe, Cr, Mn and/or Ni) islands that were formed on Alloy 800HT were not tied up to twin boundaries as they were at 550 °C test. The reason for this is still unknown and deserves further attention.

- Cr-rich carbide precipitates were observed in both alloys in the 625 °C test whereas almost none was observed in the 550 °C test after 500 h. Formation of such precipitates did not seem to have any effect on the alloys corrosion resistance nonetheless, their effect on the in-service mechanical integrity needs to be investigated in more details.

- First approximation mass balance showed no Cr_2O_3 volatization after short-term (500 h) corrosion test in the deaerated SCW.

7. References

[1] T. Abram and S. Ion, "Generation IV nuclear power: A review of the state of the science", *Energy Policy*, Vol. 36, 2008, pp. 4323-4330.

[2] S. Penttila, A. Toivonen, L. Rissanen and L. Heikinheimo, "Generation IV materials issue - case SCWR", *Journal of Disaster Research*, Vol.5, No.4, 2010, pp. 1-10.

[3] K. Fischer, T. Schulenberg and E. Laurien, "Design of a supercritical water-cooled reactor with a three-pass core arrangement", *Nuclear Engineering and Design*, Vol. 239, 2009, pp. 800-812.

[4] T. Schulenberg, H. Matsui, L. Leung and A. Sedov, "Supercritical water cooled reactors", *GIF symposium proceedings/2012 annual report*, pp. 63-76.

[5] K. Yamada, "Overview of IAEA activities on SCWRs", *Joint McMaster-IAEA course on science and technology of SCWRs*, Hamilton, Canada, 2012.

[6] I. Pioro, "Introduction and historical development of supercritical water-cooled reactors (SCWRs)", *Joint McMaster-IAEA course on science and technology of SCWRs*, Hamilton, Canada, 2012.

[7] S. Mokry, I. Pioro, A. Farah, K. King, S. Gupta, W. Peiman and P. Kirillov, "Development of supercritical water heat-transfer correlation for vertical bare tubes", *Nuclear Engineering and Design*, Vol. 241, 2011, pp. 1126–1136.

[8] D.F. Wang and S. Wang, "A preliminary cathena thermalhydraulic model of the Canadian SCWR for safety analysis", *AECL Nuclear Review*, Vol. 3, No. 1, 2014, pp. 9-16.

[9] L.K.H. Leung, "Update on the Canadian SCWR concept", The 3rd Canadian SCWR Information Exchange Workshop for the Phase II NSERC/NRCan/AECL Gen-IV Energy Technologies Program,Vancouver, Canada, August 22, 2014.

[10] X. Cheng, "Introduction to Thermal-Hydraulics", Proceeding 5th International Symposium on Supercritical Water-cooled Reactors, Vancouver, Canada, March 13-17, 2011.

[11] C. Li, J. Shan and L.K.H. Leung, "Subchannel analysis of CANDU-SCWR fuel", *Progress in Nuclear Energy*, Vol. 51, 2009, pp. 799–804.

[12] J. Shan, B. Zhang, C. Li, and L.K.H. Leung, "SCWR subchannel code ATHAS development and CANDU-SCWR analysis", *Nuclear Engineering and Design*, Vol. 239, 2009, pp. 1979–1987.

[13] J. Yu, H. Liu, B. Jia, "Sub-channel analysis of CANDU–SCWR and review of heat-transfer correlations", *Progress in Nuclear Energy*, Vol. 51, 2009, pp. 246–252.

[14] D. Bröll, C. Kaul, A. Krämer, P. Krammer, T. Richter, M. Jung, H. Vogel and P. Zehner, "Chemistry in Supercritical Water", *Angewandte Chemie International Edition*, Vol. 38, 1999, pp. 2998-3014.

[15] D.A. Guzonas and W.G. Cook, "Cycle chemistry and its effect on materials in a supercritical water-cooled reactor: A synthesis of current understanding", *Corrosion Science*, Vol. 65, 2012, pp. 48-66.

[16] H. Weingärtner and E.U. Franck, "Supercritical Water as a Solvent", *Angewandte Chemie International Edition*, Vol. 44, 2005, pp. 2672 – 2692.

[17] A.T. Motta, A. Yilmazbayhan, M.J. Gomes da Silva, R.J. Comstock, G.S. Was, J.T. Busby, E. Gartner, Q. Peng, Y.H. Jeong, and J.Y. Park, "Zirconium Alloys for Supercritical Water Reactor Applications: Challenges and Possibilities", *Journal of Nuclear Materials,* Vol. 371, 2007, pp. 61-75.

[18] R.P. Olive, "Pourbaix diagrams, solubility predictions and corrosion-product deposition modelling for the supercritical water-cooled reactor", PhD Thesis, University of New Brunswick, Department of Chemical Engineering, 2012.

[19] G.S. Was, S. Teysseyre and Z. Jiao, "Corrosion of austenitic alloys in supercritical water", *Corrosion*, Vol. 62, 2006, No. 11, pp. 989-1005.

[20] N. Zhang, Y. Bai, X. Yuan, B. Li and H. Xu, "Corrosion behavior of austenitic and ferritic/martensitic steels exposed in supercritical water with dissolved oxygen", *Applied Mechanics and Materials,* Vols. 71-78, 2011, pp 2916-2919.

[21] X. Luo, R. Tang, C. Long, Z. Miao, Q. Peng and C. Li, "Corrosion behaviour of austenitic and ferritic steels in supercritical water", *Nuclear Engineering and Technology,* Vol. 40, No. 2, 2008, pp. 147-154.

[22] A.D. Siwy, T.E. Clark and A.T. Motta, "Transmission electron microscopy of oxide development on 9Cr ODS steel in supercritical water", *Journal of Nuclear Materials,* Vol. 392, 2009, pp. 280-285.

[23] N. Otsuka and H. Fujikawa, "Scaling of austenitic stainless steels and nickel-base alloys in high-temperature steam at 973 K", *Corrosion*, Vol. 47, No. 4, 1991, pp. 240-248.

[24] F.H. Stott and F.I. Wei, "High temperature oxidation of commercial austenitic stainless steels", *Materials Science and Technology*, Vol. 5, 1989, pp. 1140-1147.

[25] J. Botella, C. Merino and E. Otero, "A Comparison of the high-temperature oxidation of 17Cr-2Ni and 18Cr-8Ni austenitic stainless steels at 973K", *Oxidation of Metals*, Vol. 49, Nos. 3/4, 1998, pp. 297-324.

[26] Y. Chen, K. Sridharan, and T.R. Allen, "Corrosion of candidate austenitic stainless steels for supercritical water reactors", NACE international 2007.

[27] P. Yvon and F. Carré, "Structural materials challenges for advanced reactor systems", *Journal of Nuclear Materials*, Vol. 385, 2009, pp. 217–222.

[28] X. Ren, K. Sridharan and T.R. Allen, "Corrosion of ferritic–martensitic steel HT9 in supercritical water", *Journal of Nuclear Materials*, Vol. 358, 2006, pp. 227-234.

[29] D.A. Guzonas. The 5th Int. Sym. SCWR (ISSCWR-5), Vancouver, British Columbia, Canada, March 13-16, 2011.

[30] L. Zhang, Y. Bao and R. Tang, "Selection and corrosion evaluation tests of candidate SCWR fuel cladding materials", *Nuclear Engineering and Design*, Vol. 249, 2012, pp.180– 187.

[31] G.S. Was, P. Ampornrat, G. Gupta, S. Teysseyre, E.A. West, T.R. Allen, K. Sridharan, L. Tan, Y. Chen, X. Ren and C. Pister, "Corrosion and stress corrosion cracking in supercritical water", *Journal of Nuclear Materials*, Vol. 371, 2007, pp. 176–201.

[32] D. Guzonas and R. Novotny, "Supercritical water-cooled reactor materials - Summary of research and open issues", *Progress in Nuclear Energy*, xxx, 2014, pp. 1-12.

[33] Y. Jiao, S. Mahboubi, J. Kish, W. Cook, W. Zheng and D. Guzonas, "Influence of thermal aging on the corrosion resistance of austenitic Fe-Cr-Ni alloys in SCW", The 6th International Symposium on Supercritical Water-Cooled Reactors, ISSCWR-6, 2013.

[34] L. Tan, T.R. Allen and Y. Yang, "Corrosion behavior of alloy 800H (Fe-21Cr-32Ni) in supercritical water", *Corrosion Science*, Vol. 53, 2011, pp. 703-711.

[35] J. Li, W. Zheng, S. Penttilä, P. Liu, O.T. Woo and D. Guzonas, "Microstructure stability of candidate stainless steels for Gen-IV SCWR fuel cladding application", *Journal of Nuclear Materials*, Vol. 454, 2014, pp. 7–11.

[36] A.T. Motta, A. Yilmazbayhan, M.J. Gomes da Silva, R.J. Comstock, G.S. Was, J.T. Busby, E. Gartner, Q. Peng, Y.H. Jeong, and J.Y. Park, “Zirconium alloys for supercritical water reactor applications: challenges and possibilities”, *Journal of Nuclear Materials*, Vol. 371, 2007, pp. 61-75.

[37] C. Wagner, B. Bunsenges, *Physics and Chemistry*, Vol. 63, 1959, pp.772.

[38] N. Birks, G. H. Meier and F. S. Pettit, "Introduction to the high-temperature oxidation of metals", 2nd edition, Cambridge University Press, 2006 - Technology and Engineering.

[39] C.T. Sims, N.S. Stoloff and W.C. Hagel, "Superalloys II; High temperature materials for aerospace and industrial power", New York, John Wiley and Sons, 1987.

[40] A. S. Khanna, "Introduction to High Temperature Oxidation and Corrosion", ASM International, 2002- Technology and Engineering.

[41] J.K. Tien and T. Caulfield, "Superalloys, supercomposites and superceramics", Academic Press Incorporation, 1989- Materials Science and Technology Series.

[42] G. Wright and R.B. Dooley, "A review of the oxidation behaviour of structural alloys in steam", *International Materials Reviews*, Vol. 55, No. 3, 2010, pp. 129-167.

[43] W. Kuang, X. Wu and E. Han, "The oxidation behaviour of 304 stainless steel in oxygenated high temperature water", *Corrosion Science*, Vol. 52, 2010, pp. 4081-4087.

[44] A.C.S. Sabioni, A.M. Huntz, F. Silva and F. Jomard, "Diffusion of iron in Cr_2O_3: polycrystals and thin films", *Materials Science and Engineering*, Vol. A 392, 2005, pp. 254-261.

[45] D.R. Gaskell, "Introduction to the Thermodynamics of Materials", 5th edition, By Taylor and Francis, 2008.

[46] Available from: http://www.factsage.com/.

[47] Y. Nishiyama, Y. Hayaso and N. Otsuka, "Corrosion resistant boiler tube materials for advanced coal fired steam generating systems", 28th International Conference on ‘Coal utilization’, Clearwater,FL, USA, March 2003, Coal Technology Association.

[48] D.S. Li, D. Li, H. Dou, P. Gao, Y. Liu, X.J. Chen, X.C. Jiang and J.J. Pei, "High-temperature oxidation resistance of austenitic stainless steels", *Key Engineering Materials*, Vols. 575-576 , 2014, pp. 414-417.

[49] T. Cheng, J.R. Keiser, M.P. Brady, K.A. Terrani and B.A. Pint, "Oxidation of fuel cladding candidate materials in steam environments at high temperature and pressure", *Journal of Nuclear Materials*, Vol. 427, 2012, pp. 396-400.

[50] B.A. Pint, R. Peraldi and P.J. Maziasz, "The use of model alloys to develop corrosion-resistant stainless steels", *Materials Science Forum*, Vols. 461-464, 2004, pp. 815-822.

[51] V.V. Khokhlov, A.G. Rakoch, E.S. Dement'eva, and O.A. Lyzlov, "Theoretical analysis of anomalies in high-temperature oxidation of Fe–Cr, Fe–Ni, and Fe–Ni–Cr alloys", *Protection of Metals*, Vol. 40, No. 1, 2004, pp. 62-66.

[52] N. Otsuka, Y. Shida and H. Fujikawa, " Internal-external transition for the oxidation of Fe-Cr-Ni austenitic stainless steels in steam", *Oxidation of Metals*, Vol. 32, Nos. 1/2, 1989, pp. 13-45.

[53] D.J. Young and B.A. Pint, "Chromium volatilization rates from Cr_2O_3 scales into flowing gases containing water vapor", *Oxidation of Metals,* Vol. 66, Nos. 3/4, 2006, pp. 137-153.

[54] D.J. Young, "Effect of water vapour on the oxidation of chromia formers", *Materials Science Forum*, Vols. 595-598, 2008, pp. 1189-1197.

[55] A. Yamauchi, K. Kurokawa and H. Takahashi, "Evaporation of Cr_2O_3 in Atmospheres containing H_2O", *Oxidation of Metals*, Vol. 59, Nos. 5/6, 2003, pp. 517-527.

[56] M. Halvarsson, J.E. Tang, H. Asteman, J.-E. Svensson and L.-G. Johansson, "Microstructural investigation of the breakdown of the protective oxide scale on a 304 steel in the presence of oxygen and water vapour at 600 °C", *Corrosion Science*, Vol. 48, 2006, pp. 2014-2035.

[57] H. Asteman, J.-E. Svensson and L.-G. Johansson, "Oxidation of 310 steel in H_2O/O_2 mixtures at 600 °C: the effect of water-vapour-enhanced chromium evaporation", *Corrosion Science*, Vol. 44, 2002, pp. 2635-2649.

[58] J. Bischoff and A.T. Motta, "EFTEM and EELS analysis of the oxide layer formed on HCM12A exposed to SCW", *Journal of Nuclear Materials*, Vol. 430, 2012, pp. 171-180.

[59] C. Colliex, T. Manoubi and C. Ortiz, "Electron-energy-loss-spectroscopy near-edge fine structures in the iron-oxygen system", *Physics Revolution B (Condense. Matter),* Vol. 44, 1991, pp. 11402-11411.

[60] D.A. Eustace, D.W. McComb and A.J. Craven, "Probing magnetic order in EELS of chromite spinels using both multiple scattering (FEFF8.2) and DFT (WIEN2k)", *Micron*, Vol. 41, 2010, pp. 547-553.

[61] H. Kurata and C. Colliex, "Electron energy loss core edge structures in manganese oxides", *Physical Review B,* Vol. 48, 1993, pp. 2102-2108.

[62] G.A. Botton, C.C. Appel, A. Horsewell and W.M. Stobbs, "Quantification of the EELS near-edge structures to study Mn doping in oxides", *Journal of Microscopy,* Vol. 180, 1995, pp. 211-216.

[63] Available from: http://plotdigitizer.sourceforge.net/.

[64] Available from: http://imagej.nih.gov/ij/.

[65] Available from: http://www.fiz-karlsruhe.com/icsd_home.html.

[66] Available from: http://cimewww.epfl.ch/people/stadelmann/jemswebsite/jems.html.

[67] Available from: http://www.gatan.com/scripting/downloads.php.

[68] S. Mahboubi, G.A. Botton and J.R. Kish, "Effect of Cr content on corrosion resistance of Fe-Cr-Ni alloys exposed in supercritical water (SCW)", *submitted to Corrosion Science*, Proceeding, August 2014.

[69] O.Yu. Goncharov, "Thermodynamic assessment of high temperature oxidation of Fe–Cr alloys in air", *Inorganic Materials,* Vol. 40, 2004, pp. 1295–1300.

[70] R.E. Lobnig, H.P. Schmidt, K. Hennesen and H.J. Grabke, "Diffusion of cations in chromia layers grown on iron-base alloys", *Oxidation of Metals,* Vol. 37, 1992, pp. 81-93.

[71] K. Sugimota, M. Seto, S. Tanaka, and N. Hara, "Corrosion resistance of artificial passivation films of Fe_2O_3-Cr_2O_3-NiO formed by metalorganic chemical vapor deposition", *Journal of Electrochemical Society,* Vol. 140, 1993, pp. 1586-1592.

[72] P. Schmuki, S. Virtanen, H.S. Isaacs, M.P. Ryan, A.J. Davenport, H. BÖhni and T. Stenberge, "Electrochemical behavior of Cr_2O_3/Fe_2O_3 artificial passive films studied by in situ XANES", *Journal of Electrochemical Society,* Vol. 145, 1998, pp. 791-801.

[73] G.M. Ecer, R.B. Singh and G.H. Meier, "The influence of superficially applied oxide powders on the high-temperature oxidation behavior of Cr_2O_3-forming alloys", *Oxidation of Metals,* Vol. 18, 1982, pp. 55-81.

[74] S.C. Tsai, A.M. Huntz and C. Dolin, "Growth mechanism of Cr_2O_3 scales: oxygen and chromium diffusion, oxidation kinetics and effect of yttrium", *Materials Science and Engineering,* Vol. A212, 1996, pp. 6-13.

[75] M.M.P. Soustelle and R.L. Lalauze, "Kinetics of the oxidation of metals-influence of self-diffusion of metal", Oxidation of Metals, Vol. 7, 1973, pp. 23-29.

[76] H.E. Evans, D.A. Hilton and R.A. Holm, "Chromium-depleted zones and the oxidation process in stainless steels", *Oxidation of Metals*, Vol. 10, 1976, pp. 149-161.

[77] R.N. Durham, B. Gleeson and D.J. Young, "Factors affecting chromium carbide precipitate dissolution during alloy oxidation", *Oxidation of Metals*, Vol. 50, 1998, pp. 139-165.

[78] H.E. Evans, D.A. Hilton, R.A. Holm, and S.J. Webster, "Influence of Silicon Additions on the Oxidation Resistance of a Stainless Steel", *Oxidation of Metals*, Vol. 19, 1983, pp. 1-18.

[79] A.S. Nagelberg, "Oxidation of titanium modified Type 310 stainless steel in low oxygen partial pressure atmospheres", *Oxidation of Metals*, Vol. 17, 1982, pp. 415-427.

[80] J.H. Chen, P.M. Rogers and J.A. Little, "Isothermal and cyclic oxidation of chromia forming nickel-based superalloys", *Materials Science Forum*, Vol. 251-254, 1997, pp. 57-64.

[81] T.D. Nguyen, J. Zhang and D.J. Young, "Effects of cerium and manganese on corrosion of Fe-Cr and Fe-Cr-Ni alloys in Ar-20CO_2 gas at 818 °C", *Corrosion Science*, Vol. 76, 2013, pp. 231-242.

[82] T.N. Rhys-Jones, H.J. Grabke and H. Kudielka, "The effects of various amounts of alloyed cerium and cerium oxide on the high temperature oxidation of Fe-10Cr and Fe-20Cr alloys", *Corrosion Science*, Vol. 27, 1987, pp. 49-73.

[83] I. Wolf, H.J. Grabke and P. Schmidt, "Carbon transport through oxide scales on Fe-Cr alloys", *Oxidation of Metals*, Vol. 29, 1988, pp. 289-306.

[84] T.N. Rhys-Jones and H.J. Grabke, "Use of cerium and cerium oxide additions to improve high temperature oxidation behaviour of Fe-Cr alloys", *Materials Science and Technology*, Vol. 4, 1988, pp. 464-454.

[85] C. Gleitzer, "Electrical properties of anhydrous iron oxides", *Key Engineering Materials*, Vol. 125-126, 1997, pp. 355-418.

[86] R. K. Di Cerbo and A. U. Seybolt, "Lattice parameters of the α-Fe_2O_3-Cr_2O_3 solid solution", *Journal of the American Ceramic Society*, Vol. 42, 1959, pp. 430-431.

[87] A. Escardino, S. Mestre, A. Barba, V. Beltra´n and A. Blasco, "Synthesis mechanism of an iron–chromium ceramic pigment", *Journal of the American Ceramic Society*, Vol. 83, No. 1, 2000, pp. 29.32.

[88] H. Asteman, J.-E. Svensson, M. Norell and L.-G. Johansson, "Influence of water vapor and flow rate on the high-temperature oxidation of 304L; effect of chromium oxide hydroxide evaporation", *Oxidation of Metals,* Vol. 54, Nos. 1/2, 2000, pp. 11-26.

[89] R.K. Wild, "High temperature oxidation of austenitic stainless steel in low oxygen pressure", *Corrosion Science*, Vol. 17, 1977, pp. 87-104.

[90] J. Erneman, J.-O. Nilsson, H.-O. Andren and D. Tobjork, "Microstructural evolution during creep of Alloy 800HT in the temperature range 600 °C to 1000 °C", *Metallurgical and Materials Transactions*, Vol. 40A, 2009, pp. 539-550.

[91] W.B. Jones and R.M. Allen, "Mechanical Behavior of Alloy 800 at 838 K", *Metallurgical Transactions*, Vol. 13A, 1982, pp. 637-648.